

Contents

I Thesis overview	1
II Theory introduction	3
1 Theoretical introduction	5
1.1 Standard model	5
1.2 Theory of pp collisions	5
1.3 Proton structure	5
2 Physics of W and Z bosons in pp collisions	7
3 Methodology of the measurement	9
3.1 Cross-Section methodology	9
3.1.1 Fiducial phase-space definition	10
3.1.2 Extrapolation to the 13 TeV fiducial phase-space	10
3.2 Ratios calculation	11
3.3 Results combination	11
3.4 PDF fits	11
III Experimental setup	13
4 The Large Hadron Collider	15
5 The ATLAS experiment	17
5.1 Inner detector	17
5.2 Calorimeters	17
5.2.1 Forward calorimeters	17
5.3 Muon system	17
5.4 The magnet system	17
5.5 Trigger system	17
5.6 Atlas software	17
6 Event reconstruction	19
6.1 Tracks and vertexes	19
6.2 Electron reconstruction and identification	19
6.3 Muon reconstruction and identification	19
6.4 Missing transverse energy reconstruction	19
6.4.1 Standard Missing Transverse Energy reconstruction	19
6.4.2 Reconstruction of Missing Transverse Energy from hadronic recoil	20

7 Monte Carlo simulation	23
7.1 ATLAS chain of MC production	23
7.2 Event generators	24
7.3 Simulation in Geant4	25
8 Frozen Showers	27
8.1 Problem description	29
8.2 Generation and use in simulation	32
8.2.1 Libraries tuning	33
8.3 Machine learning based bin finding procedure	34
8.3.1 Machine learning introduction	34
8.3.2 Model description	36
8.4 Validation of the new libraries	40
9 Data and Monte-Carlo samples	43
9.1 Data sample	43
9.2 Monte-Carlo samples	43
IV The Measurement	45
10 Selection	47
10.1 Data quality cuts	47
10.2 Lepton quality cuts	48
10.3 Boson selection	49
10.4 Cut flow	49
11 Monte Carlo corrections	51
11.1 Lepton efficiency corrections	51
11.1.1 Muon Trigger SF	53
11.2 Electron energy scale and resolution	55
11.3 Muon momentum correction	56
12 Hadronic recoil calibration	59
12.1 Introduction	59
12.2 Hadronic recoil resolution correction	61
12.2.1 Event activity correction	62
12.2.2 Resolution corrections using Z events	67
12.3 Hadronic recoil bias correction	69
12.3.1 Bias determination from M_T^W distribution	69
12.3.2 Bias determination using u_{\parallel} distribution	70
12.3.3 Systematic uncertainty estimation	72
12.4 Summary on hadronic recoil systematics	73
13 Background estimation	75
13.1 QCD background estimation	76
13.1.1 Template selection	77
13.1.2 Methodology of the template sample normalization	77

13.1.3 Systematic Uncertainty from the Multi-jet Background Estimation	79
13.2 Background-subtracted W and Z candidate events	81
14 Control distributions	83
15 Uncertainties in the cross-section measurement	93
15.1 Methods of uncertainties propagation	93
15.2 Experimental systematic uncertainties	94
15.2.1 Electron energy scale and resolution	94
15.2.2 Muon energy scale and resolution	94
15.2.3 Muon and electron efficiency toy Monte-Carlo	94
15.3 Theoretical uncertainty	96
15.4 Correlation between uncertainties	96
15.4.1 Toy MC correlations	96
15.4.2 Correlations between PDF's eigenvectors	96
V Results	97
16 Results of the Cross Section Measurement	99
16.1 Combined results	100
16.2 Cross-sections ratios	101
16.3 Comparation with Theoretical Predictions	101
16.4 PDF fits	101

1

Part I

2

Thesis overview

3

Part II

4

Theory introduction

3

⁵ Chapter **1**

⁶ **Theoretical introduction**

⁷ **1.1 Standard model**

⁸ **1.2 Theory of pp collisions**

⁹ **1.3 Proton structure**

10 Chapter **2**

11 **Physics of W and Z bosons in pp collisions**

12 Chapter **3**

13 **Methodology of the measurement**

14	15	3.1 Cross-Section methodology	9
16	3.1.1 Fiducial phase-space definition	10	
17	3.1.2 Extrapolation to the 13 TeV fiducial phase-space	10	
18	3.2 Ratios calculation	11	
19	3.3 Results combination	11	
20	3.4 PDF fits	11	
21			
22			
23			
24			

25 **3.1 Cross-Section methodology**

The production cross-section of W and Z bosons in a fiducial region, corresponding to the geometrical acceptance of the detector and of the kinematic selection, measured using the equation:

$$\sigma_{W/Z}^{fid} = \frac{N - B}{C_{W/Z} L_{int}}, \quad (3.1)$$

26 where

- 27 • N is the number of candidates measured in a data
28 • B is the number of background events
29 • L_{int} is the integrated luminosity corresponding to a run selections and trigger requirements
30 • $C_{W/Z}$ is a correction factor for an experimental selection and resolution effects.

The correction factors $C_{W/Z}$ is calculated from MC for each process and each decay channel separately and defined as :

$$C_{W/Z} = \frac{N_{MC,rec}}{N_{MC,gen,cut}}, \quad (3.2)$$

31 where $N_{MC,rec}$ are sums of weights of events after simulation, reconstruction and selection, $N_{MC,gen,cut}$
32 - are taken on the generator level after fiducial cuts. These correction factor are including efficiencies
33 for trigger, reconstruction and identification (see Sec.11.1).

In addition, this measurement could be extrapolated to the full phase-space using as:

$$\sigma_{W/Z}^{tot} = \frac{\sigma_{W/Z}^{fid}}{A_{W/Z}} = \frac{N - B}{A_{W/Z} C_{W/Z} L_{int}}, \quad (3.3)$$

where $\sigma_{W/Z}^{tot}$ are the total inclusive production cross-section of the W and Z bosons, and $A_{W/Z}$ is an acceptance.

The $A_{W/Z}$ factor determined from Monte Carlo simulation as:

$$A_{W/Z} = \frac{N_{MC,gen,cut}}{N_{MC,gen,all}}, \quad (3.4)$$

where $N_{MC,gen,all}$ are the sum of weights of all generated MC events. Both $A_{W/Z}$ and $C_{W/Z}$ are defined at the "born level", i.e. before the decay leptons emit photons via QED final state radiation.

3.1.1 Fiducial phase-space definition

The definition of fiducial volume for W bosons in both electron and muon channels is:

- $P_T^l > 20$ GeV
- $|\eta^l| < 2.5$
- $P_T^\nu > 25$ GeV
- $M_T^W > 40$ GeV

where P_T^l and P_T^ν are the charged lepton and neutrino transverse momentums respectively, η^l is a lepton pseudo-rapidity, and M_T^W is the transverse mass, defined as:

$$M_T^W = \sqrt{2P_T^l \cdot P_T^\nu [1 - \cos(\phi_l - \phi_\nu)]}, \quad (3.5)$$

where ϕ_l is an azimuthal angle of the charged lepton and ϕ_ν is an azimuthal angle of neutrino.

For the Z boson measurement fiducial phase-space is defined as:

- $P_T^l > 20$ GeV
- $|\eta^l| < 2.5$
- 66 GeV $< M_Z < 116$ GeV

where M_Z is an di-lepton invariant mass.

3.1.2 Extrapolation to the 13 TeV fiducial phase-space

Since the 13 TeV inclusive cross-section measurement uses another definition of the fiducial phase space, it is possible to extrapolate cross-section to a new fiducial phase-space as:

$$\sigma_{W/Z}^{fid,13} = \frac{\sigma_{W/Z}^{fid}}{E_{W/Z}}, \quad (3.6)$$

where $E_{W/Z}$ is an additional extrapolation factor:

$$E_{W/Z} = \frac{N_{MC,gen,cut}}{N_{MC,gen,cut^{new}}}, \quad (3.7)$$

51 where $N_{MC,gen,cut^{new}}$ is the sum of the weights of Monte-Carlo events after the new set of cuts on
 52 the generator level.

53 The 13 TeV fiducial phase-space is defined as:

54 • $P_T^l > 25$ GeV

55 • $|\eta^l| < 2.5$

56 • $P_T^\nu > 25$ GeV

57 • $M_T^W > 50$ GeV

58 for the W decays and

59 • $P_T^l > 25$ GeV

60 • $|\eta^l| < 2.5$

61 • 66 GeV $< m_Z < 116$ GeV

62 for the Z measurements.

63 3.2 Ratios calculation

64 3.3 Results combination

65 3.4 PDF fits

Part III

Experimental setup

68

Chapter

4

69

The Large Hadron Collider

70 Chapter **5**

71 **The ATLAS experiment**

72

73

74 5.1 Inner detector	17
75 5.2 Calorimeters	17
76 5.2.1 Forward calorimeters	17
77 5.3 Muon system	17
78 5.4 The magnet system	17
79 5.5 Trigger system	17
80 5.6 Atlas software	17

81

82

83

84 **5.1 Inner detector**

85 **5.2 Calorimeters**

86 **5.2.1 Forward calorimeters**

87 **5.3 Muon system**

88 **5.4 The magnet system**

89 **5.5 Trigger system**

90 **5.6 Atlas software**

92

Event reconstruction

93	6.1 Tracks and vertexes	19
94	6.2 Electron reconstruction and identification	19
95	6.3 Muon reconstruction and identification	19
96	6.4 Missing transverse energy reconstruction	19
97	6.4.1 Standard Missing Transverse Energy reconstruction	19
98	6.4.2 Reconstruction of Missing Transverse Energy from hadronic recoil	20

104

6.1 Tracks and vertexes

105

6.2 Electron reconstruction and identification

106

6.3 Muon reconstruction and identification

107

6.4 Missing transverse energy reconstruction

108 Atlas detector has almost 4π coverage. This allows to calculate imbalance of energies inside calorimeter,
109 especially transversal part of it called E_T^{miss} . In W -analyses E_T^{miss} is used as a proxy for neutrino
110 from a $W \rightarrow l\nu$ decay. It leaves detector without interacting with it and that causes large energy
111 imbalance in a detector. In this section two methods of E_T^{miss} reconstruction and the reasons for
112 using non-standard one will be discussed.

113

6.4.1 Standard Missing Transverse Energy reconstruction

Standard reconstruction of E_T^{miss} at ATLAS experiment [?] uses transverse energy deposits in the calorimeter, energy losses in cryostat and reconstructed muons for a calculation:

$$E_{x(y)}^{\text{miss}} = E_{x(y)}^{\text{miss,calo}} + E_{x(y)}^{\text{miss,cryo}} + E_{x(y)}^{\text{miss,muon}}. \quad (6.1)$$

Calorimeter term is using information from reconstructed physics objects for calibration of cell response. The total transverse energy in calorimeter is defined as:

$$E_{x(y)}^{\text{miss}} = E_{x(y)}^{\text{miss},e} + E_{x(y)}^{\text{miss},\gamma} + E_{x(y)}^{\text{miss},\tau} + E_{x(y)}^{\text{miss,jets}} + E_{x(y)}^{\text{miss,SoftTerm}} + E_{x(y)}^{\text{miss},\mu}. \quad (6.2)$$

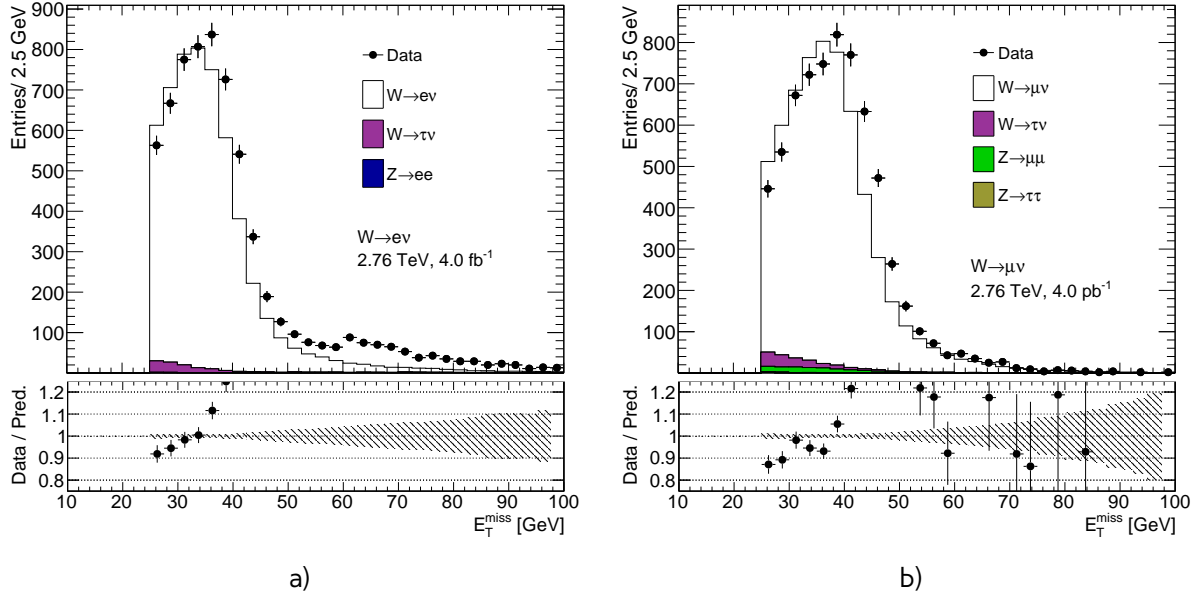


Fig. 6.1: Missing transverse energy distribution for a) the $W \rightarrow ev$ selection and b) the $W \rightarrow \mu\nu$ selection from Chap. 10. E_T^{miss} calculated using the standard ATLAS algorithm. The expected contributions from all backgrounds are estimated with Monte Carlo simulations, except for QCD background that is not included. All Monte-Carlo corrections from Chap. 11 are applied. There are visible discrepancies between data and MC, that cannot be explained by the contribution of QCD background, which is expected mainly in the low E_T^{miss} region (Sec. 13.1).

where each term is calculated as a negative sum of the calibrated reconstructed objects, projected onto the x and y directions. Each jet with energy $P_T > 20$ GeV is corrected for a pile-up and a jet energy scale is applied. Soft term is calculated from topoclusters and tracks, that are not associated with high-pt objects. To avoid double counting, muon energy loss in the calorimeter is subtracted from E_T^{miss} . The E_T^{miss} muon term is calculated from the momenta of muons measured in a range of pseudorapidity. Since pileup has a significant effect on a E_T^{miss} performance several methods of pileup suppression are used [?].

The runs at 2.76 TeV are characterized by a low pileup (mean number of interaction per bunch crossing < 1.0), so the usage of a procedure optimized for high pileup 8 TeV runs may not be optimal. It was examined and figured out, that there are big discrepancies between E_T^{miss} distributions for data and MC simulation, as shown on a Fig. 6.1, where the missing transverse energy for data is compared to signal and background MC predictions.

The differences are visible in both electron and muon channels and cannot be explained by the (missing on the control plots) contributions from the QCD background, which is expected mainly in the low E_T^{miss} region (see Sec. 13.1).

6.4.2 Reconstruction of Missing Transverse Energy from hadronic recoil

Different way of E_T^{miss} calculation was developed for W and Z decays by W mass measurements group [?]. This procedure based on the requirement of balance in transverse momentum of a W-

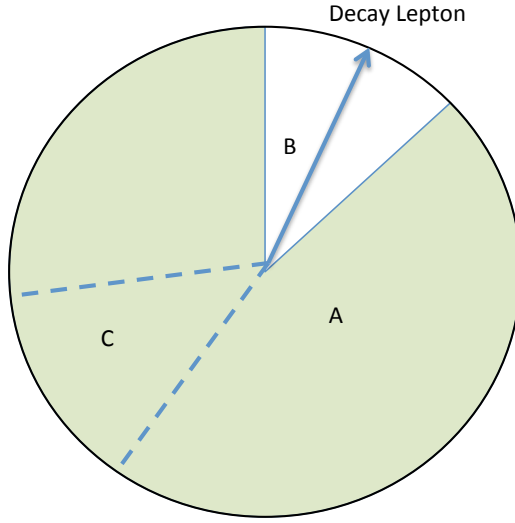


Fig. 6.2: Definition of different zones in the calculation of the cluster-based hadronic recoil. Zone B is excluded from hadron recoil calculation because it contains decay lepton. To describe properly overall acitivity it is replaced by the zone C, rotated in the direction of B. Zone A corresponds to the rest of the calorimeter [?].

boson and the initial (quark-gluon) state radiation:

$$\vec{P}_T^W = \vec{P}_T^l + \vec{P}_T^\nu = \sum \vec{P}_T^{ISRquarks,gluon}, \quad (6.3)$$

where $\sum \vec{P}_T^{ISRquarks,gluon}$ is a transverse momentum of partons from initial state radiation, also called hadronic recoil (HR), \vec{P}_T^l and \vec{P}_T^ν are the transverse momentum of lepton and neutrino respectively. Therefore, E_T^{miss} can be determined as:

$$E_T^{miss} = -P_T^\nu = -HR + P_T^l \quad (6.4)$$

This procedure assumes, that recoil arises from one single leading jet, and the rest is coming from a soft hadronic activity. The hadronic recoil is computed as a vector sum of calorimeter clusters:

$$HR = \sum_{i=0}^{N_{topo}} \vec{p}_T^{topo} \quad (6.5)$$

while a scalar sum of all transverse energy corresponds to the hadronic activity in the event:

$$\sum E_T = \sum_{i=0}^{N_{topo}} E_T^{topo} \quad (6.6)$$

¹³⁰ To avoid double counting of lepton energy losses in the calorimeter, the clusters inside a cone with
¹³¹ radius $dR = 0.2$ around the lepton direction are excluded from this calculation. To compensate for the
¹³² subtracted soft activity from the cone, a replacement cone is added (Fig. 6.2). This cone is defined

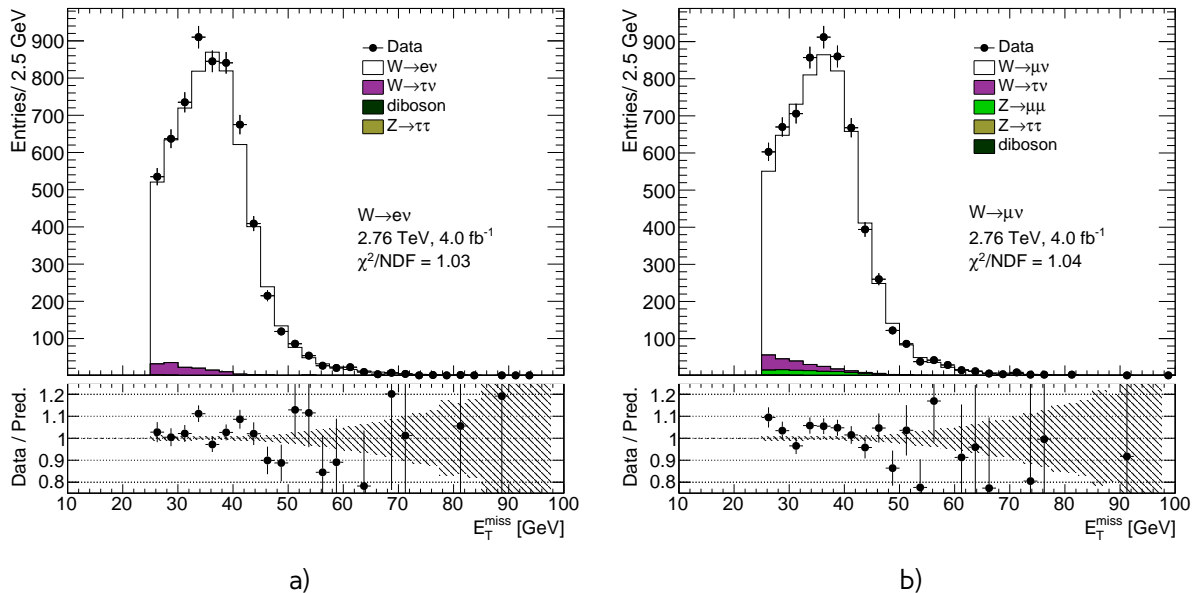


Fig. 6.3: Missing transverse energy distribution for a) the $W \rightarrow e\nu$ selection and b) the $W \rightarrow \mu\nu$ selection from Chap. 10. E_T^{miss} calculated using the hadronic recoil algorithm. The expected contributions from all backgrounds are estimated with Monte Carlo simulations, except for QCD background that is not included. All Monte-Carlo corrections from Chap. 11 are applied.

as a cone at the same pseudorapidity, but a different ϕ . It should be far from any other lepton and hadron recoil direction. The cone is then rotated to the original lepton direction. This definition does not take into account the jet reconstruction aspects.

Fig. 6.3 shows the control plots for the distributions of missing transverse energy calculated using the hadronic recoil procedure. In both electron and muon channels the agreement between data and MC simulation is much better than in case of the standard procedure described in a previous chapter. It was decided to use hadronic recoil E_T^{miss} reconstruction method in 2.76 TeV analysis.

141

Monte Carlo simulation

142 The Monte Carlo (MC) method was invented by scientists working on the atomic bomb in the 1940s.
 143 Its core idea is to use random samples of parameters or inputs to explore the behavior of a complex
 144 system or process. Nowadays, MC experiments are essential part of research in both theoretical
 145 and experimental particle physics. This chapter gives an overview of ATLAS experiment simula-
 146 tion scheme, simulation methods and software used. Also, a techniques for fast simulation will be
 147 discussed.

148

7.1 ATLAS chain of MC production

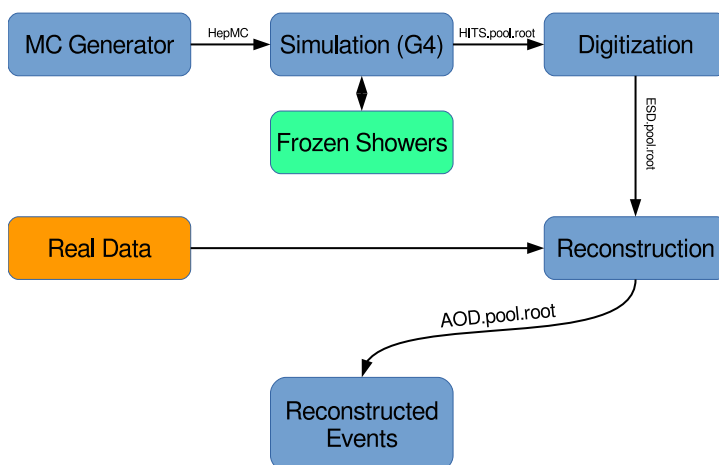


Fig. 7.1: Diagram of the ATLAS MC production chain

149 Monte Carlo method allows to perform different analysis, generate predictions for comparisons
 150 with data, study detector or selection algorithms performance. All of these applications require
 151 accurate MC predictions. Simulation software expects to use precise physics models for sampling
 152 and have large enough statistics, to exclude statistical uncertainties (usually 5 times more, than
 153 expected in a data). ATLAS simulation software is integrated into Athena framework and usually used
 154 during large production of events. Simulation chain is generally divided into 4 main steps (Figure 7.1):

155 **Event generation** Simulation of hard interaction and a resulting high-energy particles parameters.
 156 This step is independent of ATLAS detector geometry.

157 **Simulation** Simulation of energy depositions ("hits") which are produced by a final state particles.

158 **Digitalization** Simulation of detector response using "hits" information: first, inputs to the read out
 159 drivers (ROD's), called "digits" are constructed, then, ROD functionality is emulated. Detector
 160 noise effects are added at this stage.

161 **Reconstruction** Production of the Analysis Object Data (AOD) files, which are containing sufficient
 162 information for physics analysis. This stage is identical for both data and MC

163 Additionally, the pileup effects are added to MC by overlaying simulation of the hard interactions
 164 with simulation of soft inelastic scatterings. This scheme allows to use computing resources more
 165 efficiently, than with a single-step simulation, and simplifies software validation, since it is possible
 166 to reuse files from previous stages. In the following sections event generation and simulation will be
 167 described in more details.

168

7.2 Event generators

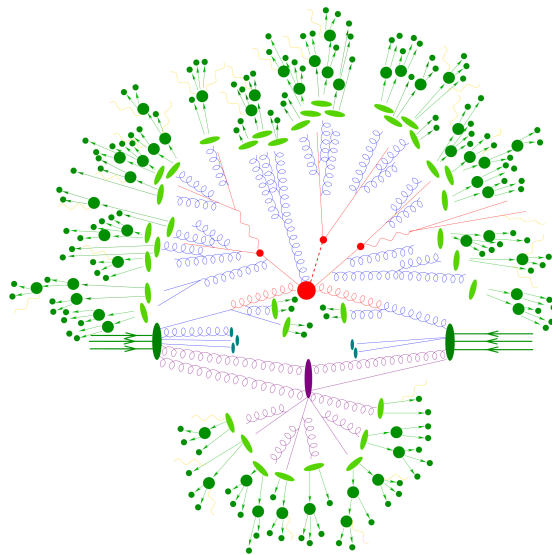


Fig. 7.2: Schematic view of a $t\bar{t}H$ event produced in a pp-collision: the hard scattering is shown as a red blob with the solid and dashed lines as the resulting three particles. Independently happening multi-particle interactions are indicated by the violet blob. Parton showers are shown with curly lines. Hadronization yields hadrons as shown in light green, while the final state particle are dark green.

169 The outcome of the hard interaction could be simple scattering of the hadron elementary con-
 170 stituents, their annihilation into new resonances or a combination of two. This can lead to a final
 171 state with a large particles multiplicity. The main goal of event generator is to provide a complete
 172 picture of this final states: description of the particle types and momentia on event-by-event ba-
 173 sis. The factorisation theorem [?] allows to make event generation in independent stages, which are
 174 dominated by different dynamics. Schematic plan of simulation of ttbar event is shown in Figure ??:

175 **Modelling of hard subprocess** Hard subprocess happens at the smallest times and distances,
 176 where the colliding partons are considered free. Process of interest is simulated by selecting

177 production channels and calculating corresponding matrix elements (ME) in the desired level of
 178 accuracy in perturbation theory . Most of the generators have leading order or next to leading
 179 order ME in α_s .

180 **Parton showering** Quarks and gluons from hard process can radiate secondary quarks and gluons,
 181 resulting in the dozens of additional partons associated with the event. This process is
 182 calculated as step-by-step evolution of momentum transfer scales from highest (hard subprocess),
 183 to the lowest (around 1 GeV). There is a possibility of double counting between showers
 184 and hard subprocess. This can be avoided using matching approaches, for which higher order
 185 corrections to ME are integrated with parton showers, or merging strategy, where jet resolution
 186 scale is used as a threshold between matrix elements and parton showers.

187 **Hadronisation** Final stable color-neutral particles, what can be detected in experiment, are formed
 188 during hadronisation. This occurs at larger nonperturbative scales and usually implemented
 189 using different phenomenological models.

190 **Modelling underlying event** Parallel to the main process other collisions of partons can occur,
 191 called underlying event. These additional interactions can produce partons which contribute to
 192 the final state. This is one of the least understood aspects of hadronic collisions.

193 The current analysis uses samples generated with the following generators:
 194 Powheg [?] Powheg is a generator with NLO ME [?], that can be interfaced with other generators (such
 195 as Pythia or Herwig) for higher precision of showering.
 196 Pythia [?] Pythia is a general purpose generator for hadronic, hadron-lepton and leptonic collisions.
 197 It can model initial and final state showers, hadronisation and decays, underlying event (via
 198 multi-parton interactions). Pythia contains a library with around 240 processes with LO ME. It
 199 uses Lund String model [?] for hadronisation.

200 Herwig [?] Herwig is a LO general purpose event generator for simulation lepton-lepton, hadron-
 201 lepton and hadron-hadron collisions. The main difference between Pythia and Herwig is that
 202 it uses angular ordering in the parton showers and also models the hadronisation step based
 203 on the cluster fragmentation

204 Sherpa [?] Sherpa is an event generator, that uses tree-level leading order matrix element for a hard
 205 scattering and featuring its own implementation of parton shower and hadronisation models.

206 Photos [?] Program used for generation of QED radiative corrections in W and Z decays.

207 Tauola [?] Generator, used to describe leptonic and semi-leptonic τ -decays.

208 7.3 Simulation in Geant4

209 After event generation, simulation software obtains hardware response for final state particles. The
 210 main method used by ATLAS experiment, referred to as *Full Simulation*, makes use of the Geant4 [?].
 211 It is C++ based toolkit for the simulation of the passage of particles through matter. It is used in a
 212 wide range of experiments in high energy and nuclear physics.

213 Geant4 can simulate complex detector structures with sensitive detector material and correspond-
 214 ing infrastructure. It can also calculate basic properties of materials, like radiation and interaction

length. For detector Geant4 stores "hits" information - snapshots of physical interactions. In Geant4 events and particles are simulated separately and each particle is moved in steps. Size of each step is chosen to preserve both CPU performance and required precision.

Physics interactions are treated as a set of discrete processes. They could be handled either at rest, along step or after it. Geant4 package has different models and approximations for hadronic and electromagnetic processes. Some of them are approximate and computationally fast. It allows to choose set of the models, called physics list, depending on particular requirements. There are several reference physics lists, that are validated for each new release of Geant4 software. ATLAS experiment uses one of this lists.

Most of the computing resources are taken by a mass MC production, required for each data taking periods. Uncertainties of some of Run-I analyses are dominated by available MC statistics. It is possible to improve in CPU usage by tuning physics list or replacing a complex magnetic field maps by a parametrisation. Also there are long-term developments for multi-threading and vectorisation of the code.

Yet, Run-2 has a higher pileup and luminosity, so even more MC events are needed. This means that fast and accurate simulation approach is essential. During simulation largest time is spend on calorimeters. This is the motivation for development of fast calorimetry techniques.

There are two main methods used at ATLAS:

- Parametrisation of calorimeter cells response. Spacial energy response is simulated using longitudinal and lateral energy profiles.
- Frozen Showers. This technique will be described more detailed in Chap. 8

237

Frozen Showers

238

240	8.1 Problem description	29
241	8.2 Generation and use in simulation	32
242	8.2.1 Libraries tuning	33
243	8.3 Machine learning based bin finding procedure	34
244	8.3.1 Machine learning introduction	34
245	8.3.2 Model description	36
246	8.4 Validation of the new libraries	40

250 As it was mentioned in a previous chapter, fast simulation techniques are the essential part of
 251 Monte-Carlo production at ATLAS experiment. Typical time for a simulation of $t\bar{t}$ event is around 1
 252 minute, and most of the time is spend on a simulation of particle interaction in calorimeters. This
 253 motivates a development of fast calorimetry techniques.

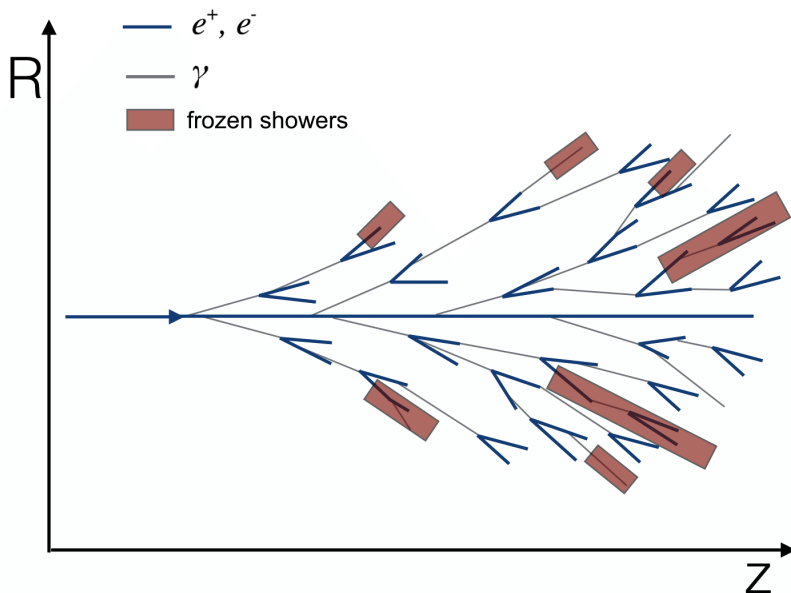


Fig. 8.1: Diagram showing the shower substitution of the low-energy particle, during the high-energy particle simulation. Some of the showers from a particles, substituted by frozen showers method marked by a red squares

Table 8.1: Main parameters used for the frozen shower libraries

The general frozen showers parameters	
Detectors used	FCAL1, FCAL2
Type of the particle	photons, electrons, neutrons
Energy range	$E_\gamma < 10 \text{ MeV}$, $E_e < 1000 \text{ MeV}$, $T_n < 100 \text{ MeV}$

254 Frozen showers is currently the main fast calorimeter simulation approach used at ATLAS exper-
 255 iment. In this chapter we will discuss main principles,difficulties and current developments in this
 256 method.

257 Frozen shower method uses pre-simulated "frozen" showers instead of the full simulation. This
 258 is allowing to reduce time spend on a simulation of a large amount of low energy sub showers.
 259 This method is allowing to have a 25% speedup in simulation. It is required to have an in advance
 260 generation of a libraries for each detector and particle used in this method. Each shower from a
 261 library stores it's lateral and transverse size and list of the all energy depositions inside sensitive
 262 material (hits) with information about their energy, position and time. During a simulation, if energy
 263 of secondary electron falls below cutoff energy it is replaced by a shower from a library, as shown
 264 on a Fig. 8.1. Main parameters used in ATLAS simulation are summarized in a Tab. 8.1.

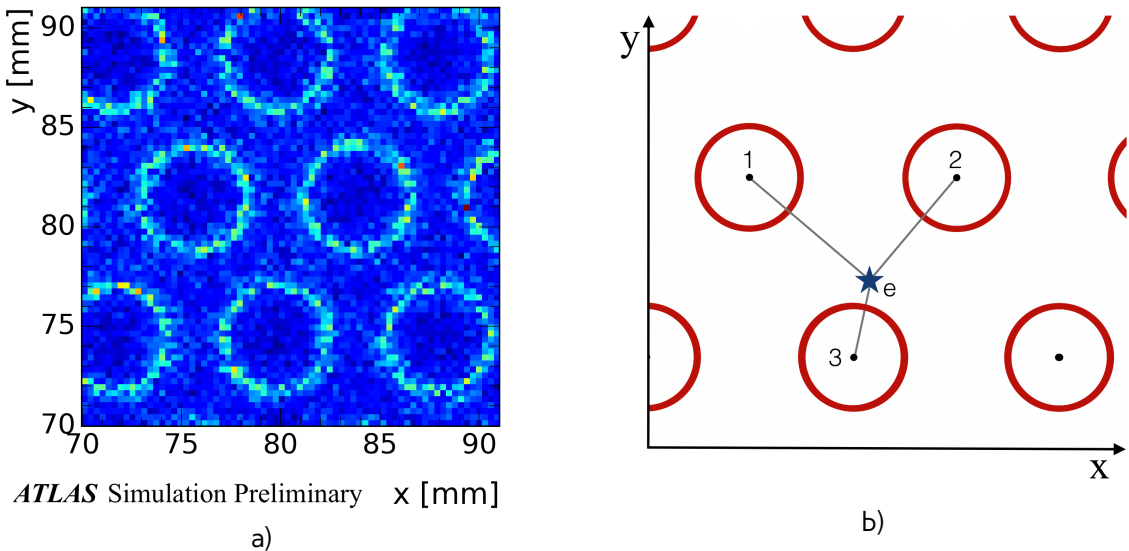


Fig. 8.2: a) Shower energy response histogram in the x vs y plane for electrons, generated with uniformly distributed x and y and energy less than 1 GeV. Light circles are corresponding to a showers, started inside a LAr gaps with on average higher energy response, while the dark parts are corresponding to dead material respectively with smaller sum of the "hits" energy. b) Distance to a closest rod center scheme, where $d_{rod} = \min(d(1,e), d(2,e), d(3,e))$. Rod centers and liquid argon gaps are shown by black and red circles respectivelly.

265 8.1 Problem description

266 Fast simulation of forward calorimeters (FCAL) is a complicated task due to its complex structure.
 267 As it was mentioned in a Sec. 5.2.1 FCAL consists of hexagonal absorber cells with anode tube and
 268 cathod rod in the cell center and liquid argon in the gap between rod and tube. In order to simulate
 269 resolution of high energetic electrons, good fast simulation technique should take this feature of
 270 large amount of non-uniformly distributed sensitive material.

Resolution of electron inside calorimeter can be written as:

$$\frac{\sigma}{E} \approx \frac{1}{\sqrt{E}} \oplus \frac{1}{E} \oplus const, \quad (8.1)$$

271 where symbol \oplus indicates a quadratic sum. The first term is 'stochastic term', which includes intrinsic shower fluctuations, second takes into account readout noise effects and pile-up fluctuations.
 272 Constant term derives from non-uniformities in a detector, causing large fluctuation of the energy loss. Resolution of high-energy electrons is mostly dominated by the constant term.

Fluctuations due to a detector design are visible in a simulation of small energy electrons, generated inside a different points in forward calorimeter. Shower energy E^{shower} distribution in the x vs y plane is showed on Fig. 8.2, where shower energy is defined as:

$$E^{shower} = \sum E_i^{hits}, \quad (8.2)$$

275 where E_i^{hits} is an energy of i-th shower deposit inside sensitive material. Periodic structure resembles
 276 the calorimeter design, where light circles are corresponding to gaps with liquid argon. It could be
 277 reduced to a 1-d problem by introducing d_{rod} distance to a closest rod center.

278 Typical electron substituted by a frozen showers coming from a simulation of high energy electrons
 279 have a relatively small energy (Fig. 8.3 a)). Mean number of depositions in a sensitive material in a
 280 "frozen" shower is around 5 and this value rises with electron energy (Fig. 8.3 b). Fig. 8.4 presents a
 281 distribution showers for electrons with energy below 1 GeV coming from initial electrons with energy
 282 1 TeV in the distance to a closest rod center vs shower energy plane. Liquid argon gap is marked by

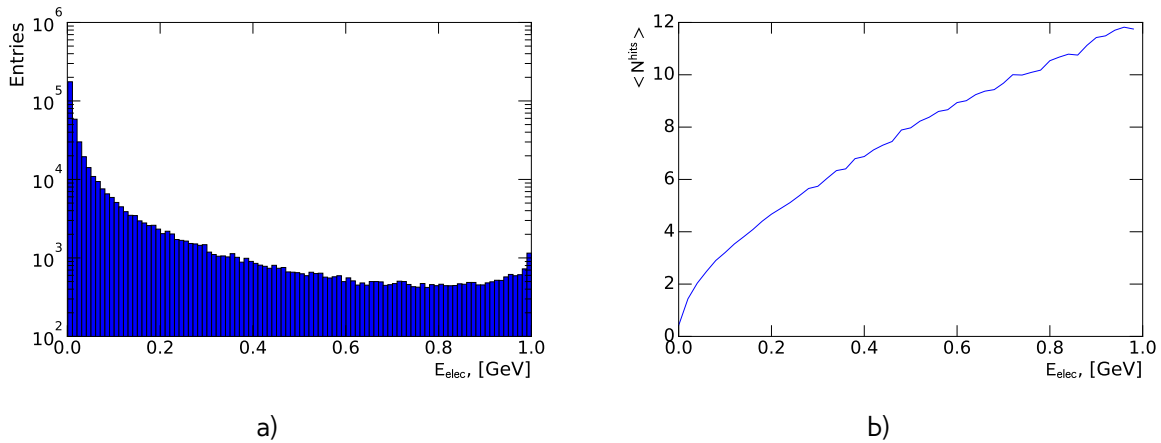


Fig. 8.3: Distribution a) electron energies and b) mean number of hits in a shower vs energy of electron for electrons with energy less than 1 GeV coming from initial electron with energy 1 TeV.

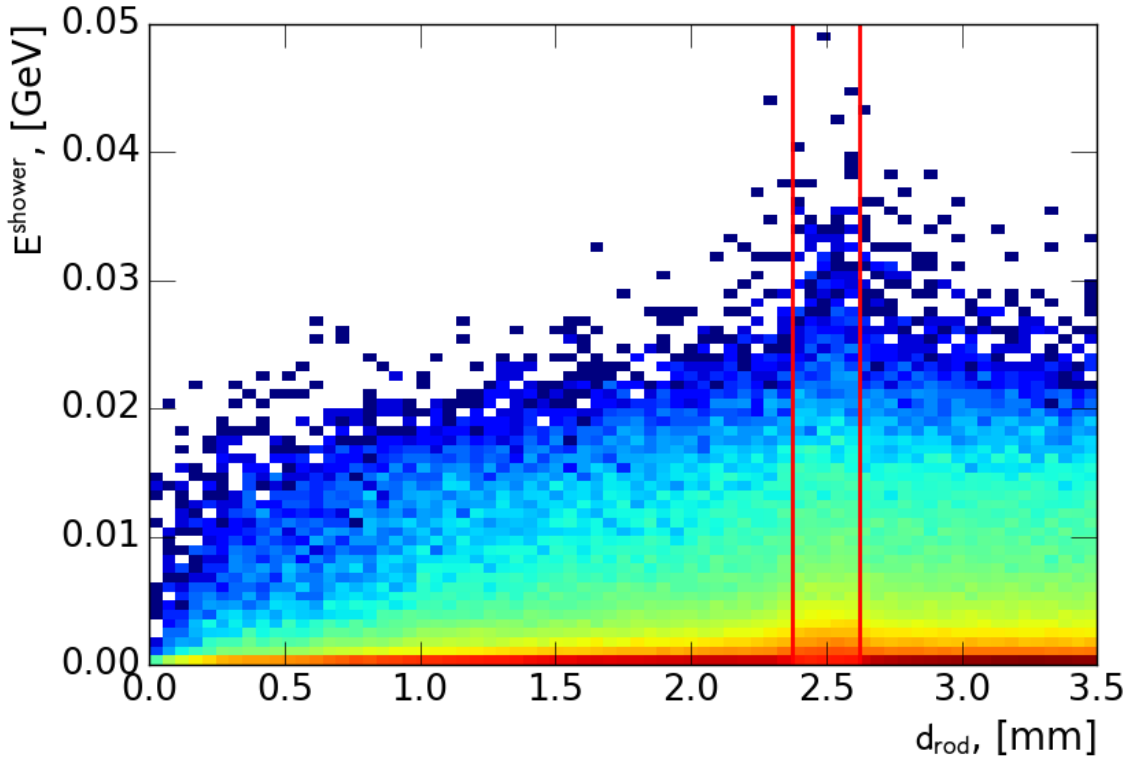


Fig. 8.4: Distribution of electron showers for electrons with energy less than 1 GeV coming from initial electron with energy 1 TeV in distance to a closest rod center vs shower energy plane. Position of a liquid argon gap is noted by a red lines. There is visible difference in shower properties between showers inside and outside of the liquid argon gaps

a red lines. There is a clear difference in a showers energies between electrons born in a sensitive and dead material. Difference in a shower properties are also visible for number of hits (Fig. 8.5 a) and standard deviation energy of hits in shower (Fig. 8.5 b) distributions. Size of this differences depends on a electron energies and higher for a smaller energies (Fig. 8.6 a) and less significant for a higher energies (Fig. 8.6 b). This fact combined with energy distribution states an importance of proper simulation non-uniformities for showers coming from a small energy electrons.

On another hand, use of the frozen showers in a small energy region can be suboptimal because of the small number of energy depositions in a shower. For electrons with energy less than 30 MeV 90% of the showers has zero depositions and just 0.5% of showers are having more than 1 hits (Fig. 8.7). Below this energy single energy spot model have showed better performance in simulation.

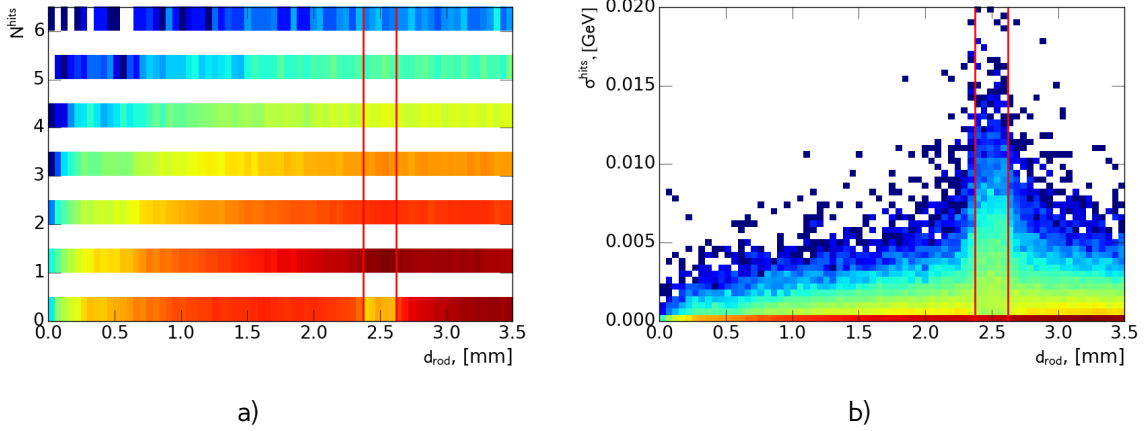


Fig. 8.5: Distribution of electron showers for electrons with energy less than 1 GeV coming from initial electron with energy 1 TeV in distance to a closest rod center vs a) number of hits in a shower plane and b) standard deviation of hits in a shower energy. Position of a liquid argon gap is noted by a red lines. There is visible difference in shower properties between showers inside and outside of the liquid argon gaps

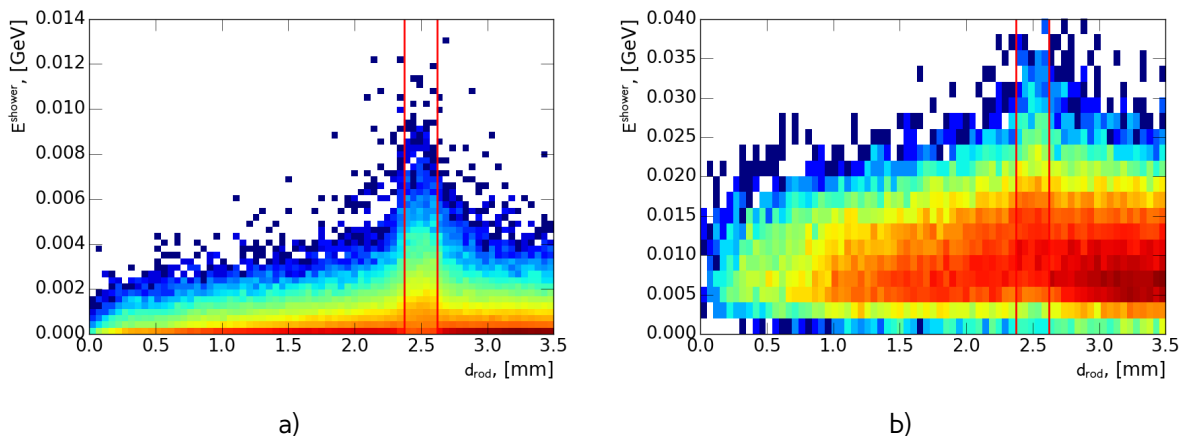


Fig. 8.6: Distribution of electron showers for electrons with energy a) less than 100 MeV and b) higher than 300 GeV coming from initial electron with energy 1 TeV in distance to a closest rod center vs shower energy plane. Position of a liquid argon gap is noted by a red lines. Size of the difference in a shower properties depends on the energy of the electrons and higher for smaller energies

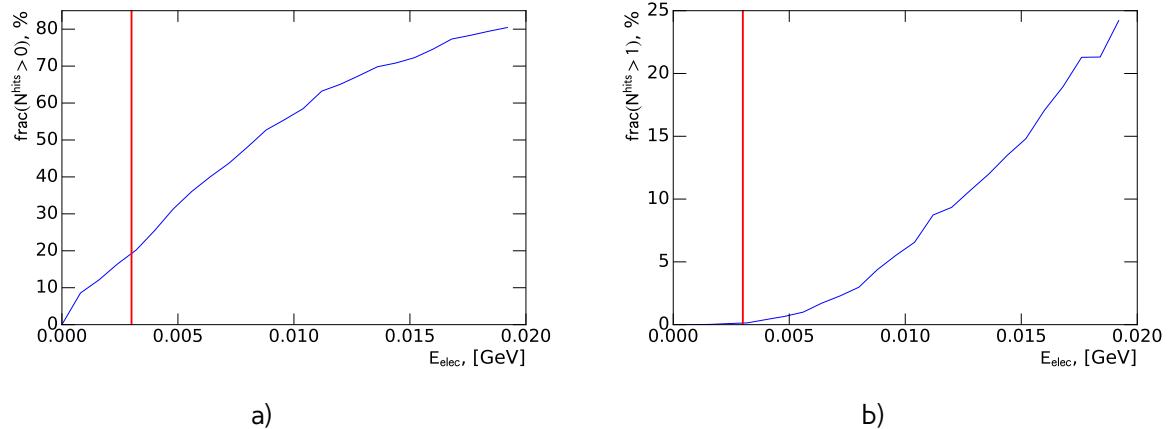


Fig. 8.7: Distribution of fraction of showers with a)at least 1 b) at least 2 depositions inside sensitive material depending on a initial electron energy. Red line denotes 30 MeV lower limit for a frozen showers method.

293 8.2 Generation and use in simulation

294 As it was mentioned in introduction frozen showers method consist of the 2 stages: generation of
 295 libraries and use in simulation. Generation needs to be repeated for each significant change in a
 296 physics processes description in Geant4 or in a description of detector. Showers are stored in a
 297 library in pseudorapidity and distance to a closest rod center bins, while energy remains unbinned.
 298 Distance binning was introduced to describe fluctuations from Sec. 8.1. Position of the liquid argon
 299 gap bin is corresponding to a real gap position.

300 In order to have proper energy distribution for a generation of library particles coming from
 301 a simulation of physical process (usually $t\bar{t}$ or high energy electrons) are used. For each particle
 302 eligible for frozen showers use parameters are saved in a HepMC (reference) format for a later
 303 use. On a second stage, these particles are propagated through the calorimeter using standard
 304 ATLAS simulation infrastructure. Each hit is saved as a shower inside library in a corresponding
 305 pseudorapidity and distance bin.

306 Additionally, in order to save disc space as well as a memory consumption, hit information is
 307 compressed. This compression is done in a two steps:

308 **Hit merging** if the distance between any two hits is smaller, than a given parameter R_{min} , then
 309 hits are merged into one deposit at the energy weighted center of them. This process is done
 310 iteratively.

311 **Truncation** hits whose energies are below the fraction f of the total energy sum of all hits, are
 312 truncated. The energy of remaining hits is rescaled back to preserve the total deposited energy.

During simulation, if an energy of a particle falls below cut-off energy, the particle algorithm examines resulting shower containment. It checks that particle is far from the edges of calorimeter, so what shower will be by 90% inside calorimeter. This depends also on a energy of particle, because shower sizes are growing with energy. The algorithm searches for a shower with the closes energy in a corresponding pseudorapidity and distance bin. Shower is a rotated in a direction of particle. In

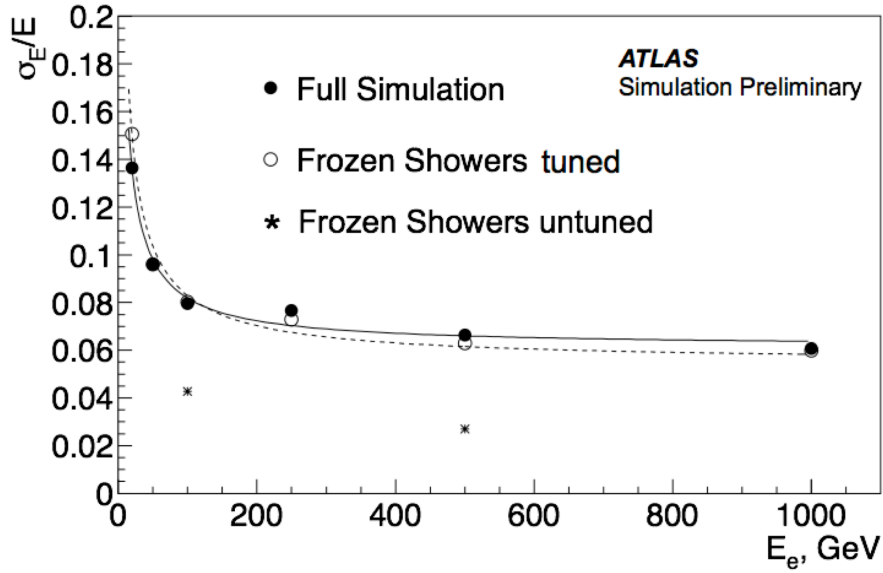


Fig. 8.8: Electron resolution for full simulation, tuned and untuned frozen showers. Electrons simulated with frozen showers libraries before tuning (star points) have twice smaller resolution, than an electrons from full simulation (circles). Tuning (black dots) is allowing to gain better agreement with full simulation.

order to correct differences in energy, each hit in a shower is scaled as:

$$E_{hit}^{new} = E_{hit} \cdot \frac{E_{part}}{E_{part,lib}}, \quad (8.3)$$

where E_{hit} is the energy of the hit, E_{part} is the energy of the particle and $E_{part,lib}$ is the energy of the particle from a library. Then particle is removed and substituted by a resulting shower. Later, reconstruction algorithm uses hits from a frozen shower as a usual energy depositions in a sensitive material.

8.2.1 Libraries tuning

Frozen showers method gives a good agreement with a full simulation for a shower shape variables(Sec. 8.4), however resolution of the reconstructed electrons is around 2 times smaller(Fig. 8.8), than in a full simulation. It can be interpreted as a lack of the showers from liquid argon gap in a simulation. Most of this effect is coming from an electron libraries. This means that this libraries are requiring additional reconstruction-based tuning after generation.

Usual tuning consists of 2-step manual procedure:

Changing bin width On this stage width of the liquid argon bin is enlarged. This is causing larger size of the fluctuations, that leads to a higher resolution and a mean energy of reconstructed electrons

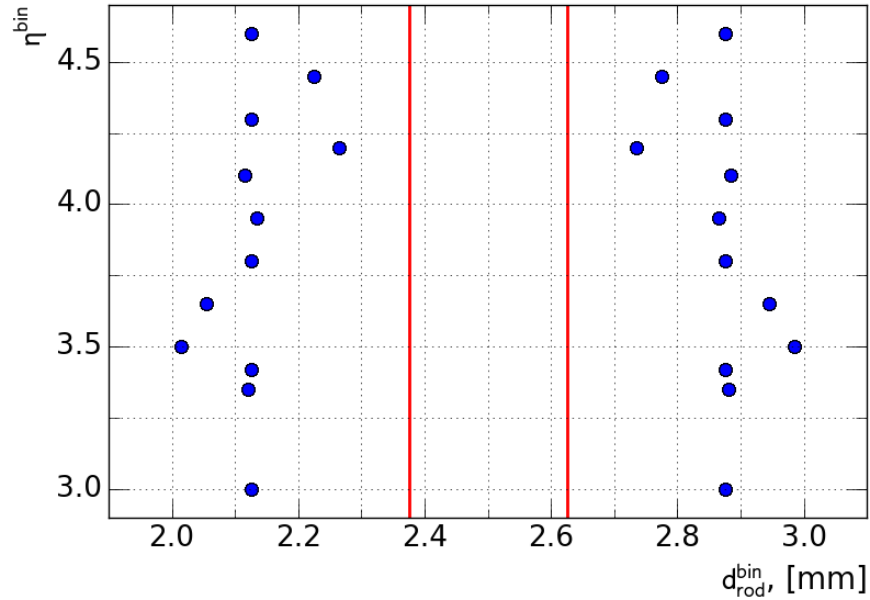


Fig. 8.9: Position of gap bins for different η bins in old libraries after tuning. Dots are corresponding to a limits of each bin. Red lines are denoting original position of bins, that are corresponding to a position of a liquid argon gap in the calorimeter.

327 **Shower energy scaling** In order to correct introduced shift in a mean energy shower energy is
328 reduced by rescaling all of the hits in a shower.

329 It is repeated iteratively in each pseudorapidity bin separately till the desired agreement is obtained.
330 The resulting bin positions are shown on a Fig. 8.9. This method allows to have a relatively good
331 agreement with full simulation (black dots on Fig. 8.8). However, it is necessary to repeat this
332 procedure for each new libraries generation and requires significant tuning effort, that makes it not
333 optimal.

334 8.3 Machine learning based bin finding procedure

335 Since frozen showers are planned to be used in Run-2 Monte-Carlo production, there is a need
336 for a more automatic procedure of library generation with proper electrons resolution. One of the
337 possible ways is to choose different position of liquid argon bin during libraries generation using
338 machine learning tools. In this section automatic bin finding procedure will be discussed.

339 8.3.1 Machine learning introduction

340 Machine learning is a set of algorithms, what allows computers to learn and give a predictions without
341 being specifically programmed. This is a modern field of computer science, that is wildly used in a
342 different fields like computer vision, natural language processing, data science etc. There are two
343 main types of machine learning algorithms: supervised, where example of desired output is given by
344 the "teacher" and the goal is to learn a general rule, that maps inputs to outputs and unsupervised

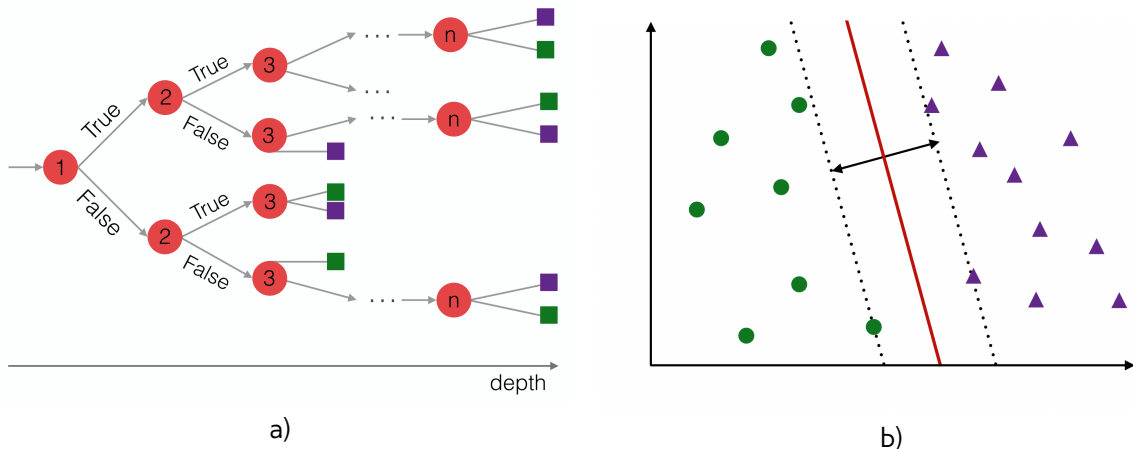


Fig. 8.10: Schematic representation of machine learning algorithms, used in the analysis for a classification. Green figures are representing first class of the events, whereas violet ones belong to a second class. a) Representation of a binary decision tree structure: red circles are corresponding to a node, that are split in the respect to the one of the features. Squares represent leafs, where all of the events are classified to a certain class. Depth of the tree is calculated as a number of edges from the node to the trees first node. b) Representation of the SVM algorithm. Dividing hyperplane is shown by a solid line. The dashed lines represent the maximum margin boundaries

345 learning, then there are no labels given to algorithm, and algorithms is discovering hidden patterns
346 in data. Initial data parameters of interest, that are used in algorithm to learn are called features.

347 Machine learning algorithms can be used for solving a classification problem, where each event
348 should be identified to one of the specified classes. Since the first introduction of the machine
349 learning classifiyng algorithms called perceptron by a Rosenblatt [ref](#) many different algorithms
350 have been invented. In this analysis decision trees and support vector machines have been used.

351 **Binary decision trees**

352 Binary decision trees are one of the most commonly used machine learning algorithms for a clas-
353 sification problems in a particle physics. Schematic representation of this algorithm is shown on a
354 Fig. 8.10 a. Each node is corresponding to the one of the internal input variables and connected to
355 two branches, that are split in the respect to the a variable. The first node is called a root node.
356 Depth of the tree is a number of edges from the node to the tree's root node. Leaf node represents
357 classification or decision. For each node the best feature is selected and it's cut value are obtained
358 by calculating each possible variation in the feature set and then ranking them. One of the main
359 advantages of the decision trees is a simplicity of visualization and interpretation.

360 **Support vector machines**

Support vector machines (SVM) is a supervised machine learning algorithm which can be used for classification problems. In this algorithm each event is represented in a p-dimensional parameter space. Classification is performed by finding a the hyper-plane that differentiate the two classes

with the largest separation (Fig. 8.10 b). The hyperplane can be written as the set of points \vec{x} in a parameter space satisfying:

$$\vec{w} \cdot \vec{x} - b = 0, \quad (8.4)$$

where \vec{w} is the normal vector to the hyperplane and the parameter $\frac{b}{\|\vec{w}\|}$ determines the offset of the hyperplane from the origin along the normal vector \vec{w} . The margin hyperplanes are described by equations:

$$\vec{w} \cdot \vec{x} - b = 1, \quad (8.5)$$

$$\vec{w} \cdot \vec{x} - b = -1, \quad (8.6)$$

where $\frac{2}{\|\vec{w}\|}$ is the distance between these 2 hyperplanes, so planes with the maximum margin between should have the minimum $\|\vec{w}\|$.

Because we want to prevent each point to fall into the margin, we following constrain should be satisfied:

$$\vec{w} \cdot \vec{x} - b \geq 1 \text{ where } y_i = 1, \quad (8.7)$$

$$\vec{w} \cdot \vec{x} - b \leq -1 \text{ where } y_i = -1, \quad (8.8)$$

These equations can be rewritten as:

$$y_i(\vec{w} \cdot \vec{x} - b) \geq 1 \quad (8.9)$$

It is also possible to construct a non-linear classifier by replacing dot-product with a different *kernel* function. In this thesis, a radial basis function (RBF) kernel is used:

$$K_{rbf}(\vec{x}_i, \vec{x}_j) = e^{-\gamma|\vec{x}_i - \vec{x}_j|^2} \quad \gamma > 0, \quad (8.10)$$

where parameter γ adjusts the width of the kernel.

8.3.2 Model description

As it was mentioned in a previous sections, modules in FCAL are consisting of different types of material and showers started inside dead material are usually having smaller energies, than a sensitive material once. However, the validation (Fig. 8.8) can be interpreted as the that there are high energy showers outside of the liquid argon gap. It could be explained by the fact, that electron, created in a dead material, can cross a liquid argon gap and give a hit there as it shown in Fig. 8.11 (electron 2). These electrons would be indistinguishable from electrons, created directly in a sensitive material (electron 1 in Fig. 8.11).

It was decided to treat this electrons together with electrons created in sensitive material, and call a caused showers as a sensitive material showers. Oppositely, showers that did not crossed a liquid argon gap, are called a dead material showers. This model leads to a bigger gap.

From the definition, this model leads to the dependency of the liquid gap width on:

Electron energy Gap should get wider with higher energy of the initial electron, because of the growth of the mean free path with energy.

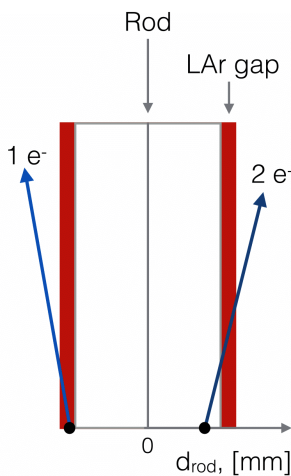


Fig. 8.11: Schematic representation of the model. Electron 1 is created in a liquid argon gap. Electron 2 is created near liquid argon gap and crosses it. This causing a smearing of sensitive material showers distribution. Electrons created in a sensitive material tend to create more energetic showers, than electrons from a dead material. However, electrons, shown on this scheme, may give similar shower and therefore be not distinguishable.

383 **Direction of the electron** Electron aligned collinearly with liquid argon gap will have smaller prob-
 384 ability to cross liquid argon gap. This probability will grow with the angle reaching its maximum
 385 at 90°

386 **Training sample**

387 Real distributions, used in simulation, have a complicated structure and depend on a physical pro-
 388 cesses simulated. Machine learning could catch these dependencies, instead of the needed ones.
 389 This is why a more simplified data as a training sample for machine learning is needed. Training
 390 sample was made by a simulation of the electrons, created in forward calorimeters. In order to treat
 391 equally high and low initial electron energy showers, the uniform distribution of the energies is used.
 392 Most of the showers have direction in η range between 3.0 and 5.0 (Fig. 8.12), that is corresponding
 393 to a position of the calorimeter. Distribution of the showers directions in different positional η bins
 394 shows, that there is indeed the correlation between direction and the position of the electrons.
 395 Because of this it was decided to use electrons with direction, uniformly distributed between 3.0
 396 and 5.0.

397 **First classifier**

398 First classifier classifier aims to classify all of the showers based on a shower parameters. It is
 399 possible to train supervised learning algorithm on pre-labeled artificially reduced training sample
 400 and then expand the classification on a full train sample.

401 Pre-labeling could be easily done from a definitions of sensitive and dead material showers based
 402 on a distance to a closest rod center (Fig. 8.13). Showers started in liquid argon gap are 100 %
 403 sensitive material showers, while showers from electrons near rod center and on the edges of the
 404 the cells can be labeled as a dead material showers, since there is a small probability for an electron
 405 to reach liquid argon gap.

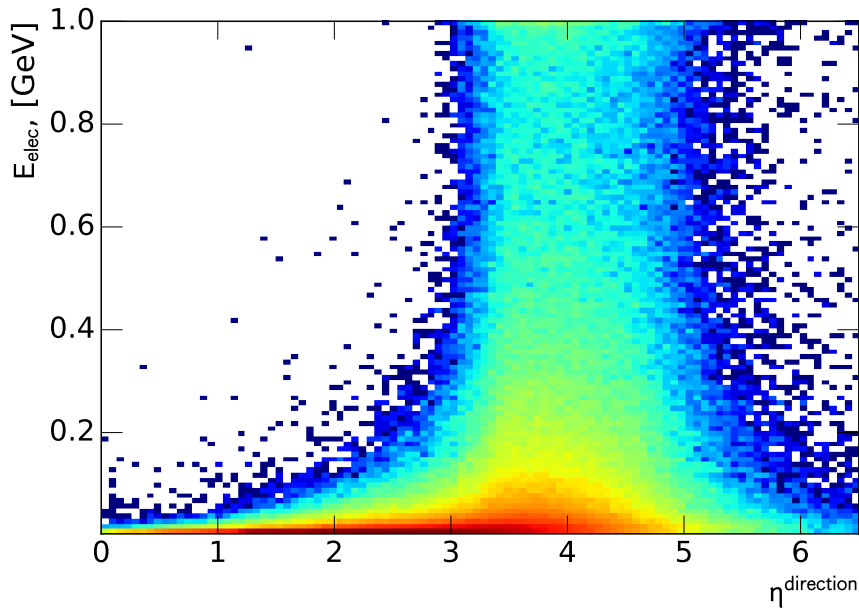


Fig. 8.12: Distribution of showers used in production of 1000 GeV electrons on shower energy vs $\eta^{momentum}$ plane.

406 For a classifier it was decided to use a simple decision trees, because it have showed good clas-
 407 sification efficiency (around 97%) on a reduced training sample. Variance of the different input
 408 parameters have been tested, and it was figured out, that the best set of the parameters is :

- 409 • Shower energy, that is equal to the sum of all "hits" in sensitive material energies in shower
- 410 • Maximum hit fraction. This quantity is calculated as energy of the most energetic hit divided
 411 by the shower energy
- 412 • RMS of the hits, calculated as a standard deviation of the hits energy in a shower

413 Predictions of the first classifier on a full training sample is shown in a Fig. 8.14 a).

414 **Second classifier**

415 Second classifier uses predictions of the first classifier as an input label. It is trying to reconstruct a
 416 best dividing hyperplane between two methods using a support vector machines. It uses as an input
 417 truth parameters of the electron, e.g. energy of the initial electron and its distance to a closest rod
 418 center. Different kernels have been tested and the best predictions have been obtained using RBF
 419 kernel (Eq. 8.10). Assuming, that $\eta^{momentum} \approx \eta^{position}$ classification is performed in each $\eta^{distance}$ bin
 420 used in a library. Example of the classifier output is shown in a Fig. 8.14 b). As it is expected from the
 421 model, gap position is getting wider with higher energies of the electron. Variation of the obtained
 422 parameters have been found small, so the mean of the parameters have been used.

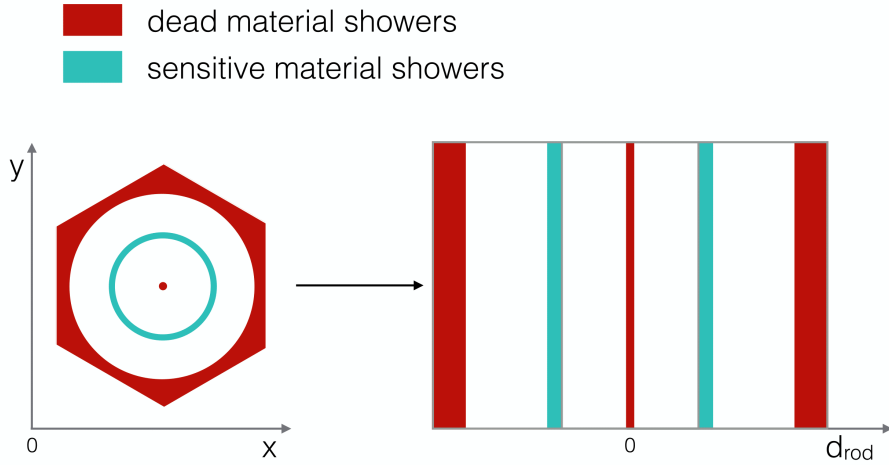


Fig. 8.13: Schematic representation of preselected data for a first classifier in x vs y plane and distance plane. Electrons, created near rod center and on the borders of the module have low probability to cross the sensitive material, while oppositely all of the electrons created inside liquid argon gap are sensitive material showers.

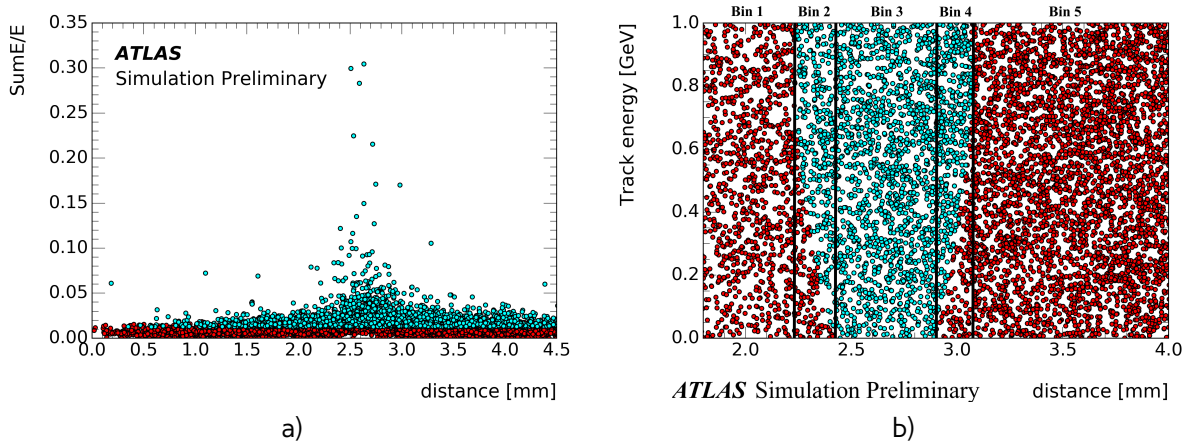


Fig. 8.14: Results of machine learning for a) first classifier b) second classifier. Cyan dots are corresponding to sensitive material showers, red - dead material showers. Black lines in Fig. b are corresponding to a resulting bin positions

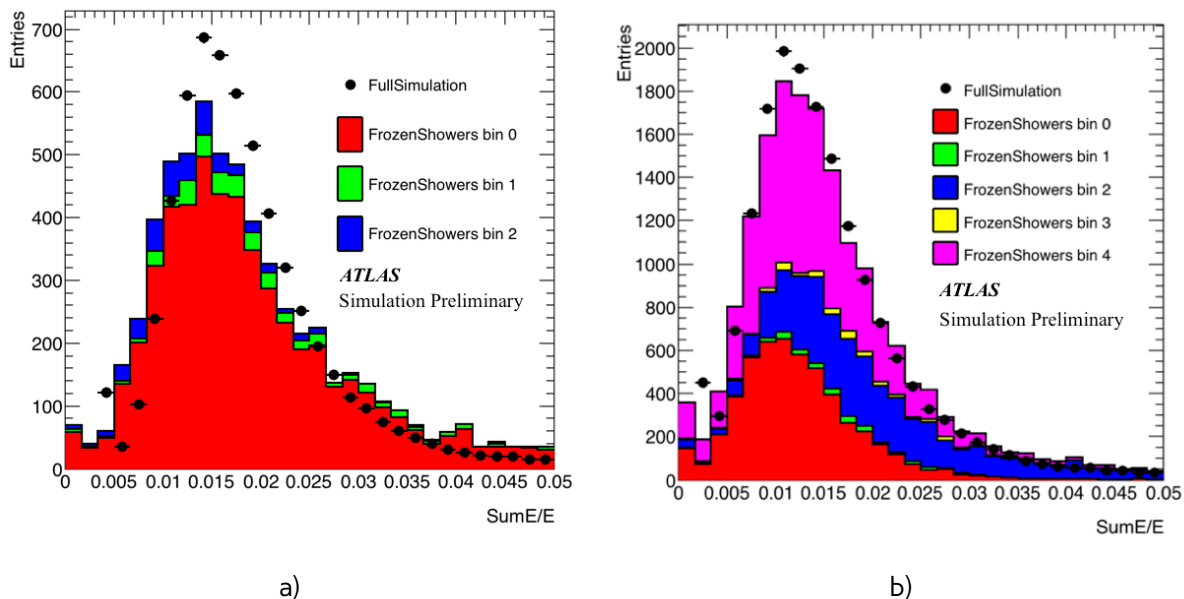


Fig. 8.15: Comparison of the distributions of shower energy divided by the energy of initial electron between full simulation and toy MC using libraries for liquid argon gap bins and 2 closest to them bins for a) old "tuned" libraries with 1 liquid argon gap bin b) new libraries binning with 3 liquid argon gap bins. There are still remaining differences between full simulation and toy MC, but new machine learning binning performs better.

Interpretation of results

Because a full new regeneration of libraries and validation on a reconstructed variables is an a time-consuming procedure, the toy Monte-Carlo method have been developed for a cross-check of classifiers and its interpretation. It uses pseudorapidity $\eta^{position}$, energy of electron and distance to a closest rod center from a data as a reference for a random generator. This simulation allows to compare shower energies and shower energy divided by the energy of initial electron (SumE/E) distributions with and distributions from a full simulation, that are considered as a reference.

Several interpretations of the bin positions have been tested and the best one is showed in Fig. 8.14 b) by a black lines. It was decided to make 3 bins corresponding to a liquid argon position instead of the only one. One contains, according to a classifier just sensitive material showers events, while in other 2 there is a mixture of dead material and sensitive material showers. The obtained positions of the liquid argon bins are wider, than a nominal ones, as expected from the model. Comparison of SumE/E distributions using toy MC on old libraries (Fig. 8.15 a) and the libraries with the new binning (Fig. 8.15 b) have showed, that we could expect a better performance on a reconstructed values.

8.4 Validation of the new libraries

438 Validation results for two different eta bins are shown on figure a) and b). In a bin this new binning
439 is performing better, than original one without any additional tuning. Unfortunately this is not true
440 for all of the bins, as we can see on a figure b). This eta bin have showed worst performance for a
441 new binning, but it is performing still better, than original binning without tuning.

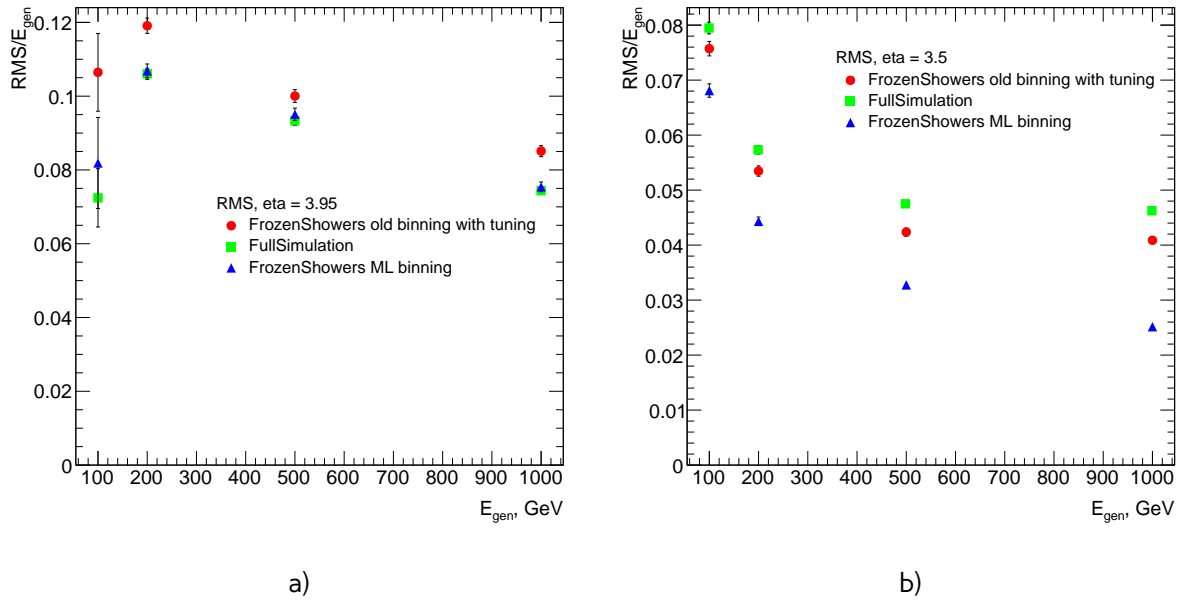


Fig. 8.16: Resolution of reconstructed electrons for full simulation, new libraries with ML binning and old tuned libraries with original binning for a) $\eta = 3.95$ b) $\eta = 3.5$

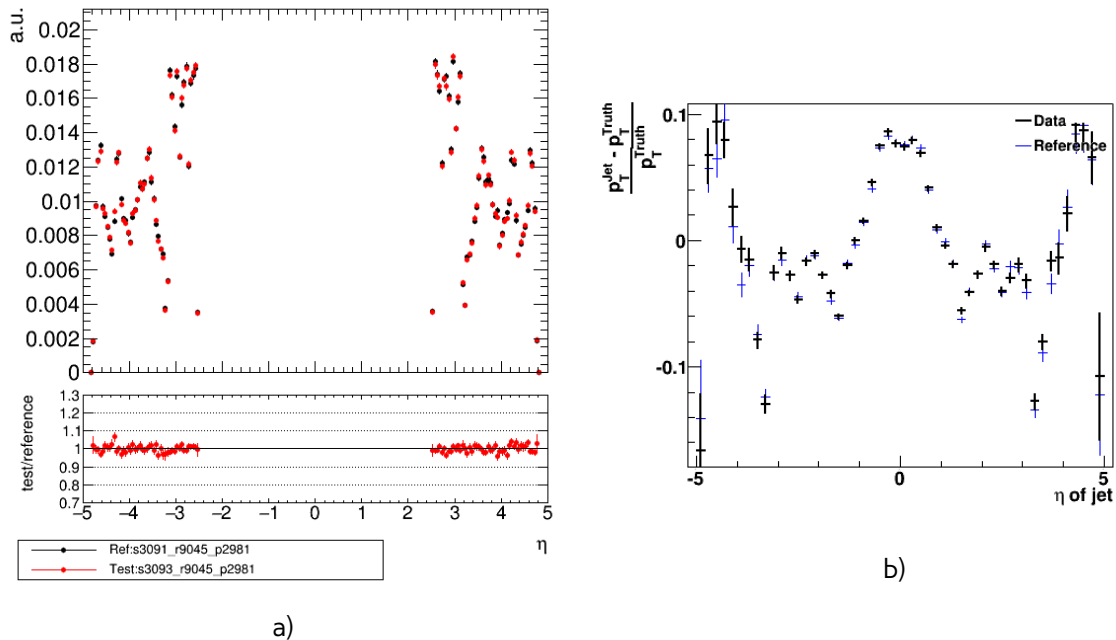


Fig. 8.17: Resolution of reconstructed electrons for full simulation, new libraries with ML binning and old tuned libraries with original binning for a) $\eta = 3.95$ b) $\eta = 3.5$

442 Validation on another objects

443 This binning was used in a production of new libraries for Monte Carlo in a Run-2. It is planned to use
444 more precise training sample for a future iterations of this procedure for improving performance of

445 outlying eta bins.

446

Chapter

9

447 Data and Monte-Carlo samples

448 9.1 Data sample

449 9.2 Monte-Carlo samples

450

Part IV

451

The Measurement

452

Chapter 10

453

Selection

454 Selection criteria is the set of requirements, that is applied both on data and MC. Analysis depends
 455 on a selection, that can separate process of interest (signal) from other processes. For $pp \rightarrow W \rightarrow$
 456 $ev/\mu\nu$ and $pp \rightarrow Z/\gamma^* \rightarrow ee/\mu\mu$ selection criteria can be divided into 3 groups: data quality, lepton
 457 and boson cuts. In this chapter all of them will be discussed and a cut flow presented.

458 10.1 Data quality cuts

Table 10.1: Selection criteria

Event selection	
Single lepton trigger	
Good Run List	
Reject events with LAr errors	
Number of tracks at primary vertex ≥ 3	
Electron Selection	
EF_e15_loose1	EF_mu10
$P_T^l > 20\text{GeV}$	$P_T^l > 20\text{GeV}$
$ \eta^l < 2.47$	$ \eta^l < 2.5$
excluding $1.37 < \eta^l < 1.52$	
OQ cut	staco reconstruction chain
Medium electron identification	Medium muon identification
$P_T^{cone,20} < 0.1$	$P_T^{cone,20} < 0.1$
W boson selection	
$E_T^{\text{miss}} > 25 \text{ GeV}$	
$M_T^W > 40 \text{ GeV}$	$66 < M^Z < 116 \text{ GeV}$
Z boson selection	

459 Data taking conditions are important in the analysis because of the possible biases. In order
 460 to preserve high data quality some events must be rejected. The reason may be unstable beam
 461 conditions, disabled parts of the detector or events with too many noisy cells. Number of runs, than
 462 can be used for the analysis are stored in a so-called Good Run List (GRL), which in the addition to
 463 the run numbers contains information about luminosity blocks.

Table 10.2: Number of W boson candidates in data and signal MC, remaining after each major requirement. The signal MC is normalised to the NNLO cross-section shown in Tab. 13.1

Requirement	Number of candidates			
	Data	signal MC	Data	signal MC
	$W^+ \rightarrow e\nu$ $W^- \rightarrow e\nu$			
No selection	27491466	8354	27491466	5002
Event selection	333054	6044	333054	3139
Lepton selection	15075	4315	15075	2306
Boson selection	3914	3544	2209	1941
	$W^+ \rightarrow \mu\nu$ $W^- \rightarrow \mu\nu$			
No selection	27491466	8354	27491466	5002
Event selection	26475095	8226	26475095	4916
Lepton selection	11466	4782	11466	2595
Boson selection	4365	3936	2460	2164
	$Z \rightarrow ee$ $Z \rightarrow \mu\mu$			
No selection	27491466	1196	27491466	1196
Event selection	333054	1051	333054	1051
Lepton selection	459	430	459	430
Boson selection	430	418	430	418

464 Events, where LAr calorimeter was malfunctioning are excluded by LAr quality criteria. Furthermore
 465 required to have at least one primary vertex from a hard scattering with at least 2 tracks, that are
 466 reconstructed from this vertex.

467 Online selection of events is based on a single lepton trigger, depending on a lepton flavor. For
 468 electron analysis EF_e15_loose1 trigger is used, which records electrons with $E_T > 15$ GeV. This trigger
 469 uses additional "loose" isolation requirements to exclude jets, that are misidentified as electrons. In
 470 the muon channel lowest single lepton trigger is EF_mu10. It records events with muons $E_T > 10$ GeV.

471 10.2 Lepton quality cuts

472 Both analyses use similar selection criteria, applied on a leptons. The leptons must satisfy require-
 473 ment $P_T^l > 20$ GeV and match to the event trigger.

474 Electron candidates are required to be within pseudorapidity range $|\eta^l| < 2.47$. The electron candi-
 475 dates found within the transition region between the barrel and the endcap electromagnetic calorime-
 476 ters, $1.37 < |\eta^l| < 1.52$, are removed. Additionally, for a better multijet background rejection medium
 477 identification and $P_T^{cone,20} < 0.1$ criterias are applied. The object quality (OQ) cut applied in order to
 478 remove events from runs where there dead front end boards in the calorimeter.

479 Muons have to satisfy the following criteria: they should be reconstructed by a staco algorithm in
 480 a muon spectrometer and fall within range $|\eta^l| < 2.5$. Set of medium requirements is applied. They
 481 must also satisfy $P_T^{cone,20} < 0.1$ isolation criteria.

482 10.3 Boson selection

483 The events, containing W boson candidates are required to have exactly one lepton, fulfilling the
484 lepton selection. Missing transverse energy, used as a proxy for a neutrino from W decay is required
485 to be $E_T^{miss} > 25\text{GeV}$. The transverse mass, calculated from the lepton and missing transverse energy
486 as in Eq. 3.5 has to be bigger than 40 GeV ($M_T^W > 40 \text{ GeV}$).

487 The reconstructed lepton pair in case of Z boson analysis is required to have the invariant mass
488 between 66 and 116 GeV. Both upper and bottom limits allow to exclude regions with high background
489 contamination.

490 The full set of cuts is summarized in a Tab. 10.1.

491 10.4 Cut flow

492 The effect of each selection can be studied using cut-flows, which show the number of events
493 passing each set of cuts in a sequential order. Cut flows for W and Z analysis are shown in a Tab.
494 10.2.

495

Chapter 11

Monte Carlo corrections

497 Monte Carlo plays important role in the cross-section measurement. It is constantly being improved,
 498 in order to obtain a better precision in data description. Part of these corrections have been described
 499 in Chap. 7. Unfortunately, not everything can be taken into account during simulation itself. This
 500 leads to differences between data and Monte Carlo, that need to be accounted for. There are two
 501 possible methods to correct Monte Carlo without regenerating it. First one is to apply event weights,
 502 so that each MC event can contribute by a non one entry to a histogram. This procedure called
 503 event reweighting. Second one is MC smearing. It uses random numbers to alter the reconstructed
 504 4-vectors. This chapter describes all additional corrections, that have been applied on MC samples in
 505 this analysis. All of these correction are introducing additional systematic error, that will be discussed
 506 in the Chap. 15.

507 11.1 Lepton efficiency corrections

508 The efficiency of lepton detection at ATLAS detector can be divided into three components:

- 509 • The reconstruction efficiency ϵ_{rec} is a probability to reconstruct lepton as a lepton of this
 510 flavor.
- 511 • The identification efficiency $\epsilon_{id|rec}$ is the probability that a reconstructed lepton survives iden-
 512 tification requirements.
- 513 • The trigger efficiency $\epsilon_{trig|rec,id}$ is the probability, that lepton satisfy trigger requirements.

The full efficiency for a single lepton can be written as:

$$\epsilon_{total} = \epsilon_{rec} \times \epsilon_{id|rec} \times \epsilon_{trig|rec,id} \quad (11.1)$$

514 All these efficiencies are measured using tag-and-probe method in $Z \rightarrow ll$ decays. One of the
 515 leptons from Z boson, called "probe", is initially selected with all of the cuts, except the one under
 516 study. Second one, called "probe", satisfies more tighter selection with some additional cut, e.g.
 517 trigger matching.

518 The reconstruction efficiency is associated with the algorithm used in the event reconstruction
 519 process. This is causing differences between electrons and muons efficiencies. In the electron case
 520 the reconstruction efficiency is depicted as a probability to reconstruct an electron which has de-
 521 posited its energy in electromagnetic calorimeter cluster as an electron candidate.

Muon reconstruction efficiency is given by:

$$\epsilon_{reco,muon} = \epsilon_{reco,muon|ID} \cdot \epsilon_{ID} \approx \epsilon_{reco,muon|ID} \cdot \epsilon_{ID|MS}, \quad (11.2)$$

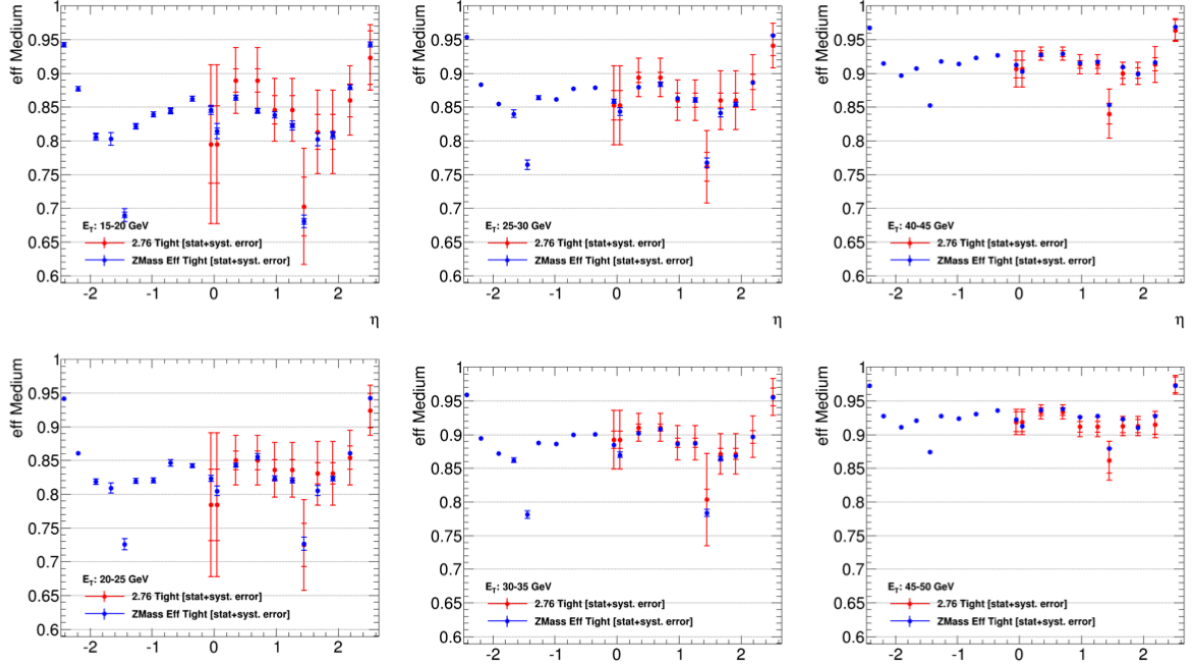


Fig. 11.1: Comparison of electron efficiencies as calculated for 8TeV (blue points) and 2.76TeV (red points) for MC simulation. Efficiencies are shown as a function of pseudorapidity (η) for different electron E_T bins. Both statistical and systematic uncertainties are shown.

522 where $\epsilon_{reco,muon|ID}$ is a conditional probability that muon reconstructed in ID is also reconstructed
 523 using MS as a combined muon, and ϵ_{ID} is a probability that muon is reconstructed as an ID track. This
 524 quantity ϵ_{ID} cannot be measured directly in a data and therefore is replaced by $\epsilon_{ID|MS}$ - probability
 525 that muon reconstructed in MS is also reconstructed in ID, that can be measured by the tag-and-
 526 probe method.

Simulation samples are corrected to match data efficiencies by a scale-factor :

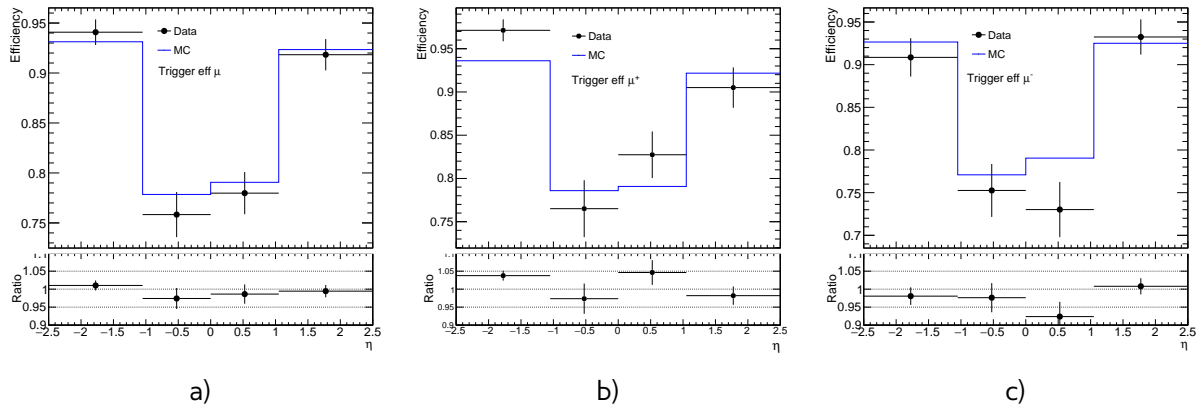
$$SF_{reco,id,trig} = \frac{\epsilon_{reco,id,trig}^{data}}{\epsilon_{reco,id,trig}^{MC}} \quad (11.3)$$

527 The scale factors are calculated in a P_T^l and η^l bins and have associated statistical and systematic
 528 uncertainty components. The statistical component is connected to a size of $Z \rightarrow ll$, which is in
 529 our case is around 500 event per each lepton flavor. This makes statistical error the dominant one
 530 and means that precise calculation of scaling factors based on this data is difficult.

531 It is possible however to use scale factors for 8 TeV 2012 data. The main difference between these
 532 data samples are center of mass energy and the pile-up conditions (10 in 2012 and less than 1 in 2013).
 533 This effects have been studied on a $Z \rightarrow ee$ sample. Fig. 11.1 shows the scale factors for different
 534 P_T^l ranges as a function of η^l . The differences in the scale factors are negligible and fully covered
 535 by the statistical errors. This justifies the usage of 8 TeV scaling factors with increased uncertainty
 536 (that is considered to be fully statistical) in the analysis at 2.76 TeV.

Table 11.1: Muon trigger scale factors

	SF	SF stat.error
μ	0.988	0.011
μ^+	1.012	0.015
μ^-	0.964	0.015


 Fig. 11.2: Trigger scale efficiencies distribution for a) μ b) μ^+ c) μ^- as a function of pseudorapidity

11.1.1 Muon Trigger SF

Unfortunately, single muon trigger haven't been present in the 2012 data, so muon trigger scale factor had to be derived from the 2.76 TeV data. The size of the Z sample is not big enough to make the scale factors in P_T^l and η^l bins.

Since the P_T^μ cut is significantly higher, than the trigger threshold, efficiency P_T^μ dependency can be considered flat. On the another hand, η dependence are expected. Binning in η is motivated by a detector construction. Muon trajectory is bend in a magnetic field. That can lead to small differences in a trigger efficiencies for different muon charges. Possible charge dependency of the scale factors have been also studied.

Trigger efficiencies for data and MC in η bins are shown in a Fig. 11.2. Total scale factors are presented in Tab. 11.1. Scale factors for μ^+ and μ^- are more than 3σ away from each other, that is a clear indicator of a charge dependency.

Effect of applying different scale factors on muon for W analysis is shown on Fig. 11.3 - 11.5. Best agreement with data is achieved by applying single bin scale factor. This motivates a choice of single bin charge dependent scale factor for this analysis.

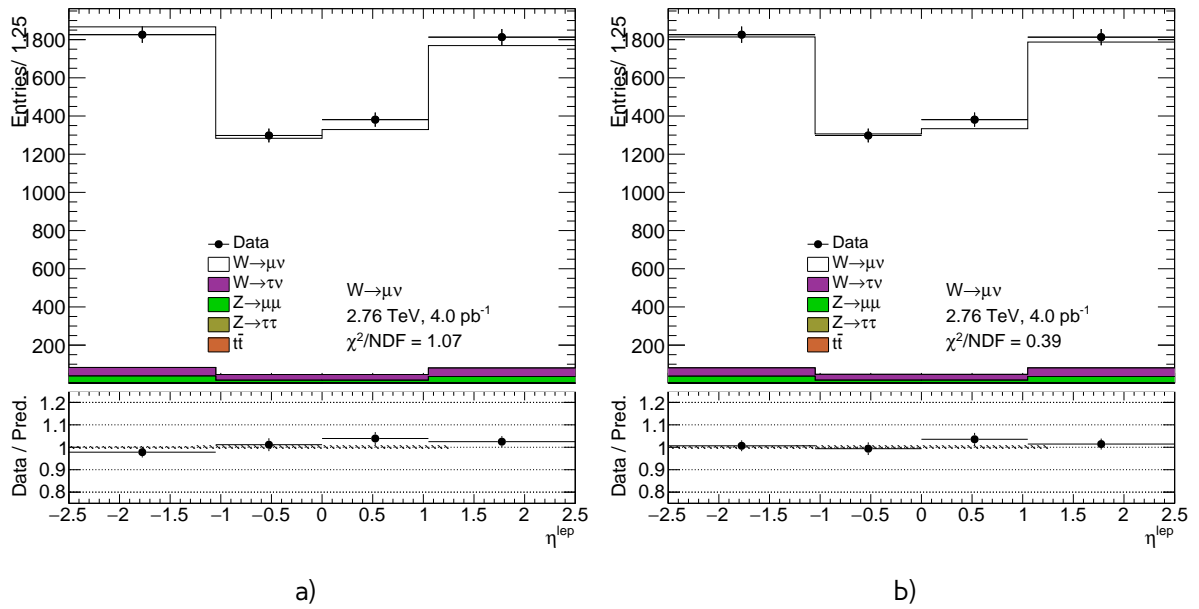


Fig. 11.3: Muon pseudorapidity distribution from the $W \rightarrow \mu\nu$ selection with a) binned b) not binned charge dependent trigger scale factor applied

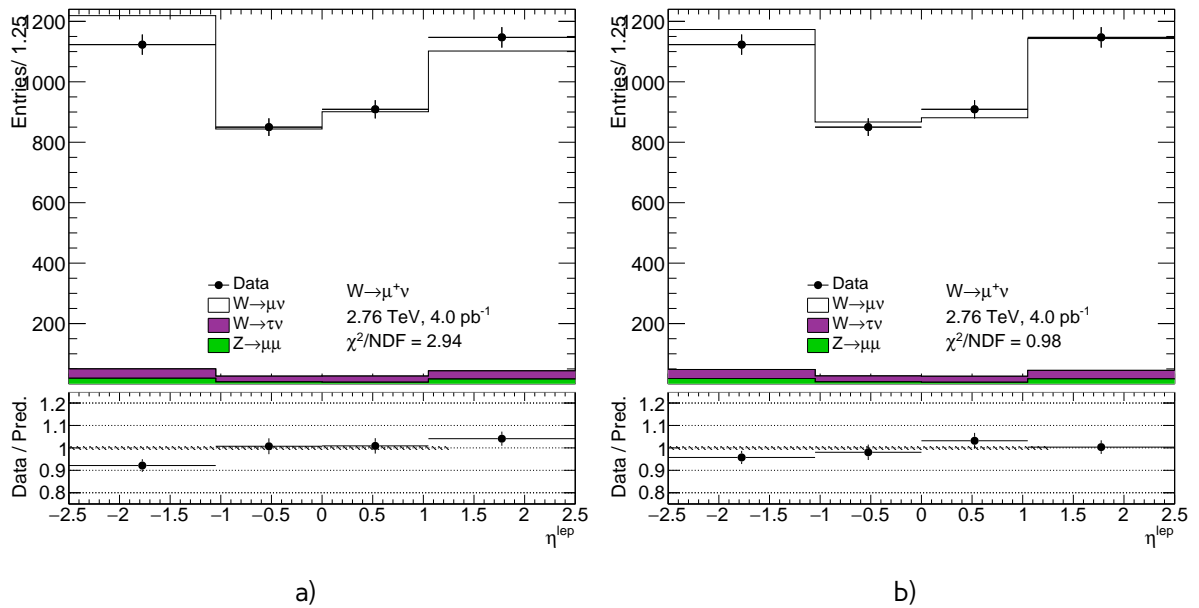


Fig. 11.4: Muon pseudorapidity distribution from the $W \rightarrow \mu^+\nu$ selection with a) binned b) not binned charge dependent trigger scale factor applied

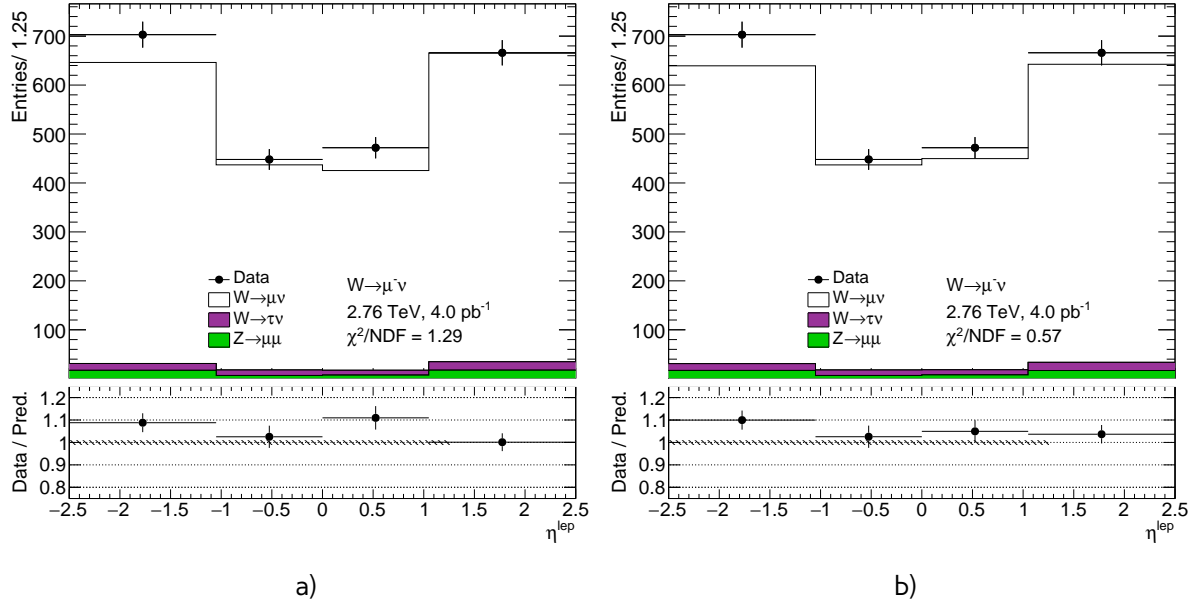


Fig. 11.5: Muon pseudorapidity distribution from the $W \rightarrow \mu^- \nu$ selection with a) binned b) not binned charge dependent trigger scale factor applied

11.2 Electron energy scale and resolution

The reconstructed electron clusters energy tend to be shifted in comparison to the true energy of the initial electron. The correction of this shift is done in both data and MC as a 3 step procedure:

- Electronic calibration, that transfers a raw signal from a readout to a cluster energy deposit.
- MC based calibration. It corrects the effects of the energy loss in the material in front of the calorimeter and the leakage into the hadronic calorimeter. This calibration is applied on both data and MC.
- Correction of the calorimeter cell response in the data. This allows to get the right response in non-optimal HV-regions and to exclude biases in the calorimeter electronics reconstruction.

The energy shift is parameterised, as:

$$E^{data} = E^{MC}(1 + \alpha_i), \quad (11.4)$$

where E^{data} and E^{MC} are the energies in data and simulation, respectively and α_i is a mean shift in a given bin i in η . The effect of this miscalibration on a reconstructed mass of Z boson neglecting second order terms is:

$$m_{i,j}^{data} = m_{i,j}^{MC}(1 + \alpha_{i,j}), \quad \alpha_{i,j} \sim \frac{\alpha_i + \alpha_j}{2}, \quad (11.5)$$

where $m_{i,j}^{data}$ and $m_{i,j}^{MC}$ are reconstructed mass of Z boson in a i and j bins in η for data and MC respectively.

It is also needed to correct the difference in the electron resolution. It can be described by Eq. 8.1. It is assumed, that sampling and noise terms are well modeled by MC and the main difference is

coming from a constant term. So, the electron resolution correction can be written as:

$$\frac{\sigma_E}{E}^{Data} = \frac{\sigma_E}{E}^{MC} \oplus c_i \quad (11.6)$$

where c_i is an η dependent relative resolution correction. Similarly to an energy scale correction it is possible to derive resolution correction factor by a comparison of $m_{i,j}^{data}$ and $m_{i,j}^{MC}$ distributions. α_i and c_i correction values are obtained via the χ^2 fit on a invariant mass electrons for data and MC. The resulting energy scale is applied on a data, while the resolution is corrected in MC. The resulting scale is validated using a $J/\psi \rightarrow ee$ and $Z \rightarrow ee\gamma$ samples.

11.3 Muon momentum correction

The muon momentum resolution depends on a η , ϕ and p_T of the muon [?]. There is an empirical formula to describe it inside the detector (ID or MS):

$$\frac{\sigma_{Det}(p_T)}{p_T} = \frac{r_0^{Det}(\eta, \phi)}{p_T} \oplus r_1^{Det}(\eta, \phi) \oplus r_2^{Det}(\eta, \phi) \cdot p_T. \quad (11.7)$$

The first term origins from the fluctuations of the energy loss in the transversed material. The second term is coming from the magnetic field inhomogenities and the local displacements. Third term describes the intrinsic resolution effects.

Similarly to electrons, the overall energy scale shift between data and MC is parameterised as:

$$p_T^{data} = p_T^{MC} + s_0^{Det}(\eta, \phi) + s_1^{Det}(\eta, \phi) \cdot p_T^{MC}, \quad (11.8)$$

where $s_0^{Det}(\eta, \phi)$ is coming from the imperfect knowledge of energy losses for muons passing through detector.

This leads to a total correction formula:

$$p_T^{Cor,Det} = \frac{p_T^{MC,Det} + \sum_{n=0}^1 s_n^{Det}(\eta, \phi) (p_T^{MC,Det})^n}{1 + \sum_{m=0}^2 \Delta r_m^{Det}(\eta, \phi) (p_T^{MC,Det})^{m-1} g_m}, \quad (11.9)$$

where g_m are normally distributed random variables with mean 0 and width 1. Due to small amount of material between interaction point and the ID, $\Delta r_0^{ID}(\eta, \phi)$ and $s_0^{ID}(\eta, \phi)$ are set to 0. Missalignment effect of the MS is corrected on a simulation level by adding a random smearing to the alignment constants. This allows to set $\Delta r_2^{MS}(\eta, \phi)$ to 0 during a fit.

The correction factors are extracted using events with $Z \rightarrow \mu\mu$ candidates fulfilling the requirement of two combined muons. For the correction invariant mass distributions $m_{\mu\mu}^ID$ and $m_{\mu\mu}^{MS}$ are considered individually within a specific $\eta - \phi$ region of fit. Combined muon parameters are used to obtain angles η and ϕ . The correction extraction is performed first for the ID and then for the MS with addition of the fit variable:

$$\rho = \frac{p_T^{MS} - p_T^{ID}}{p_T^{ID}}, \quad (11.10)$$

which represents the p_T imbalance between ID and MS.

In a second step corrections are propagated to the combined momentum, using a weight average:

$$p_T^{Cor,CB} = f \cdot p_T^{Cor, ID} + (1 - f) \cdot p_T^{Cor, MS}, \quad (11.11)$$

579 where the weight f is derived from the MC.

580 Chapter **12**

581 **Hadronic recoil calibration**

583	12.1 Introduction	59
584	12.2 Hadronic recoil resolution correction	61
585	12.2.1 Event activity correction	62
586	12.2.2 Resolution corrections using Z events	67
587	12.3 Hadronic recoil bias correction	69
588	12.3.1 Bias determination from M_T^W distribution	69
589	12.3.2 Bias determination using u_{\parallel} distribution	70
590	12.3.3 Systematic uncertainty estimation	72
591	12.4 Summary on hadronic recoil systematics	73
592		
593		
594		
595		

596 E_T^{miss} affects significantly the W boson measurement, so it is important to have a solid understand-
597 ing of possible sources differences in the hadron recoil reconstruction in data and Monte Carlo.
598 This chapter describes the procedure of calibration bias and resolution mismodelling in a hadron
599 recoil, that was adapted for 2.76 TeV data.

600 **12.1 Introduction**

601 This analysis uses a standard hadronic recoil calibration procedure, described in [?], that was modified
602 and adapted for the low statistics 2.76 TeV case. The standard procedure consists of the 3 main steps.

603 The first step in a hadronic recoil calibration procedure aims to correct differences in a pile-up
604 modeling in the event. Additional interactions can have a significant effect on E_T^{miss} and $\sum E_T$
605 distributions. These discrepancies are usually corrected by reweighting average number of interactions
606 per bunch crossing in MC to match the data. However, ATLAS simulation is suited for high pile-
607 up runs, so this quantity is modelled discretely in case of 2.76 TeV analysis (Fig. 12.1), what makes
608 the precise reweighting impossible. However, since the mean number is below 1, effect of these
609 discrepancies on E_T^{miss} distributions can be neglected.

610 On the second and third step possible discrepancies in a resolution and scale of hadronic recoil
611 respectively are corrected. The hadronic recoil algorithm performance can be studied in MC through
612 the projection of $\vec{H}R$ on the direction of the transverse momentum of the vector boson, as shown in
613 Fig. 12.2. This projection can be divided into perpendicular u_{\perp} and parallel u_{\parallel} components as follows:

$$u_{\parallel} = \vec{v}_{xy} \cdot \vec{H}R \quad (12.1)$$

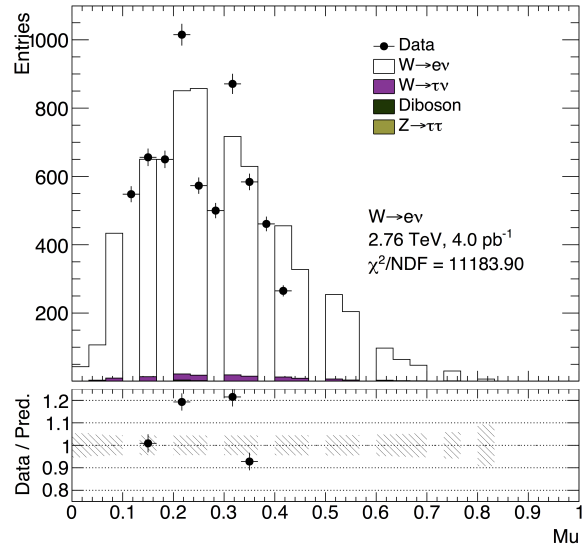


Fig. 12.1: Mean number of interactions per bunch crossing from the $W \rightarrow e\nu$ selection. MC modelled pileup discretely, that makes a standard data to MC reweighting procedure not feasible.

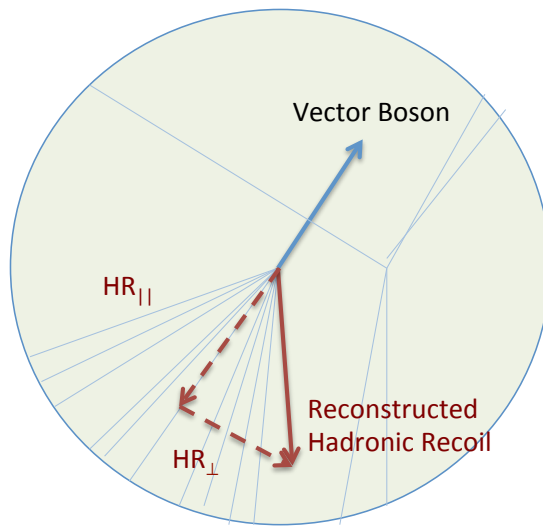


Fig. 12.2: Parallel and perpendicular projections of the hadronic recoil with respect to the transverse momentum of the vector boson [?]

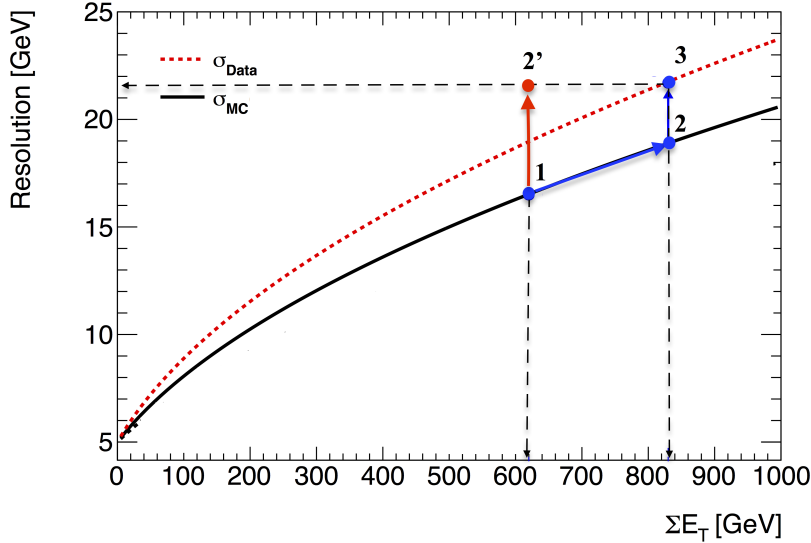


Fig. 12.3: Schematic view of the correction procedure: this figure illustrates the resolution of u_{\perp} as a function of $\sum E_T$. The dotted curve represents data resolution (σ_{data}), solid black is a nominal MC (σ_{MC}). Blue line from point 1 to point 2 corresponds to a $\sum E_T$ correction discussed in Sec.12.2.1. Red line from point 1 to point 2' corresponds to a direct correction of resolution mismodelling discussed in Sec. 12.2.2. Modified from [?]

$$u_{\perp} = v_x \cdot HR_y - v_y \cdot HR_x, \quad (12.2)$$

where \vec{v}_{xy} is a unitary vector along the transverse component of a vector boson momentum and v_x and v_y are its projections on x and y axis respectively. In the case of the true kinematics $u_{\parallel} = p_T^{bos}$ and $u_{\perp} = 0$. However the calorimeter resolution is causing relatively wide distributions for these projections. The parallel component u_{\parallel} is sensitive to a possible bias in the hadron recoil, while the perpendicular u_{\perp} can be used for determination of the resolution discrepancies. The mean and the width of these distributions can depend on different variables, such as a mean number of interactions in event, hadronic activity, boson P_T^{bos} etc.

It is convenient to use Z boson decays for a hadron recoil calibration, since its transverse momentum P_T^Z can be determined not only from the hadronic recoil, but also from its decay products. The P_T^Z resolution coming from a lepton reconstruction is 3-4 times more precise, than the one extracted from a hadronic recoil. This allows to treat leptonically reconstructed P_T^Z as a reference P_T of the boson and to compare directly u_{\perp} and u_{\parallel} in data and MC. However, small size of the Z sample in 2.76TeV data leads to a high statistics error for these distributions. The calibration constants can also be derived from W boson decays. In order to exclude possible bias from P_T^W mismodelling these calibration constants can be derived through data vs MC comparison of P_T^W independent distributions (such as M_T^W). The combined Z and W boson determination procedure has been used.

12.2 Hadronic recoil resolution correction

The event activity plays an important role in the E_T^{miss} reconstruction. Since $\sum E_T$ and the hadronic recoil resolution values are correlated, the possible mismodelling of the event activity can lead to

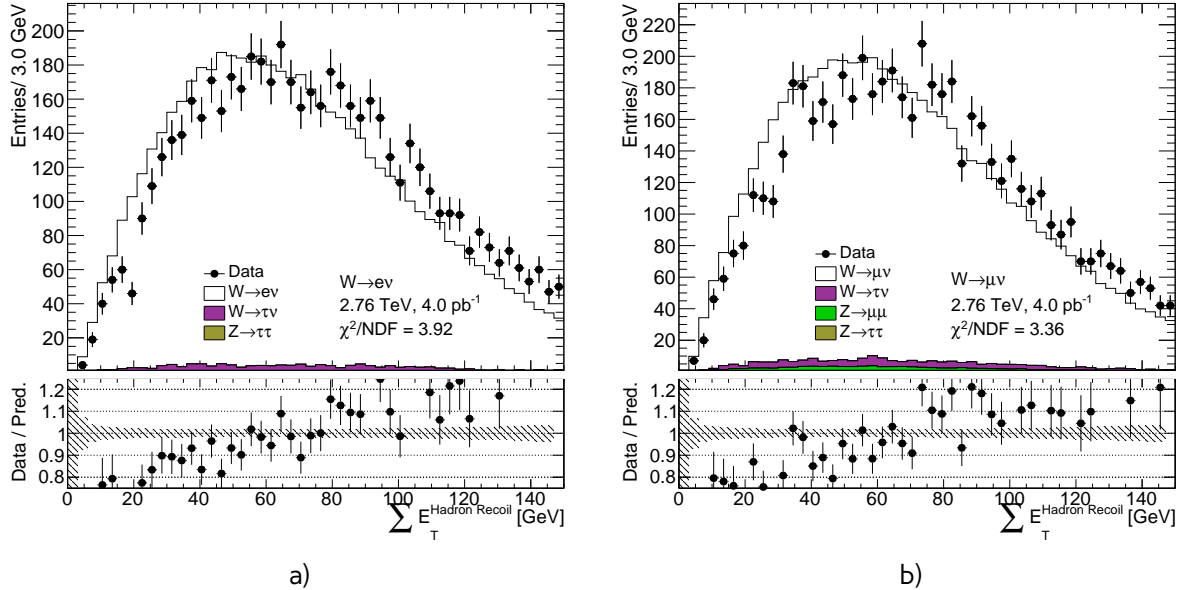


Fig. 12.4: Event activity $\sum E_T$ distribution from a) the $W \rightarrow e\nu$ selection and b) the $W \rightarrow \mu\nu$ selection. There is a clear sign of the event activity mismodelling in both channels, that should be corrected.

629 differences between the data and Monte Carlo E_T^{miss} resolutions (Fig. 12.3). There are two ways of
 630 resolution correction in the 2.76 TeV data:

- 631 • As a two step procedure, shown as path 1-2-3 in Fig. 12.3. The first step is to correct sumet dis-
 632 tribution to match the data using reweighting of the events. Remaining differences in resolution
 633 are corrected at the second step. This method is discussed Sec. 12.2.1.
- 634 • The second order effects on E_T^{miss} coming from $\sum E_T$ modelling are neglected and the resolution
 635 differences between data and MC corrected directly. This procedure matched to the path 1-2'
 636 in Fig. 12.3 and described in Sec. 12.2.2.

637 12.2.1 Event activity correction

638 The distributions of the event activity $\sum E_T$ are shown in a Fig. 12.4. There is a visible shift between
 639 data and MC distribution for both W boson channels. Standard procedure, used in M_T^W measurment
 640 at 7 TeV uses a smirnov transformation of $\sum E_T$ distributions in Z events. Unfortunately, size of the
 641 Z sample is not sufficient for this procedure (Fig. 12.5). This motivates a choise of $\sum E_T$ reweighting
 642 constants determination from the W boson sample.

The event activity $\sum E_T$ is correlated to the truth transverse momentum of the boson, as shown
 in Fig. 12.6, so in order to avoid possible bias from changing P_T^W spectrum, reweighting constants
 are derived in bins of reconstructed boson momentum $P_T^{W,rec}$. Inside each $P_T^{W,rec}$ bin reweighting
 constants are calculated as:

$$SF_{channel} = \frac{\sum E_T^{data,selection}}{\sum E_T^{MC,no\ cuts}}, \quad (12.3)$$

643 where $\sum E_T^{data,selection}$ is a $\sum E_T$ distribution inside a given $P_T^{W,rec}$ after the full event selection. In order
 644 to reduce systematic error from this value, a combination of $W \rightarrow e\nu$ and $W \rightarrow \mu\nu$ events is

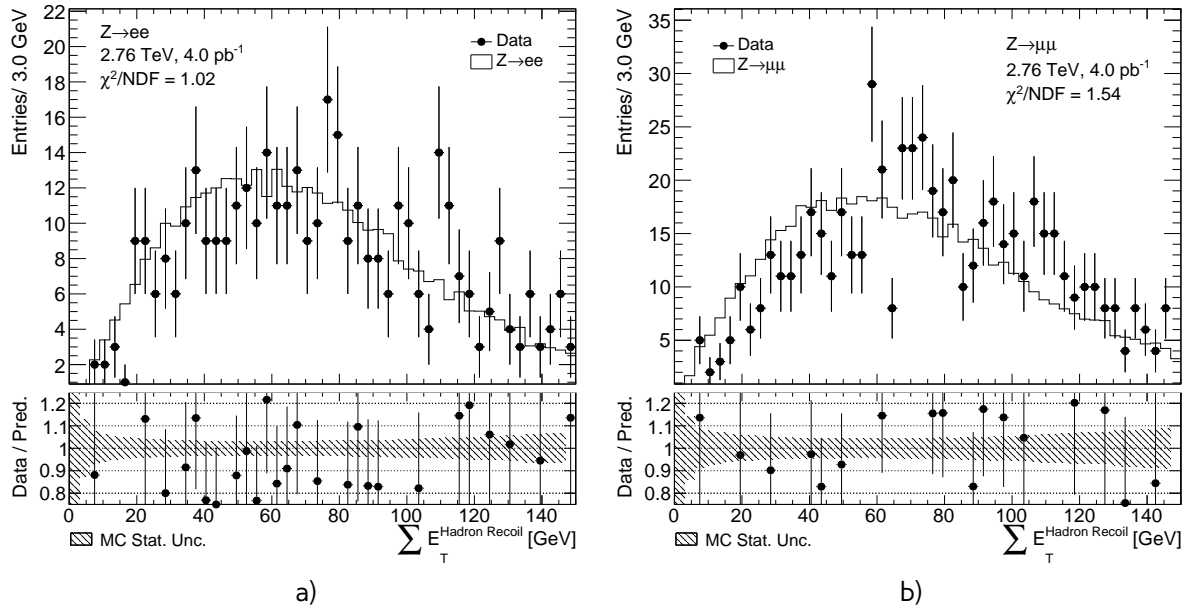


Fig. 12.5: Event activity $\sum E_T$ distribution from a) the $Z \rightarrow ee$ selection and b) the $Z \rightarrow \mu\mu$ selection. Size of the Z sample in 2.76 TeV data is insufficient indicate to the mismodelling of the event activity.

645 used. Second term $\sum E_T^{MC, no\ cuts}$ is $\sum E_T$ distribution in MC before any selection. Scale factors are
 646 determined separately for each signal MC for W boson decays, in order to leave the total number of
 647 events in MC after correction untouched. Transverse boson momentum binning is chosen so what
 648 there is an approximate equality in total number of events between bins. The total number of $P_T^{W, rec}$
 649 bins is 6. Example of correction factors for two different $P_T^{W, rec}$ bins are shown on a Fig.12.7. Resulting
 650 reweighting constants for $W \rightarrow e\nu$ and $W \rightarrow \mu\nu$ MC samples are shown in Fig. 12.8. This method
 651 allows to leave the reconstructed transverse momentum of the boson untouched and introduces a
 652 small change in a truth boson spectrum, as shown on Fig. 12.10.

653 Systematic error estimation

654 Systematic error on this reweighting can be estimated using the approximation of the ration inside
 655 each $P_T^{W, rec}$ bin by a polynomial degree 2 or 1. This method also allows to neglect effect of the data
 656 fluctuations, especially for high $\sum E_T$ regions, that could be seen on a Fig. 12.8. Because of the low
 657 statistics for $\sum E_T > 220$ GeV ratio in the last bins have been set to 1 and this region haven't been
 658 included in the polynomial fit. Total reweighting constants obtained from this procedure are shown
 659 on a Fig. 12.11.

660 Statistical error estimation

Statistical error on the $\sum E_T$ reweighting is estimated using Toy MC method, described in Chap.15
 from the polynomial order 2 approximation. The fitted parameters of the polynomials are varied
 inside each $p_T^{W, rec}$ bin within their fit uncertainties as in Eq. 15.2. Because of the possible correlations
 between fitted parameters, the multivariate Gaussian distribution have been used, that is calculated

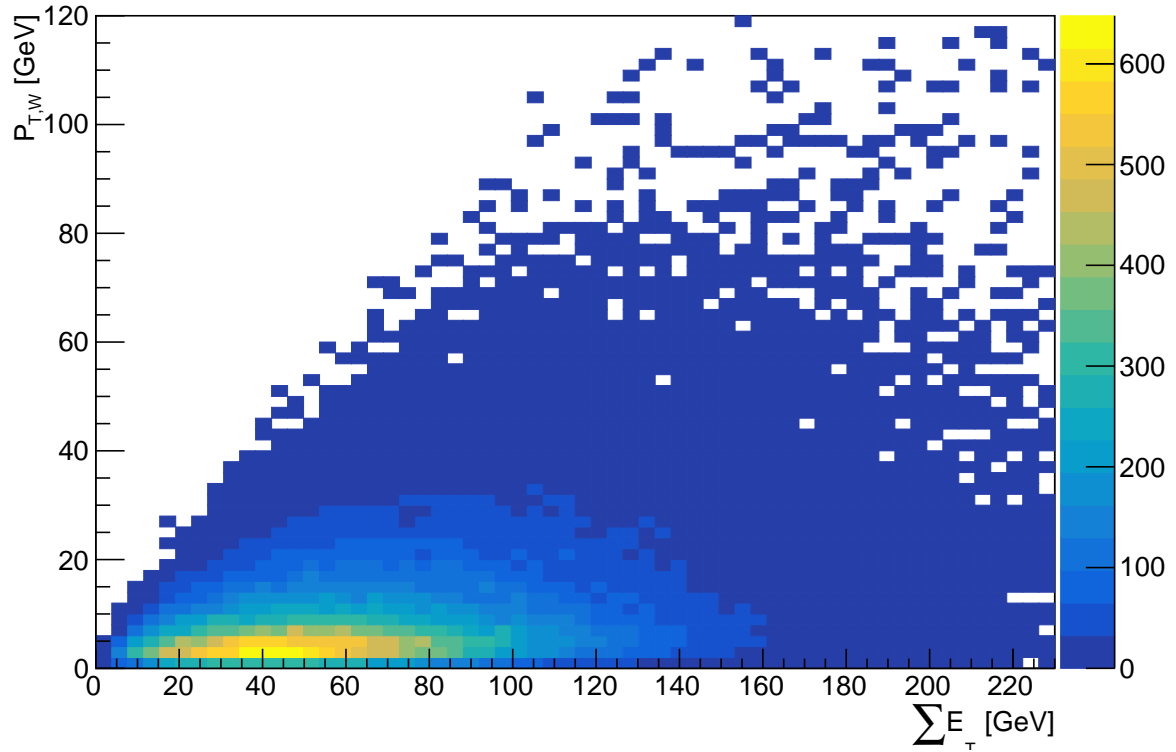


Fig. 12.6: Distribution of event activity $\sum E_T$ vs truth transverse momentum of the W boson P_T^W *truth* in the $W^+ \rightarrow e\nu$ MC sample.

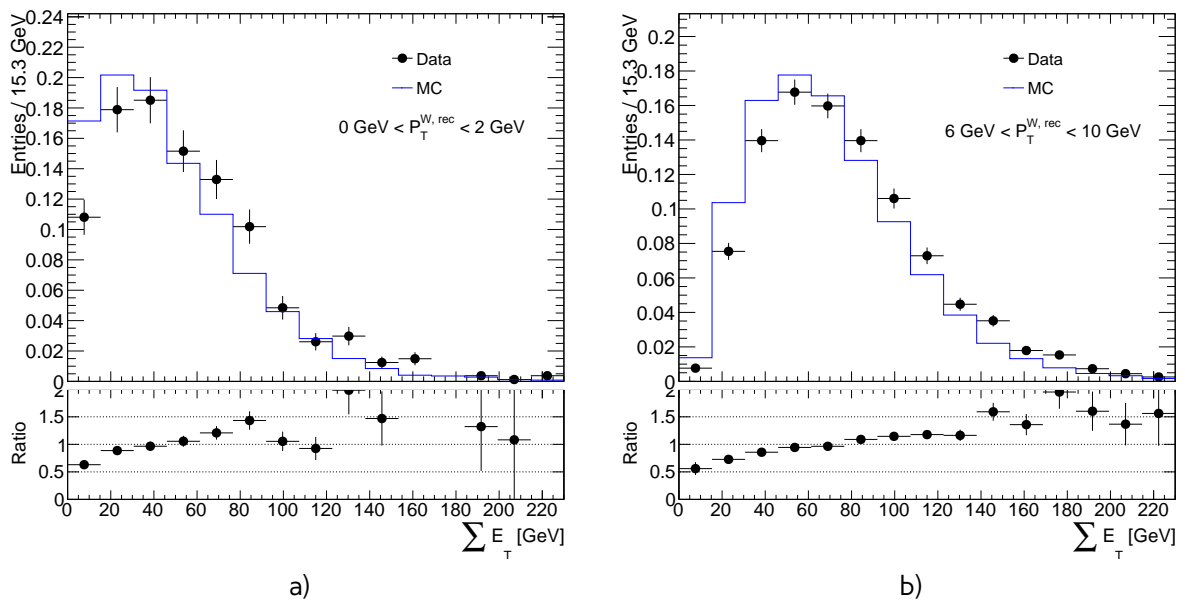


Fig. 12.7: Distribution of $\sum E_T$ for the different $p_T^{W,rec}$ bins for $W^+ \rightarrow e\nu$ MC sample

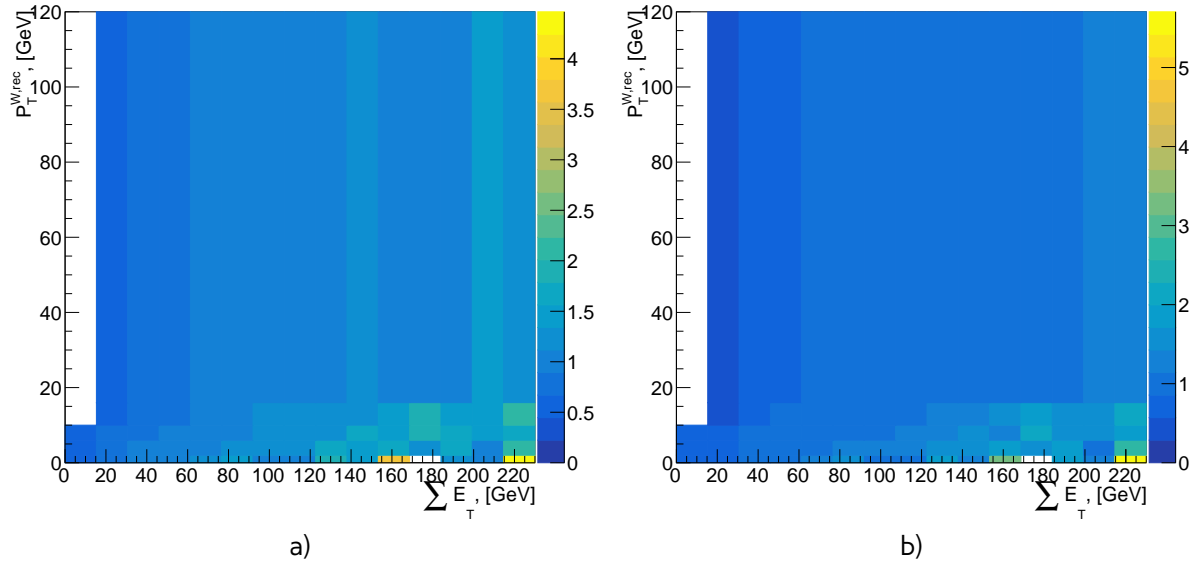


Fig. 12.8: Distribution of $\sum E_T$ reweighting constants derived for a) $W^+ \rightarrow e\nu$ and b) $W^+ \rightarrow \mu\nu$ MC sample.

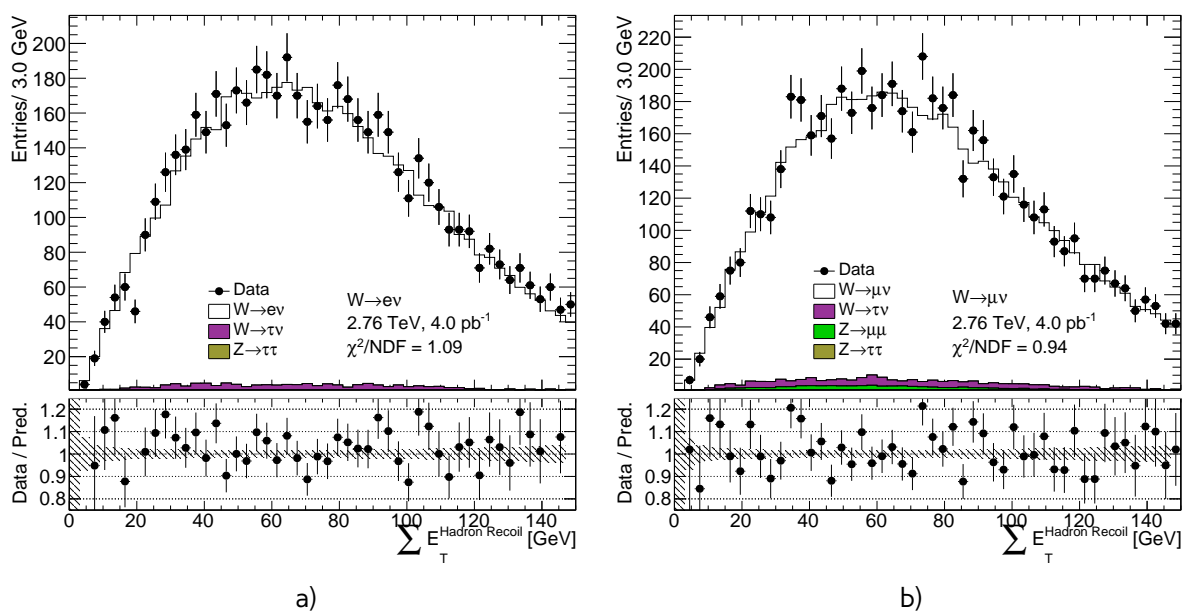


Fig. 12.9: Event activity $\sum E_T$ distribution from a) the $W \rightarrow e\nu$ selection and b) the $W \rightarrow \mu\nu$ selection after $\sum E_T$ correction.

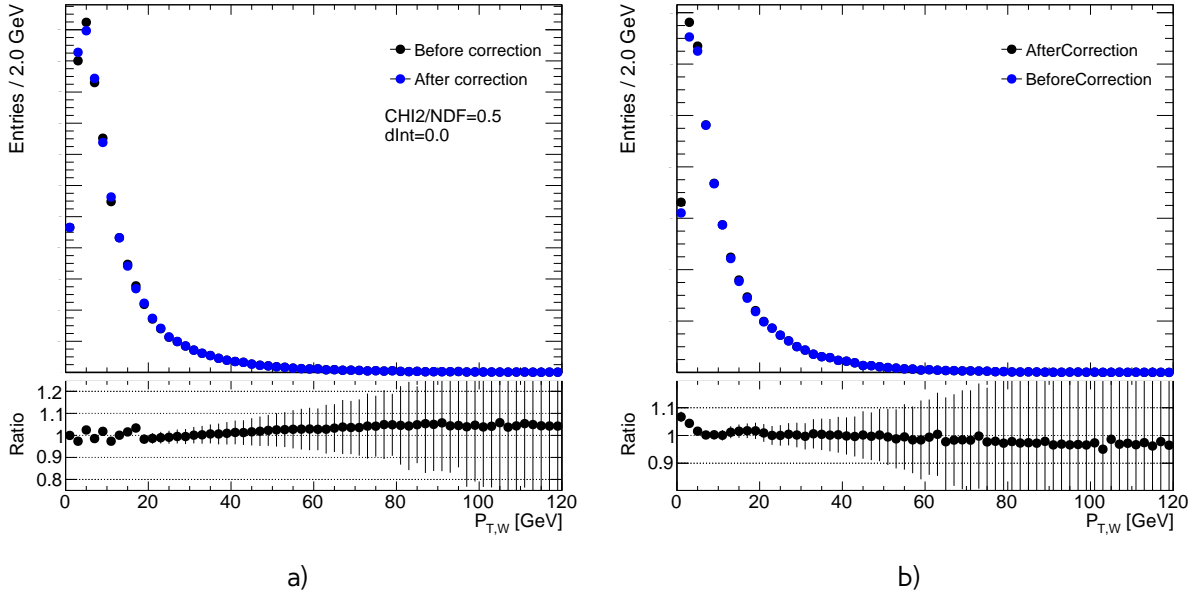


Fig. 12.10: Effect of the $\sum E_T$ reweighting on a) reconstructed transverse momentum of the boson and b) truth transverse momentum of the boson in $W^+ \rightarrow e\nu$ MC sample.

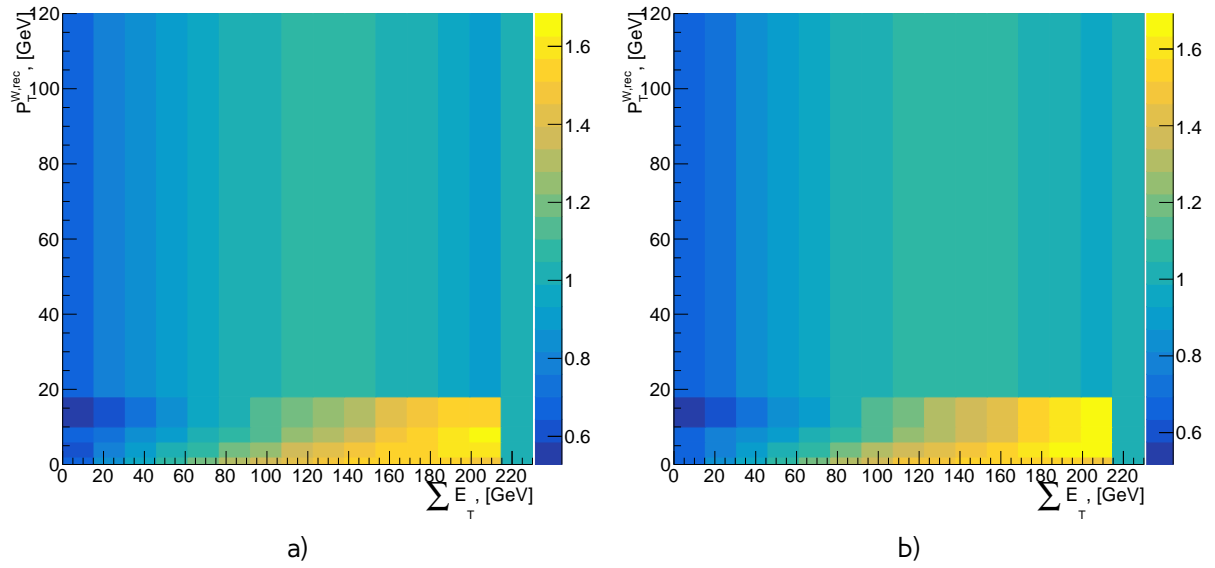


Fig. 12.11: Distribution of $\sum E_T$ reweighting constants derived for a) $W^+ \rightarrow e\nu$ and b) $W^+ \rightarrow \mu\nu$ MC sample using polynomial order 2 approximation.

Table 12.1: Effect of $\sum E_T$ correction on a C_W for a different channels and methods

Channel	δC_W no approximation	δC_W polynomial order 2	δC_W polynomial order 1	δC_W Toy MC
$W^+ \rightarrow e^+ \nu$		0.39%	0.31%	0.03%
$W^- \rightarrow e^- \nu$		0.33%	0.22%	0.03%
$W^+ \rightarrow \mu^+ \nu$		-0.20%	-0.28%	0.03%
$W^- \rightarrow \mu^- \nu$		-0.21%	-0.27%	0.03%

as:

$$p(x; \mu, \Sigma) = \frac{1}{(2\pi)^{n/2} |\Sigma|^{1/2}} \exp\left(-\frac{1}{2}(x - \mu)^T \Sigma^{-1} (x - \mu)\right), \quad (12.4)$$

where $\mu \in \mathbf{R}^n$ are the obtained from the fit parameters and Σ is $n \times n$ covariance matrix of these parameters. In case of the polynomial order two $n=3$. For statistic error determination total number of 25 toys have been used. Total error is calculated using Eq.15.3.

Effect of the $\sum E_T$ correction on cross-section

Overall effect of the $\sum E_T$ correction for different methods is summarised in Tab. 12.1. Statistical error, estimated using Toy MC method is negligible. Sign of the effect differs for different W channels, that cannot be explained by a systematic error coming from the method. This effect also cannot be explained from a physical point of view, so it was decided not to use this corrections in a final analysis.

12.2.2 Resolution corrections using Z events

Another way to check resolution effects is to study u_\perp and $u_\parallel - p_T^Z$ distributions in events containing Z boson. This correction assumes, that any resolution mismodelling reflects discrepancies in the $\sum E_T$ distribution, while the difference in the resolution at a given $\sum E_T$ is subleading. There is a clear difference in an RMS of these distributions between data and MC, that cannot be accounted for a statistical uncertainties in the data (Fig. 12.12 and Fig. 12.13). The difference in resolutions is consistent for u_\perp and $u_\parallel - p_T^Z$ distributions, but depends on an analysis channel and isolation + identification criteria.

The resolution is corrected by smearing with a Gaussian distribution each component of a hadronic recoil:

$$u'_\parallel = u_\parallel + \text{Gaus}(0, d\sigma) \quad (12.5)$$

$$u'_\perp = u_\perp + \text{Gaus}(0, d\sigma), \quad (12.6)$$

where $d\sigma$ is a difference in a resoultions calculated as:

$$d\sigma = \sqrt{\sigma_{data}^2 - \sigma_{MC}^2} \quad (12.7)$$

Systematic error of this $d\sigma$ is taken as an statistical error for σ_{data} . Due to a random nature of this correction, effect is not stable for a small $d\sigma$. Systematic error have been estimated by repeating

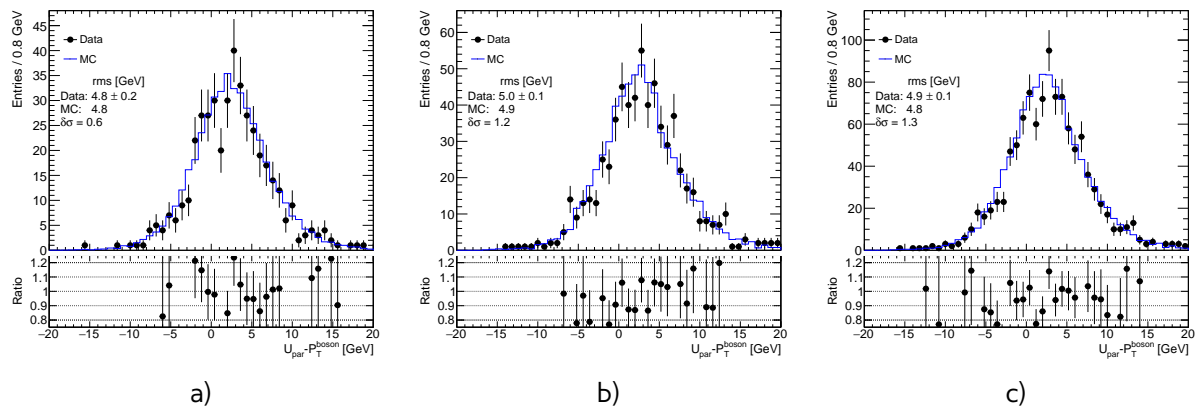


Fig. 12.12: Parallel hadronic recoil component distribution from a) the $Z \rightarrow ee$ selection b) $Z \rightarrow \mu\mu$ selection and c) $Z \rightarrow ll$ selection. The expected contribution from signal is estimated with Monte Carlo simulation, other background sources are considered negligible.

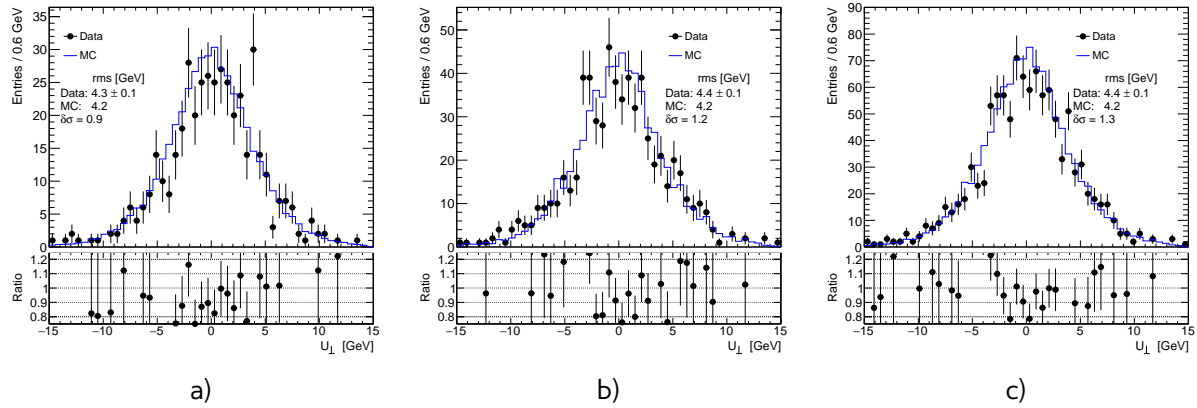


Fig. 12.13: Perpendicular hadronic recoil component distribution from a) the $Z \rightarrow ee$ selection b) $Z \rightarrow \mu\mu$ selection and c) $Z \rightarrow ll$ selection. The expected contribution from signal is estimated with Monte Carlo simulation, other background sources are considered negligible.

Table 12.2: Effect of smearing correction on a C_W for a different channels

Channel	δC_W	error
$W^+ \rightarrow e^+ \nu$	-0.20%	0.04%
$W^- \rightarrow e^- \nu$	-0.11%	0.06%
$W^+ \rightarrow \mu^+ \nu$	-0.16%	0.04%
$W^- \rightarrow \mu^- \nu$	-0.12%	0.07%

682 correction on the same sample 40 times. Overall systematic effect is below 0.2% for each channel
683 (Tab. 12.2).

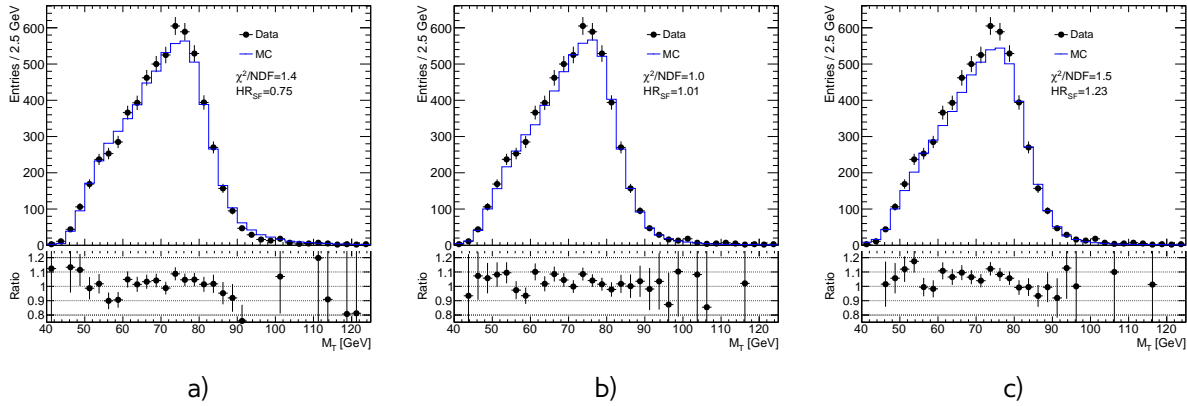


Fig. 12.14: Mass transverse distribution from the $W \rightarrow ev$ selection for different hadronic recoil scales: a) $HR_{SF}=0.75$ b) $HR_{SF}=1.1$ c) $HR_{SF}=1.23$. The expected contributions from signals and backgrounds are estimated with Monte Carlo simulation, except for a QCD background, that is not included.

684 12.3 Hadronic recoil bias correction

As it was mentioned before, it is possible to use both Z and W boson samples for the hadronic recoil bias determination. Correction factor HR_{SF} is applied as:

$$u_{\parallel}^{MC,cor} = u_{\parallel}^{MC} \cdot HR_{SF} \quad (12.8)$$

and can be obtained by scanning the impact of the scaling factor on the data to MC agreement of the distributions that are dominated by the recoil scale uncertainties. The best correction factor and its error is obtained from the fit of χ^2 distributions with the function:

$$\chi^2 = \frac{(HR_{SF} - sf_{best})^2}{\sigma_{sf}^2} + \chi_0^2, \quad (12.9)$$

685 where sf_{best} is the best scale factor, σ_{sf} is a statistical error of this parameter and χ_0^2 is a value of
686 χ^2 in a minimum.

687 This procedure can be used in both Z and W boson samples.

688 12.3.1 Bias determination from M_T^W distribution

689 Since the W boson transverse momentum cannot be measured in two different ways in order to
690 provide the reference for a hadronic recoil scale, determination of the hadronic recoil bias should
691 use the distributions, that are not sensitive to the truth P_T^W spectrum. One of the optimal choices
692 is the M_T^W distribution. The transverse mass distribution for a different scale choices is shown on a
693 Fig. 12.14. The expected contributions from signals and backgrounds are estimated with Monte Carlo
694 simulation, except for a multijet background, because its shape and number of events depends on
695 a hadronic recoil scale and thus needs to be recalculated for each value of HR_{SF} .

One of the possible ways to determine the correction factor is to use a difference in the mean of the transverse mass distributions in data and MC (Fig. 12.15). Statistical error on a correction factor is considered a dominating one and estimated as an standard error of mean $\sigma(\langle M_T^W \rangle)$, that is

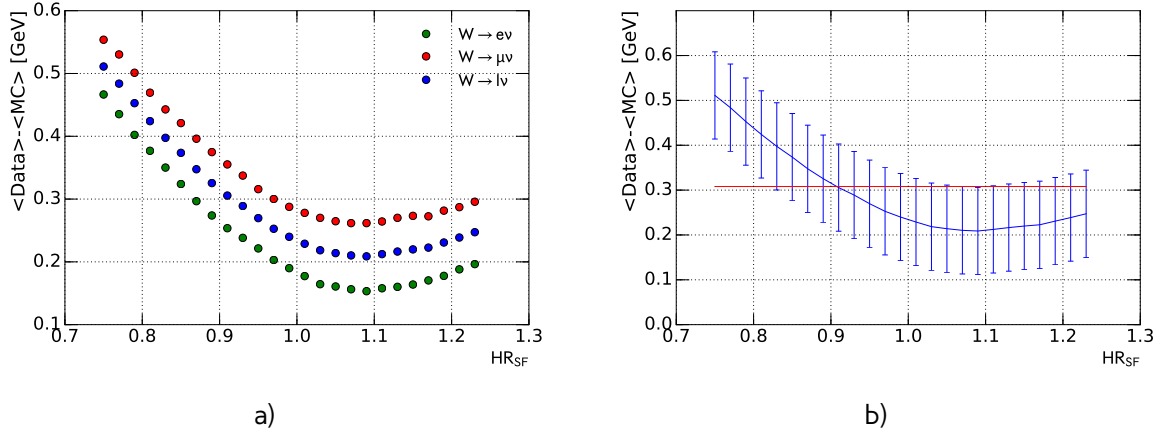


Fig. 12.15: a) Distribution of difference in a mean transverse momentum $\langle M_T^W \rangle$ between data and MC as a function of hadronic recoil scale HR_{SF} for different W boson channels. b) Distribution of difference in a mean transverse momentum $\langle M_T^W \rangle$ between data and MC as a function of hadronic recoil scale HR_{SF} for combined $W \rightarrow l\nu$ selection. Errors for each point are calculated as a standard error of mean. Below red line are values of HR_{SF} within 1σ uncertainty. The expected contributions from signals and backgrounds are estimated with Monte Carlo simulation, except for a QCD background, that is not included.

calculated as:

$$\sigma(\langle M_T^W \rangle) = \frac{\sigma(M_T^W)}{\sqrt{N}} \quad (12.10)$$

where $\sigma(M_T^W)$ is a standard deviation of M_T^W distribution and N is a total number of events used. The minimum difference is obtained at $HR_{SF} = 1.1 \pm 0.2$. The precision of this method is low, as it is mainly used as a cross-check of other methods.

Distribution of χ^2 for different W selections is shown in Fig. 12.16 a). Because of the possible mismodelling of the tail M_T^W distribution events with $M_T^W > 100$ GeV are not included in a χ^2 calculation. There is a visible peak in the χ^2 distribution for events from $W \rightarrow e\nu$ selection, coming from the missing QCD background. Hadronic recoil bias parameters are determined through the fit of χ^2 distribution in combined $W \rightarrow l\nu$ channel with the function from Eq. 12.9. The resulting bias is $HR_{SF} = 1.02 \pm 0.06(stat)$.

Additionally, a cut on M_T^W lower value may be used to reduce the multijet background contamination. The M_T^W range introduces a source of systematic uncertainty in hadronic recoil scale determination. It is estimated by repeating the fit for the different M_T^W lower and upper values, as shown in Fig. 12.17. Fit range systematic error is 0.03, that is resulting in overall result for this method $HR_{SF} = 1.02 \pm 0.07$.

12.3.2 Bias determination using $u_{||}$ distribution

Similarly to the W channel, scale correction in the Z sample can be determined from the HR_{SF} scan in the $\frac{u_{||}}{p_T^l}$ distribution, as shown on a Fig. 12.18. All of the sources of backgrounds are considered negligible in this case. Results of χ^2 test for data and MC in different channel are shown in a Fig. 12.19. Fit of the combined $Z \rightarrow ll$ distribution gives the most precise estimation of hadron recoil

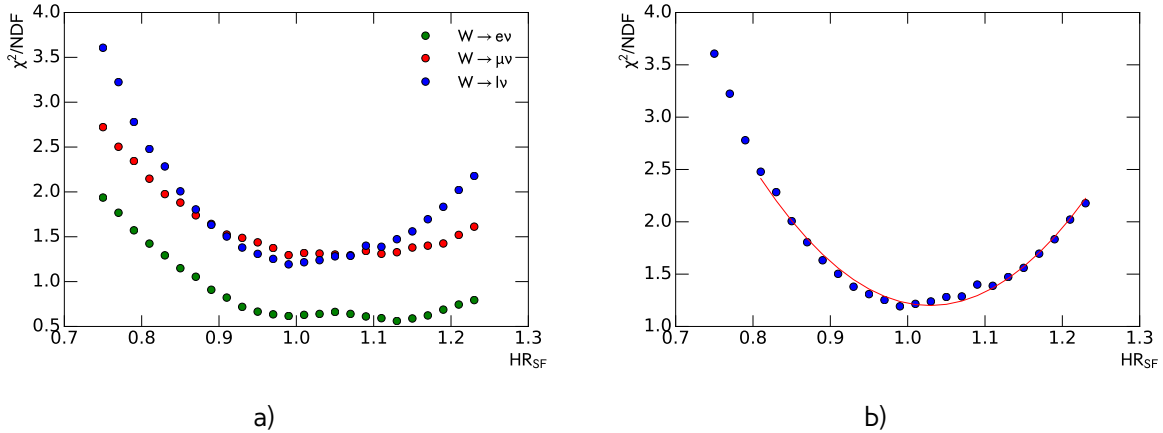


Fig. 12.16: a) Distribution of χ^2 between data and MC for transverse momentum $< M_T^W >$ as a function of hadronic recoil scale HR_{SF} for different W boson channels. b) Distribution of χ^2 between data and MC for transverse momentum $< M_T^W >$ as a function of hadronic recoil scale HR_{SF} for combined $W \rightarrow l\nu$ selection. Fit results are shown by a red line. The expected contributions from signals and backgrounds are estimated with Monte Carlo simulation, except for a QCD background, that is not included.

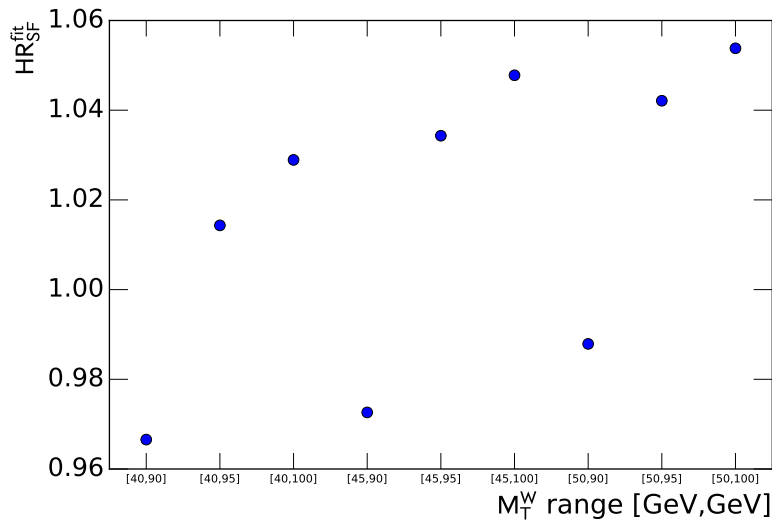


Fig. 12.17: Values of best hadron recoil biases obtained from the fit for events from combined $W \rightarrow l\nu$ selection as a function of fit range. The expected contributions from signals and backgrounds are estimated with Monte Carlo simulation, except for a QCD background, that is not included.

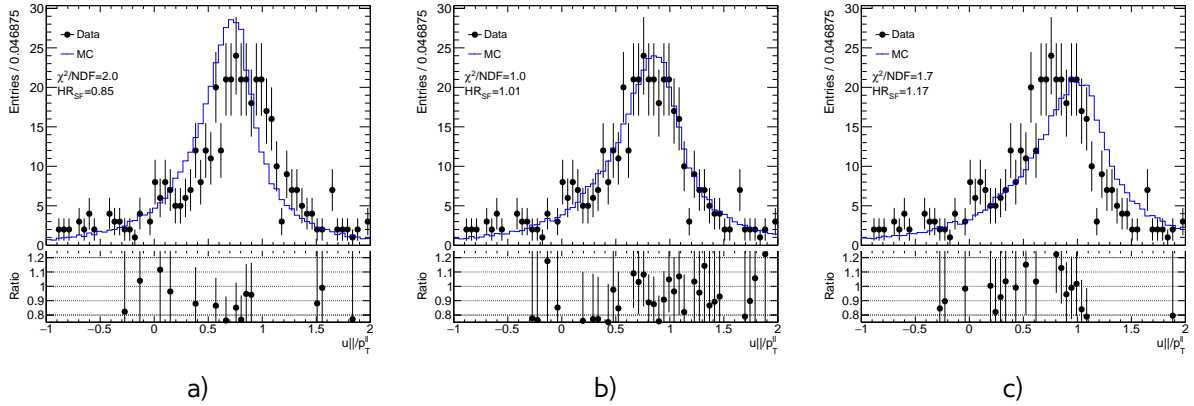


Fig. 12.18: Parallel hadronic recoil component u_{\parallel} from the $Z \rightarrow ee$ selection for different hadronic recoil scales: a) $HR_{SF}=0.75$ b) $HR_{SF}=1.1$ c) $HR_{SF}=1.23$. The expected contribution from signal is estimated with Monte Carlo simulation, other background sources are considered negligible.

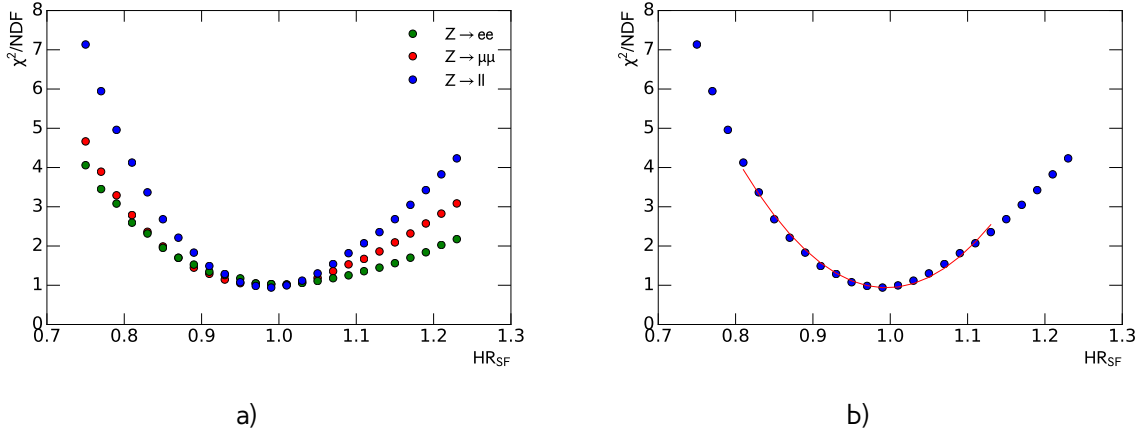


Fig. 12.19: a) Distribution of χ^2 between data and MC for transverse momentum $\langle M_T^W \rangle$ as a function of hadronic recoil scale HR_{SF} for different W boson channels. b) Distribution of χ^2 between data and MC for transverse momentum $\langle M_T^W \rangle$ as a function of hadronic recoil scale HR_{SF} for combined $W \rightarrow l\nu$ selection. Fit results are shown by a red line. The expected contribution from signal is estimated with Monte Carlo simulation, other background sources are considered negligible.

715 bias $HR_{SF} = 1.00 \pm 0.01$. Since there is no choice of the range and dependency on P_T^{bos} modeling,
 716 there is just one statistical source of uncertainty.

717 12.3.3 Systematic uncertainty estimation

718 Results on a hadron scale factors and its errors are shown in a Table 12.3. The results are consistent
 719 within one sigma. As a final result it was decided to choose HR_{SF} determined from $Z \rightarrow ll$ selection
 720 as a correction factor, leaving other as a reference cross-check.

721 Effect of the hadronic recoil bias correction for different bias scale factors presented in Fig. 12.20.
 722 Systematical error, coming from bias correction estimated using offset method (see Chap. 15).

Table 12.3: Hadronic recoil bias determination results and errors for different methods.

Method	SF	error
Mean M_T^W	1.10	0.2
$M_T^W \chi^2$	1.01	0.07
$u_{\parallel} \chi^2$	1.00	0.014

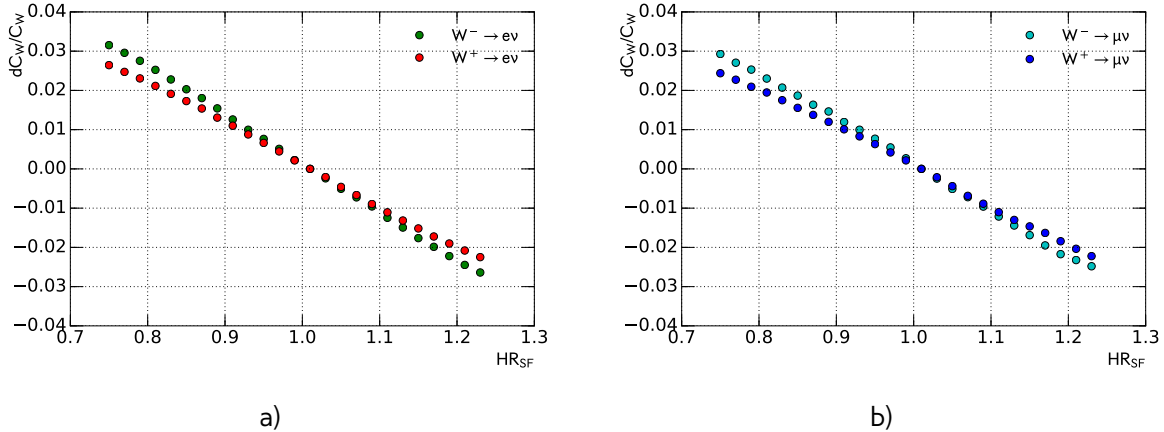

 Fig. 12.20: Effect on a C_W for a different $d\sigma$ for a) $W \rightarrow e\nu$ b) $W \rightarrow \mu\nu$ channel

 Table 12.4: Hadronic recoil bias systematics for different W boson channels.

Systematic source	$W^+ \rightarrow e^+\nu$	$W^- \rightarrow e^-\nu$	$W^+ \rightarrow \mu^+\nu$	$W^- \rightarrow \mu^-\nu$
Hadronic recoil resolution	-0.2%	-0.11%	-0.16%	-0.12%
Hadronic recoil scale	0.21%	0.20%	0.23%	0.24%

723 12.4 Summary on hadronic recoil systematics

724

Chapter 13

Background estimation

726

13.1 QCD background estimation	76
13.1.1 Template selection	77
13.1.2 Methodology of the template sample normalization	77
13.1.3 Systematic Uncertainty from the Multi-jet Background Estimation	79
13.2 Background-subtracted W and Z candidate events	81

736 After the event selection described in Chap. 10 the background contribution is around 4% for
 737 W-analysis and 0.2% for Z analysis (which with this statistics is negligible). Main backgrounds for W
 738 analysis are coming from:

- 739 • Processes with τ lepton, misidentified as an electron or muon + missing energy from neutrino
- 740 • Z decays with one missing lepton.
- 741 • QCD processes. In electron channel these are mostly jets faking electrons, while in the muon
 742 channel it consists mainly of a real muons produced in decays of heavy-flavor mesons.

743 Most of the backgrounds are estimated using MC. They are normalized using highest cross-section
 744 order available. The total list of simulated backgrounds and its cross-section is shown in a Table 13.1.
 745 The QCD background is estimated using data driven method.

Table 13.1: Background processes with their associated cross sections and uncertainties. The quoted cross sections are used to normalise estimates of expected number of events

Process	$\sigma \cdot BR$ [pb]	Order
$W^+ \rightarrow l\nu$	2116(1.9)	NNLO
$W^- \rightarrow l\nu$	1267(1.0)	NNLO
$Z \rightarrow ll$	303(0.2)	NNLO
$Z \rightarrow \tau\tau$	303	LO
$t\bar{t}$	7.41	LO
WW	0.6	LO
ZZ	0.7	LO
WZ	0.2	LO

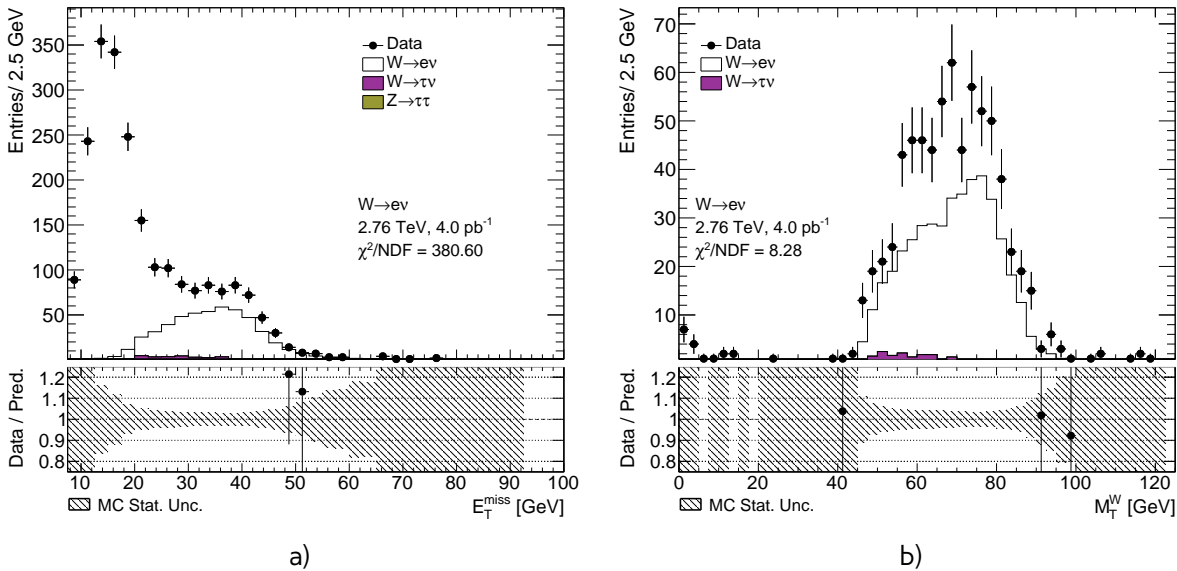


Fig. 13.1: Distribution for a) missing transverse energy E_T^{miss} b)mass transverse M_T^W from the QCD template selection for $W \rightarrow e\nu$ events

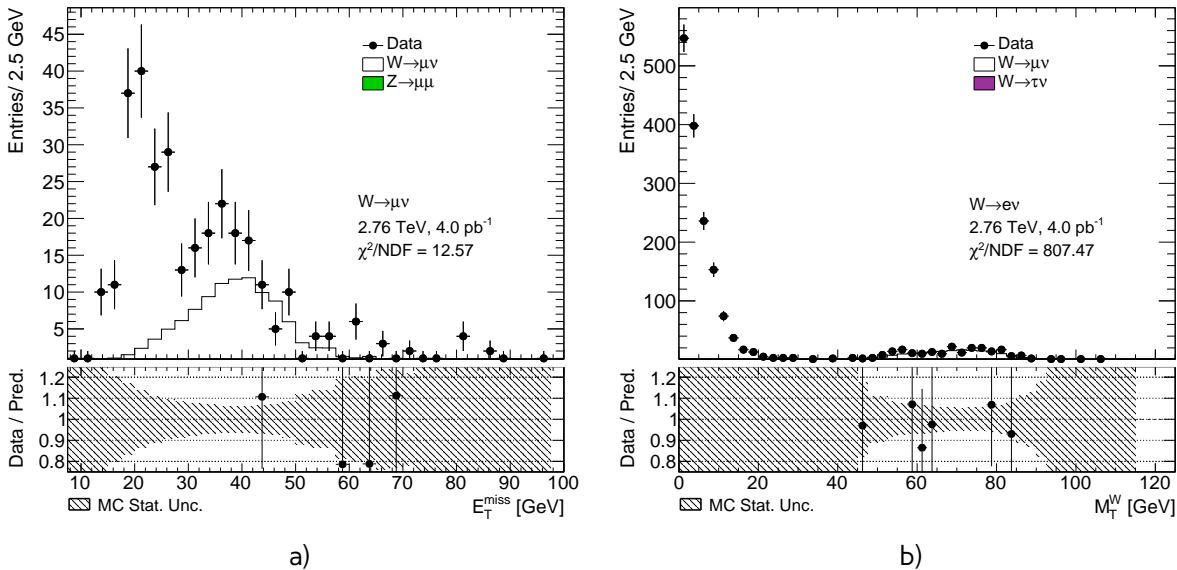


Fig. 13.2: Distribution for a) missing transverse energy E_T^{miss} b)mass transverse M_T^W from the QCD template selection for $W \rightarrow \mu\nu$ events

13.1 QCD background estimation

There is a small probability, that a jet can fake W -boson decay with isolated lepton and E_T^{miss} through the energy mismeasurement in the event. Event selection is suppressing this type of background, but not fully eliminating it. Due to a large jet production cross-section and complex composition, generation of MC events becomes impractical. This is why data driven technique for QCD background estimation have been used. In our case contribution from the QCD background in the Z sample is negligible(Fig. 14.15), so it is estimated just for $W \rightarrow e\nu$ and $W \rightarrow \mu\nu$ processes.

753 Data driven method allows to have model independent predictions with small statistical uncertainty.
 754 This method is using *QCD* enriched region, where signal events are suppressed. This is usually done
 755 by reversing identification or isolation criteria. It is assumed, that shape of the *QCD* background
 756 stays the same in the signal region. Normalization can be derived in a control region through the
 757 template fit.
 758 This section describes method of *QCD* background determination, that have been used in 2.76
 759 TeV data.

760 13.1.1 Template selection

761 A study have been performed to determine appropriate template selection. Because of the origin
 762 of the *QCD* backgrounds, missing transverse energy E_T^{miss} should be smaller in background sample,
 763 that in a signal region. Releasing E_T^{miss} cut allows to gain a bigger statistics for a *QCD* template.
 764 Another possibility is to relax the transverse mass M_T^W cut. Most of the multijet background event
 765 should contribute to the small M_T^W region. The template sample can contain also contributions from
 766 other backgrounds (mostly coming from $W \rightarrow l\nu$). The best template selection should allow for big
 767 data statistics and small electroweak contributions at the same time. In order to suppress the signal
 768 additionally reversed ID or isolation criteria is applied.

769 In electron channel, the template selection requires an electron candidate to fail medium identifi-
 770 cation criteria, but to pass loose selection. Control distributions for a different template selection in
 771 electron channel are shown on a Fig. 13.1. Relaxed E_T^{miss} cut allows to gain bigger template statistics.

772 In a muon channel template selection is build by inverting isolation criteria ($P_T^{cone,20} > 0.1$). In case of
 773 $W \rightarrow \mu\nu$ the *QCD* background template the best statistics is achieved by relaxing mass transverse
 774 M_T^W cut (Fig. 13.2).

775 In order to avoid double counting, electroweak processes (i.e. signal and backgrounds) are sub-
 776 tracted from a template. The total number of events in the template can be defined as:

$$N_{template} = N_{data}^{bkg\ enriched} - \sum_j^{MC} N_{MC_j}^{bkg\ enriched}, \quad (13.1)$$

777 where $N_{data}^{bkg\ enriched}$ and $N_{MC_j}^{bkg\ enriched}$ are numbers of the events in a background enriched sample in data
 778 and different MC samples. The resulting template statistic is 1348 and 1509 events for $W \rightarrow e\nu$ and
 $W \rightarrow \mu\nu$ respectively.

779 13.1.2 Methodology of the template sample normalization

The normalization is found through the χ^2 fit of the template and backgrounds to the data. The
 following composite model has been used for estimation:

$$M(x) = \sum_{i=1}^{N-1} f_i F_i(x) + (1 - \sum_{i=1}^{N-1} f_i) \cdot F_{QCD}(x), \quad (13.2)$$

780 where index i goes over the MC samples, x is a fit variable (E_T^{miss} or M_T^W), $F_i(x)$ and $F_{QCD}(x)$ are
 781 the probability density functions of MC samples and *QCD* background template respectively. Fit
 782 parameters f_i are the fractions of MC events within the fit region. In order to eliminate systematics,
 783 coming from the cross-section uncertainty, the signal fractions are left as free parameters of fit and
 784 and the background MC fractions are allowed to be varied within 5% uncertainty.

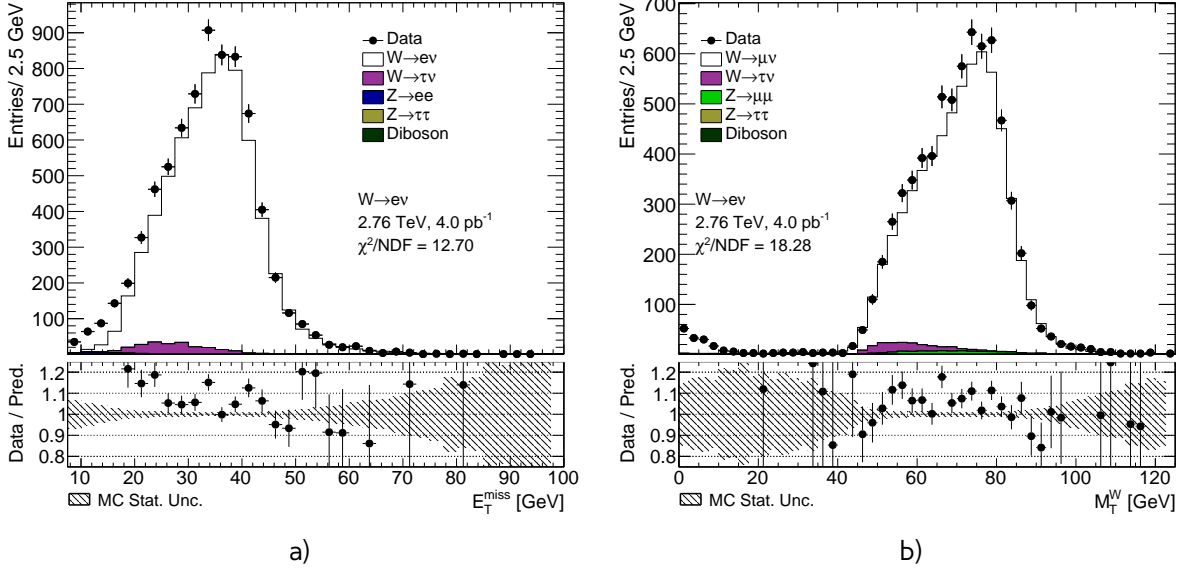


Fig. 13.3: Distributions used for multijet background estimation for a) $W \rightarrow e\nu$ b) $W \rightarrow \mu\nu$

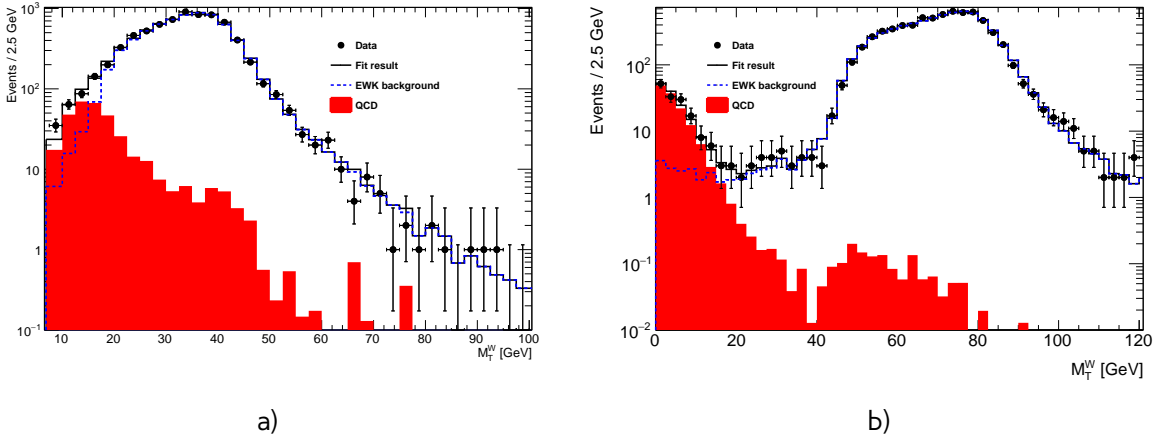


Fig. 13.4: The multijet background estimation for a) $W \rightarrow e\nu$ using reversed ID cut and released E_T^{miss} cut b) $W \rightarrow \mu\nu$ using released M_T^W cut and $b\bar{b} + c\bar{c}$ template

Normalisation scale of the QCD events is calculated from the obtained fit parameters as:

$$scale = \frac{(1 - \sum f_i) \cdot N_{Data}^{fit}}{N_{template}}, \quad (13.3)$$

where $\sum f_i$ is a sum of all fractions in the fit, N_{Data}^{fit} is a number of data events in a fit histogram and $N_{template}$ is a number of event in a template. The fit is performed separately for W^+ and W^- . Additionally, fit in total W channel is used as a cross-check of the fit. The results of the fitting procedure are shown on a Fig. 13.4 .

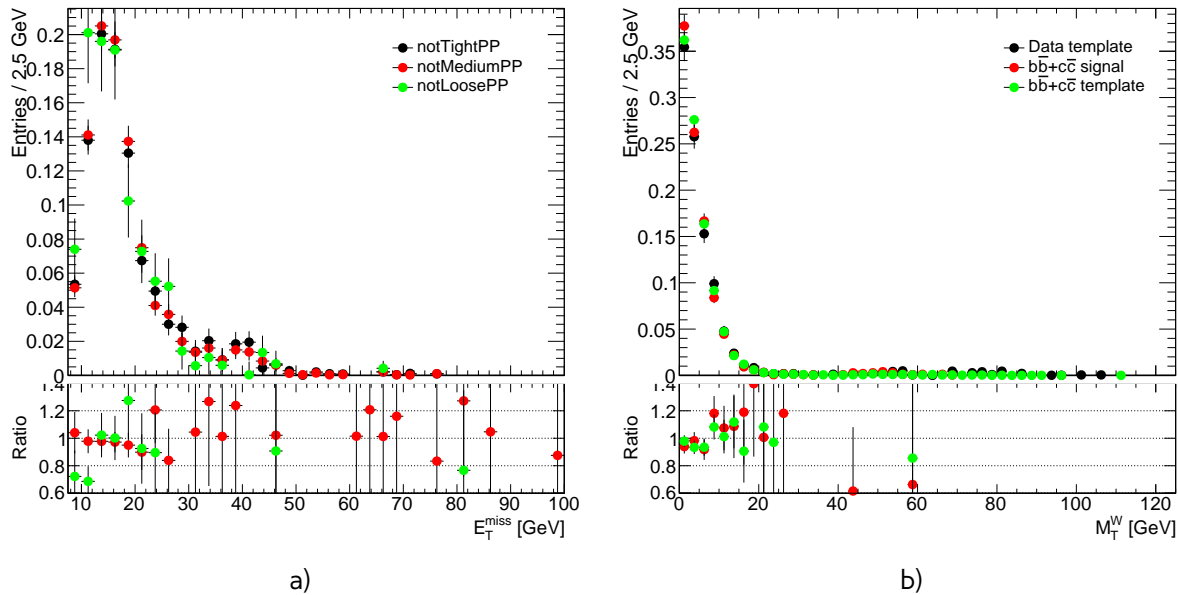


Fig. 13.5: Data and MC comparison for E_T^{miss} calculated by standard ATLAS algorithm for a) $W \rightarrow e\nu$
b) $W \rightarrow \mu\nu$ events

788 13.1.3 Systematic Uncertainty from the Multi-jet Background Estimation

The uncertainty of the multi-jet background estimation can be divided into 3 main components:

$$\delta_{QCD} = \sqrt{\delta_{fit\,unc}^2 + \delta_{MC}^2 + \delta_{fit\,bias}^2 + \delta_{template}^2}, \quad (13.4)$$

789 where $\delta_{fit\,unc}$ is the uncertainty for a scale from a χ^2 fit. The meaning of other components is
790 explained below

The second component δ_{MC} is coming from a possible mismodelling of MC in a fitted region. It can be estimated by comparison of fit results for W , W^+ and W^- . Number of multijet background events should not depend on a charge of the analysis, so it is expected:

$$N_{QCD}^W = 0.5 \cdot N_{QCD}^{W^+} = N_{QCD}^{W^-} \quad (13.5)$$

791 Standard deviation of these 3 numbers is taken as systematic uncertainty. Since in $W \rightarrow \mu\nu$ channel
792 the QCD template normalization is derived from the fit in small M_T^W region, where electroweak
793 contributions negligible and data statistics is high, this systematic source is equal to 0.

794 The third component $\delta_{fit\,bias}$ is coming from an effect of an arbitrary choice of bin size. This error
795 is estimated by repeating the fit for a different binnings. This component is assumed negligible in
796 $W \rightarrow \mu\nu$ case.

797 The uncertainty $\delta_{template}$ is due to a potential bias in the template as a result of the template choice
798 and a template statistics itself. For estimation of this uncertainty different template selections have
799 been used. For $W \rightarrow e\nu$ channel different reversed isolation criteria have been tried (Fig. 13.5 a)).
800 The overall discrepancies can be considered negligible. For $W \rightarrow \mu\nu$ channel template variations
801 are estimated using fits with $b\bar{b} + c\bar{c}$ MC samples. Fig. 13.5 b) compares data template with template
802 obtained using signal selection with released M_T^W cut and template selection. Results for a different

Table 13.2: Results of QCD background estimation for $W \rightarrow e\nu$ and corresponding error

Charge	N_{QCD}	$\delta N_{fit\,unc}$	δN_{MC}	$\delta N_{fit\,bias}$
W^+	38.3	7.0	7.0	5.0
W^-	21.5	0.7	-9.4	4.0
W	66.1	21.2	4.2	10.
Total	31.0	6.1	8.6	4.7

 Table 13.3: Results of QCD background estimation for $W \rightarrow \mu\nu$ using different templates and it's fit error

Charge	N_{QCD} data template	N_{QCD} $b\bar{b} + c\bar{c}$ template selection	N_{QCD} $b\bar{b} + c\bar{c}$ signal selection
W^+	2.48	0.73	1.34
W^-	2.48	0.73	1.35
W	4.97	1.47	2.70
Total per channel	2.48	0.73	1.35
Fit error	0.60	0.73	0.19

803 template fits are presented in Tab 13.3

804 Results of the QCD background uncertainty estimation for $W \rightarrow e\nu$ and $W \rightarrow \mu\nu$ are shown
 805 in Tab. 13.2 and 13.3 respectively. The overall number of QCD background events is estimated as
 806 31.00 ± 13.0 for $W^+ \rightarrow e^+\nu$ and $W^- \rightarrow e^-\nu$ and 1.50 ± 0.9 for $W^+ \rightarrow \mu^+\nu$ and $W^- \rightarrow \mu^-\nu$. The
 807 overall fraction of the QCD events is lower, than in 13 TeV [?], 8 TeV [?] and 7 TeV [?] data, what is in
 808 agreement with expectations.

 Table 13.4: Number of observed candidate events for the $W \rightarrow l\nu$ channel, electroweak (EWK) and top, and data-driven QCD background events, and background-subtracted signal events

I	Observed candidates	Background (EWK + top)	Background (Multijet)	Background-subtracted data N_W^{sig}
W boson				
e^+	3914	108.1 ± 5.6	31.00 ± 13.0	$3774.9 \pm 62.6 \pm 5.6 \pm 13.0$
e^-	2209	74.2 ± 3.3	31.00 ± 13.0	$2103.8 \pm 47.0 \pm 3.3 \pm 13.0$
μ^+	4365	150.5 ± 6.6	1.50 ± 0.9	$4213.0 \pm 66.1 \pm 6.6 \pm 0.9$
μ^-	2460	105.6 ± 4.1	1.50 ± 0.9	$2352.9 \pm 49.6 \pm 4.1 \pm 0.9$
Z boson				
e	430	1.2 ± 0.0	-	$428.8 \pm 20.7 \pm 0.0$
μ	646	1.5 ± 0.0	-	$644.5 \pm 25.4 \pm 0.0$

809 13.2 Background-subtracted W and Z candidate events

810 Tables 13.4 summarize the number of background events for W and Z selections. Uncertainties on
811 a number of EWK+top events are coming from a statistics, cross-section uncertainty (if given) and
812 3% of luminosity determination uncertainty. For multijet background uncertainty is coming from a
813 method and described in a subsection 13.1.3. For the background-subtracted events the statistical
814 uncertainty is quoted first, followed by the total systematic uncertainty, derived from the EWK+top
815 and multijet background ones, considering the sources as uncorrelated.

816

Chapter 14

817

Control distributions

818 Kinematic distributions after all cuts (Section 10) and corrections applied on MC (Section 11), are
 819 presented in this chapter. Distributions for $W \rightarrow l\nu$ are split in charge and shown on a Figs. 14.1-
 820 14.12. Distributions for $Z \rightarrow l^+l^-$ analysis are shown on a Fig. 14.13-14.17.

821 These plots also showing the systematic and statistical uncertainty as a shaded band. The un-
 822 certainties are including all sources, described in a 15, except for uncertainties coming from shape
 823 variation due to a PDF reweighting and QCD background and luminosity. All uncorrelated uncertainty
 824 sources are summed in quadrature. The expected background contributions are estimated using MC
 825 simulations, apart from QCD background, which is found with a data driven method, as explained in
 826 a previous chapter.

827 Good overall agreement between data and MC is observed.

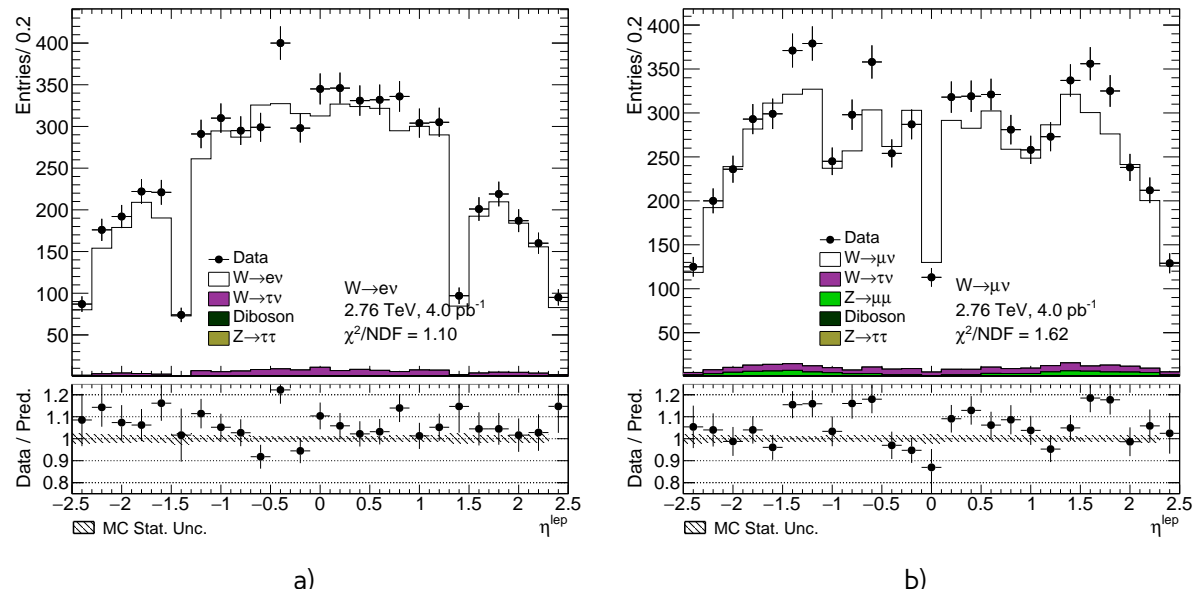


Fig. 14.1: Lepton pseudorapidity distribution from the a) $W \rightarrow e\nu$ selection and b) the $W \rightarrow \mu\nu$ selection.

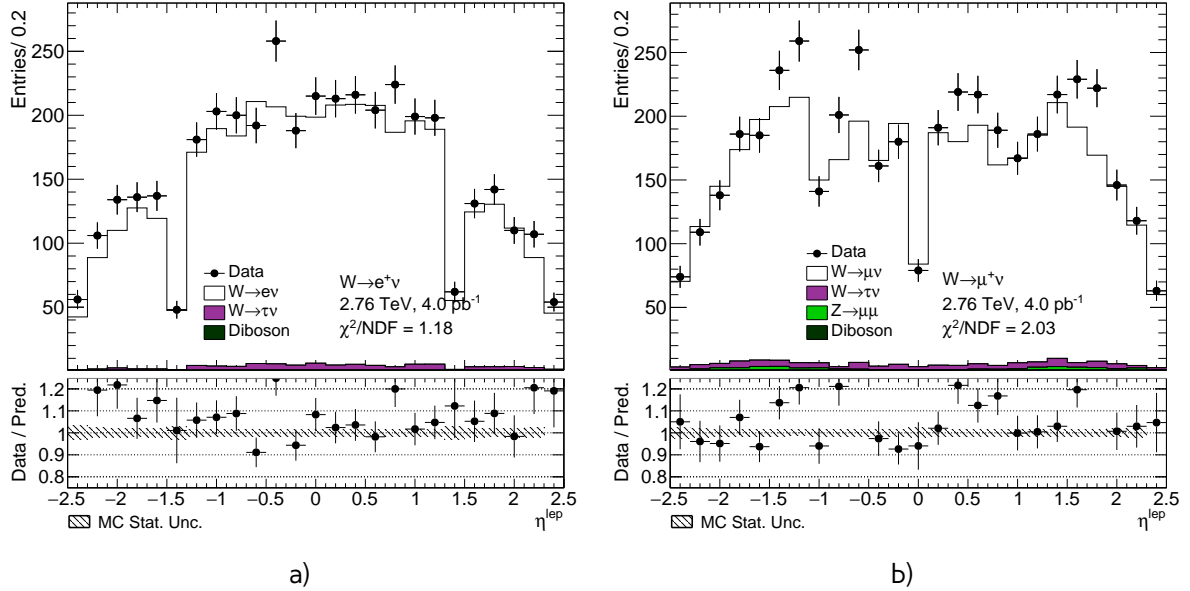


Fig. 14.2: Lepton pseudorapidity distribution from the a) $W^+ \rightarrow e^+\nu$ selection and b) the $W^+ \rightarrow \mu^+\nu$ selection.

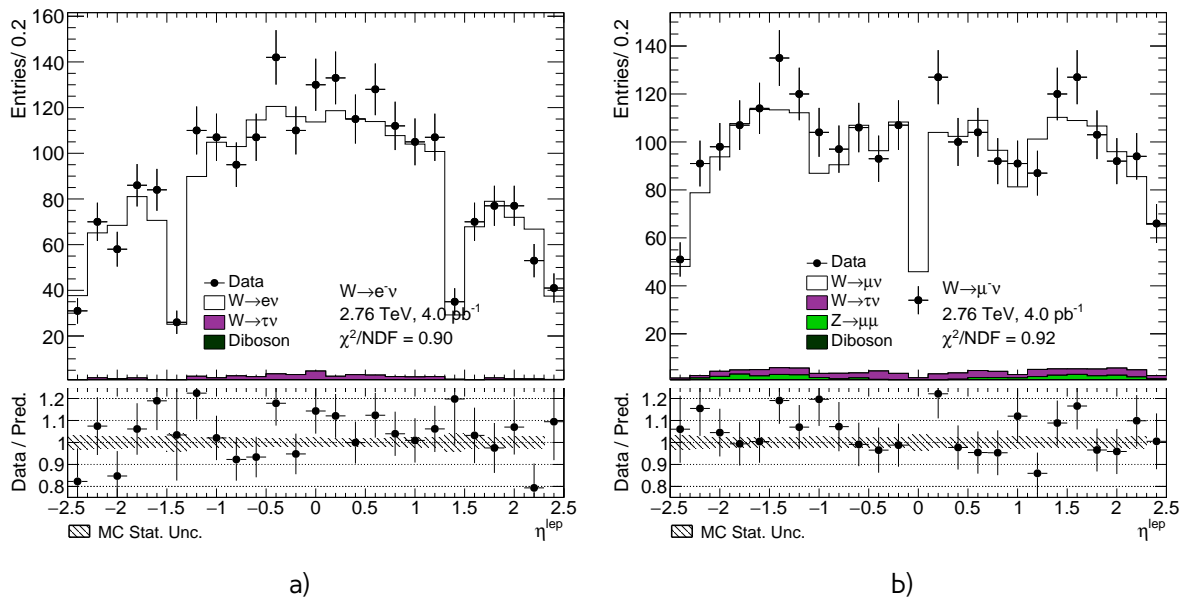


Fig. 14.3: Lepton pseudorapidity distribution from the a) $W^- \rightarrow e^-\nu$ selection and b) the $W^- \rightarrow \mu^-\nu$ selection.

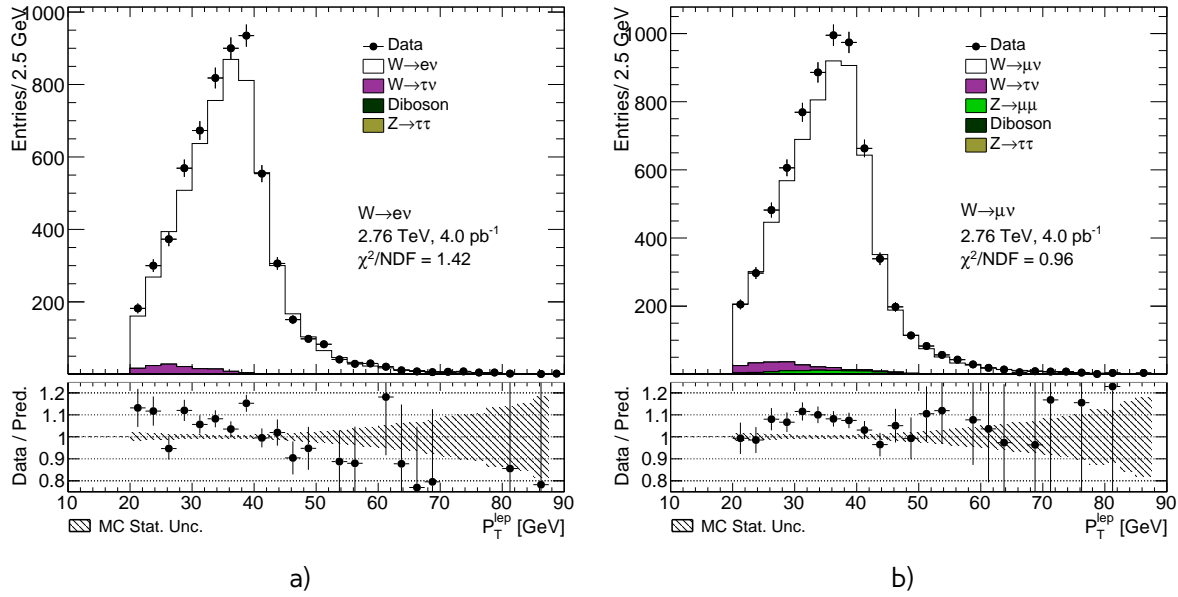


Fig. 14.4: Lepton transverse momentum distribution from the a) $W \rightarrow e\nu$ selection and b) the $W \rightarrow \mu\nu$ selection.

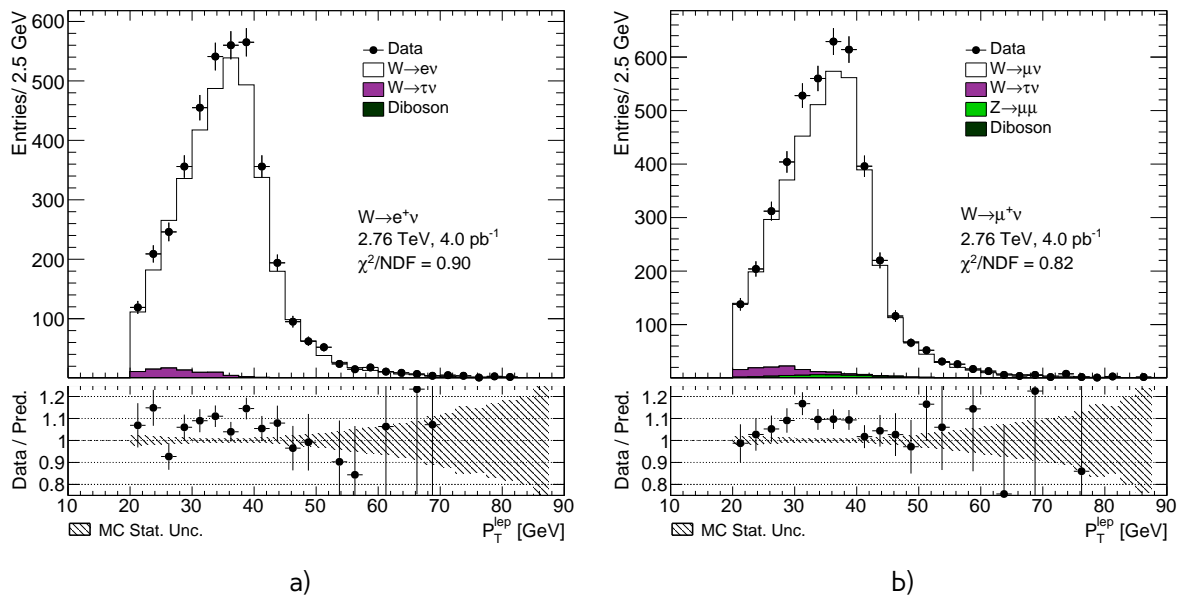


Fig. 14.5: Lepton transverse momentum distribution from the a) $W^+ \rightarrow e^+\nu$ selection and b) the $W^+ \rightarrow \mu^+\nu$ selection.

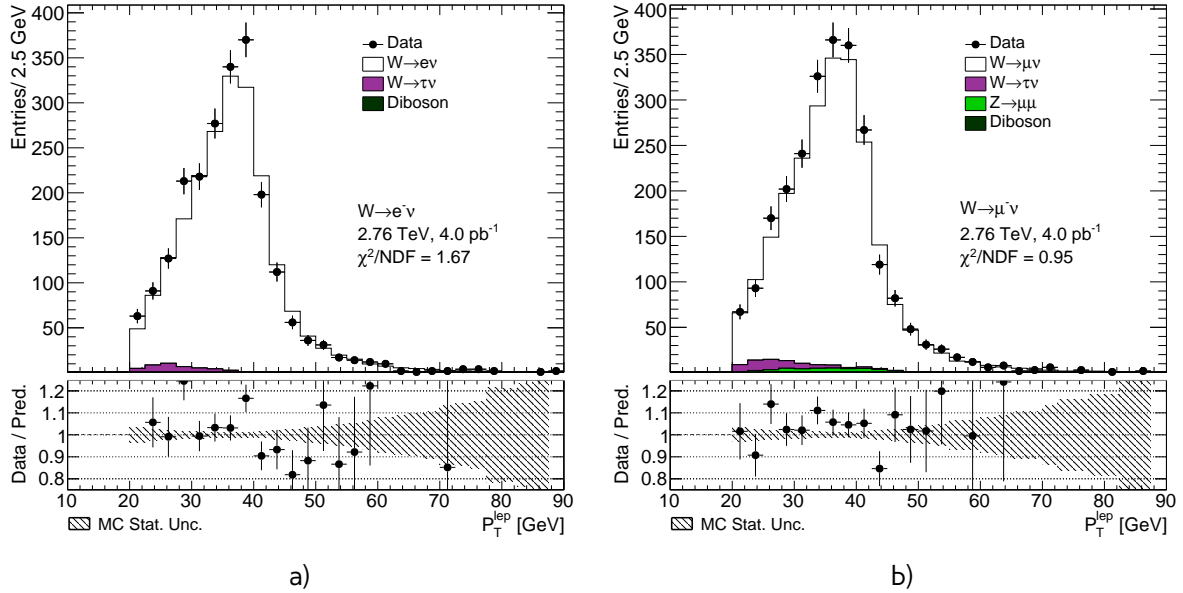


Fig. 14.6: Lepton transverse momentum distribution from the a) $W^- \rightarrow e^- \nu$ selection and b) the $W^- \rightarrow \mu^- \nu$ selection.

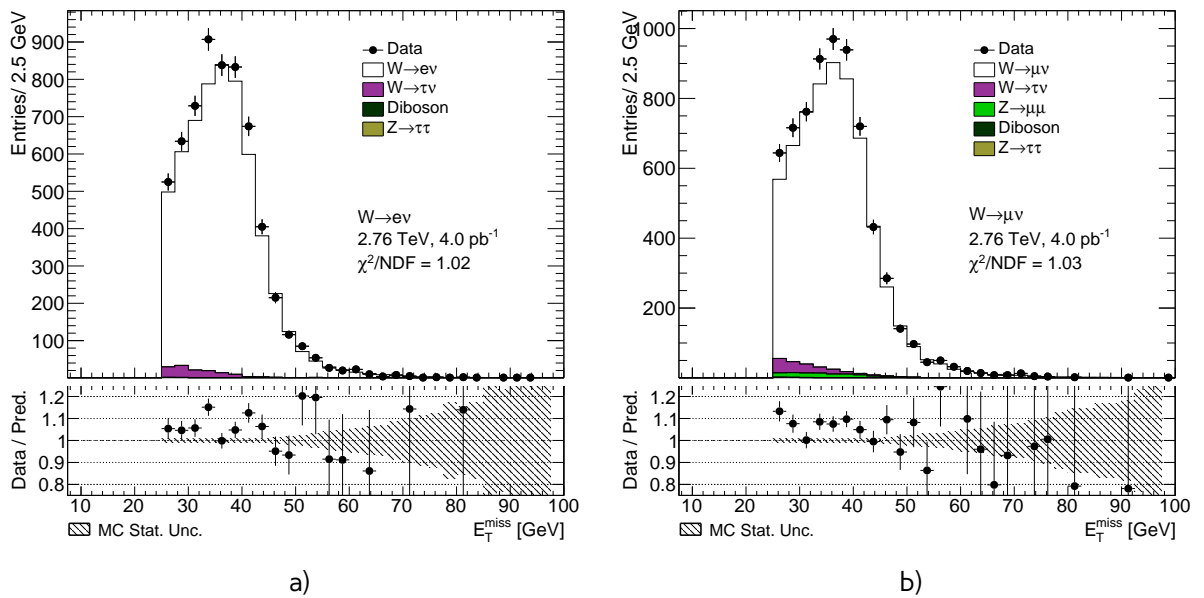


Fig. 14.7: Missing transverse energy distribution from the a) $W \rightarrow e\nu$ selection and b) the $W \rightarrow \mu\nu$ selection.

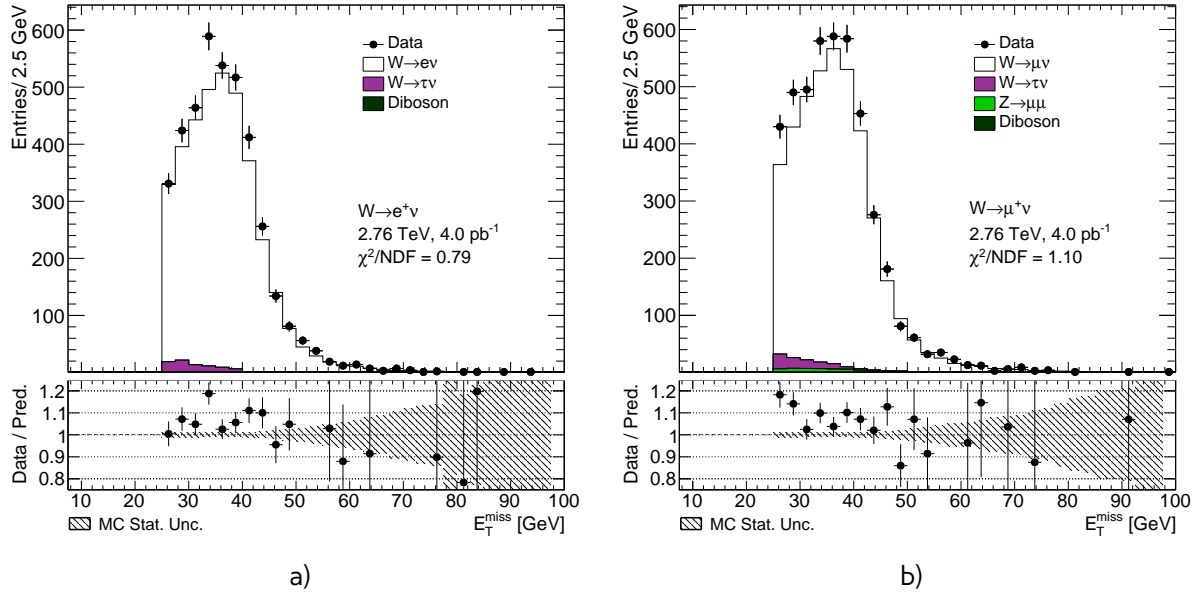


Fig. 14.8: Missing transverse energy distribution from the a) $W^+ \rightarrow e^+\nu$ selection and b) the $W^+ \rightarrow \mu^+\nu$ selection.

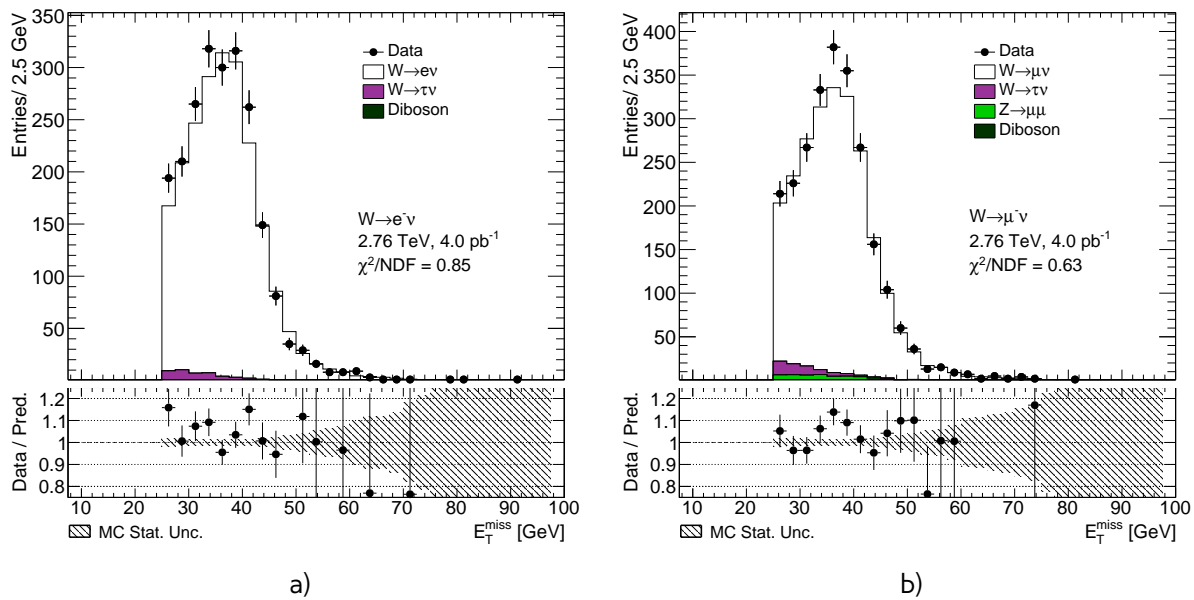


Fig. 14.9: Missing transverse energy distribution from the a) $W^- \rightarrow e^-\nu$ selection and b) the $W^- \rightarrow \mu^-\nu$ selection.

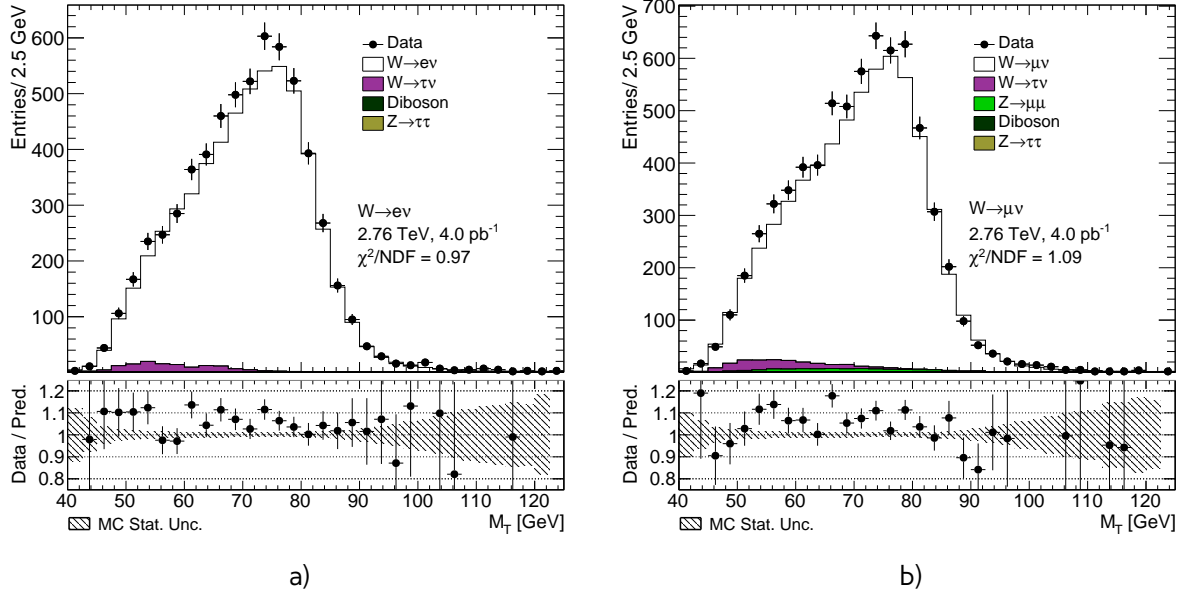


Fig. 14.10: Transverse mass distribution distribution from the a) $W \rightarrow e\nu$ selection and b) the $W \rightarrow \mu\nu$ selection.

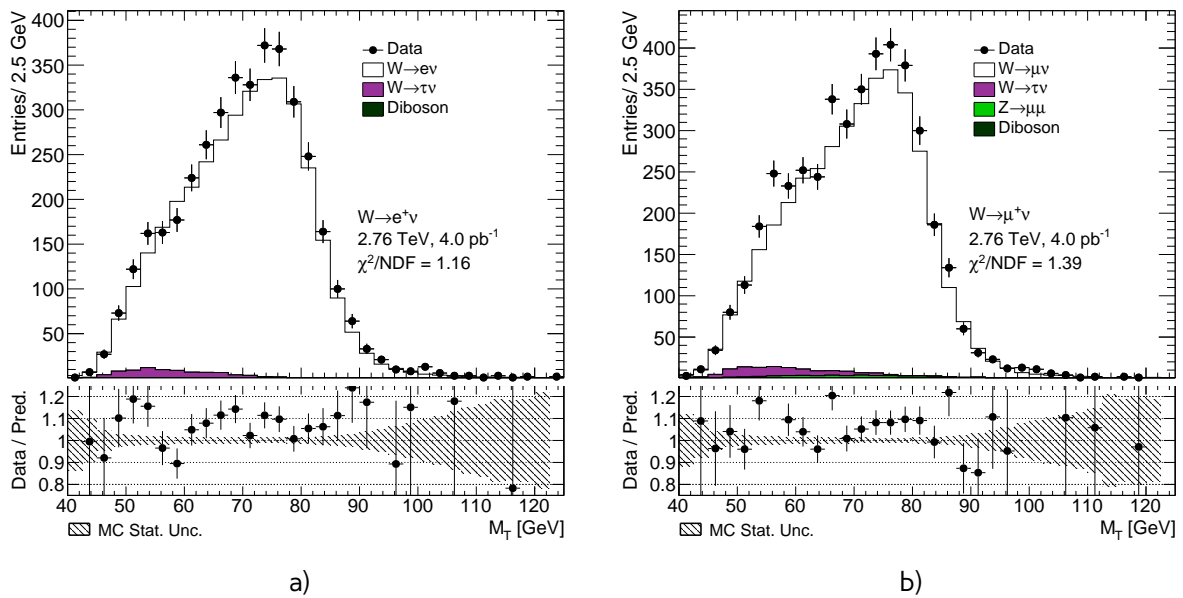


Fig. 14.11: Transverse mass distribution distribution from the a) $W^+ \rightarrow e^+\nu$ selection and b) the $W^+ \rightarrow \mu^+\nu$ selection.

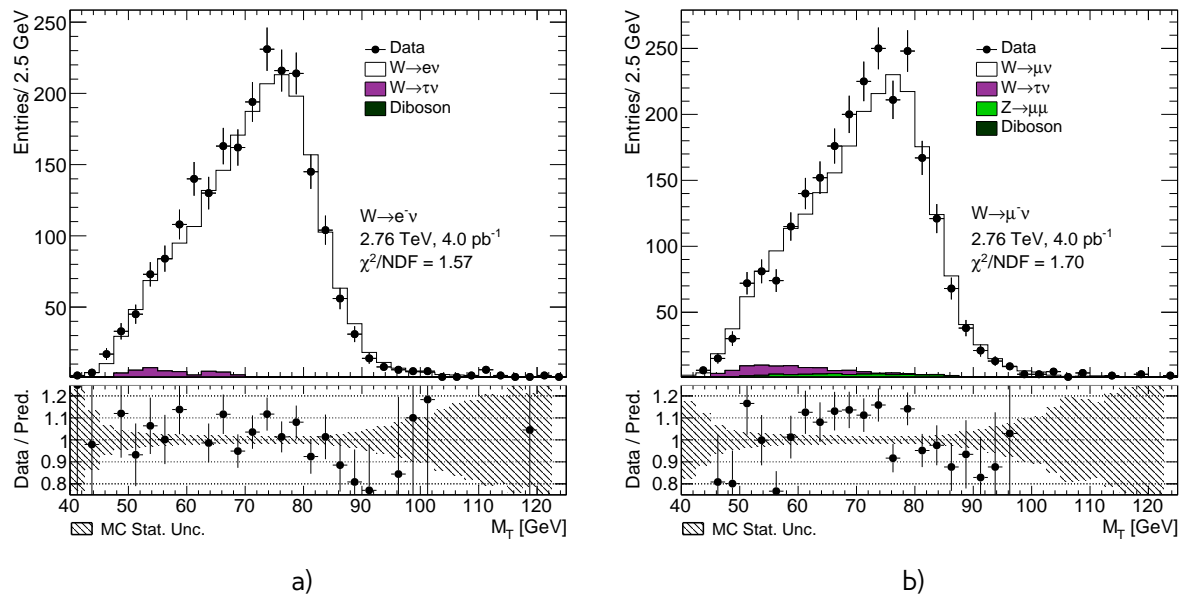


Fig. 14.12: Transverse mass distribution distribution from the a) $W^- \rightarrow e^-\nu$ selection and b) the $W^- \rightarrow \mu^-\nu$ selection.

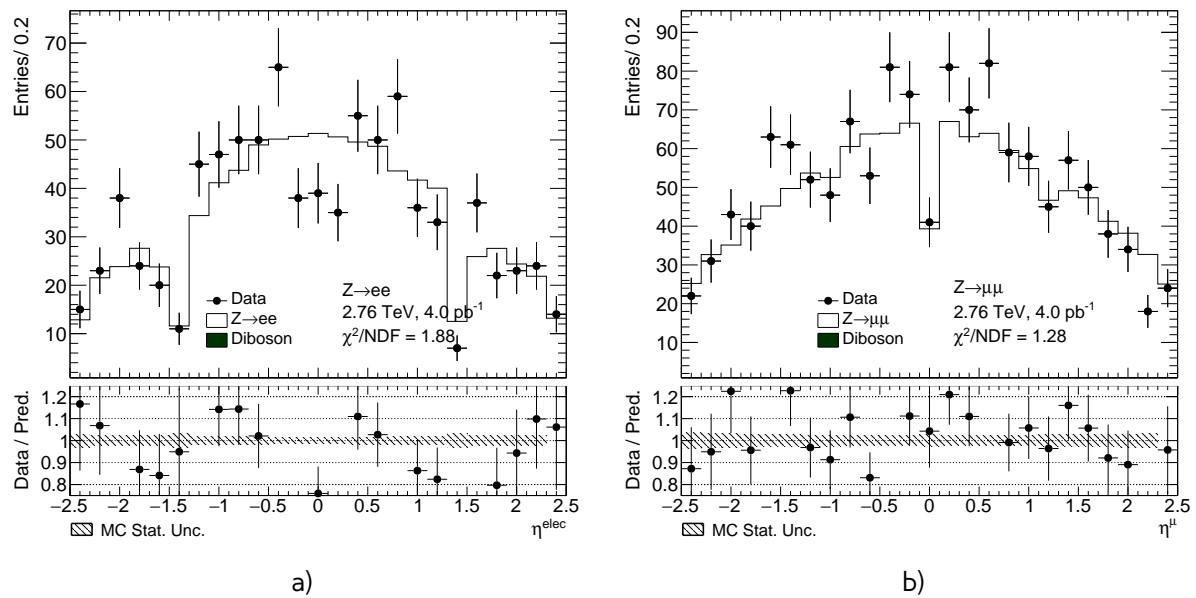


Fig. 14.13: Lepton pseudorapidity distributions from the a) $Z \rightarrow e^+e^-$ b) $Z \rightarrow \mu^+\mu^-$

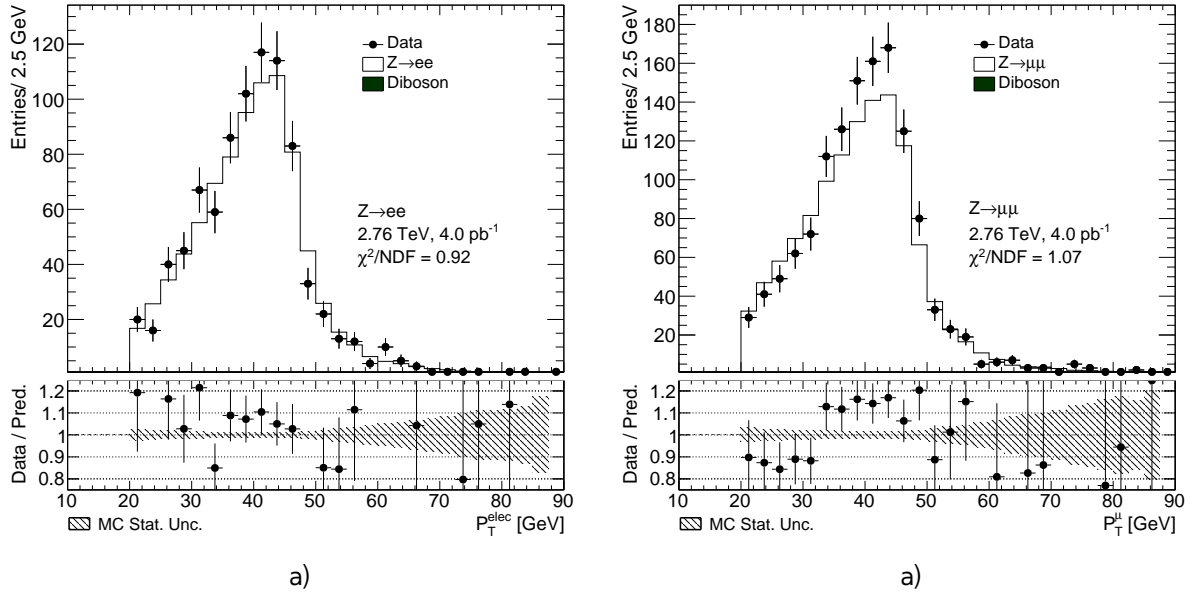


Fig. 14.14: Lepton transverse momentum distributions from the a) $Z \rightarrow e^+e^-$ b) $Z \rightarrow \mu^+\mu^-$

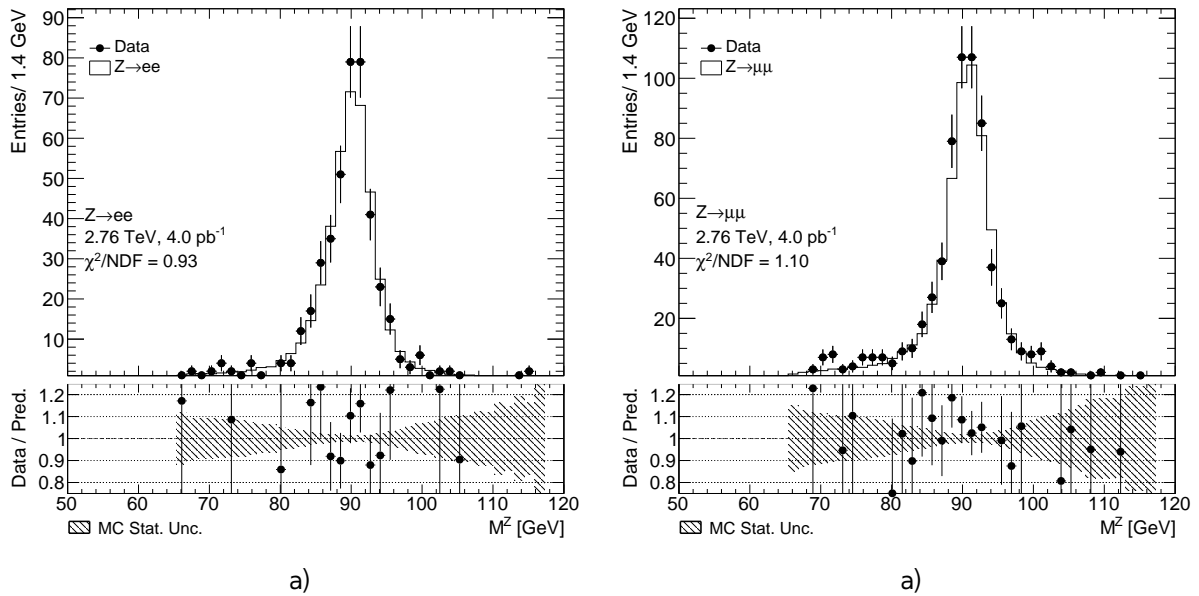


Fig. 14.15: Dilepton mass distribution distributions from the a) $Z \rightarrow e^+e^-$ b) $Z \rightarrow \mu^+\mu^-$

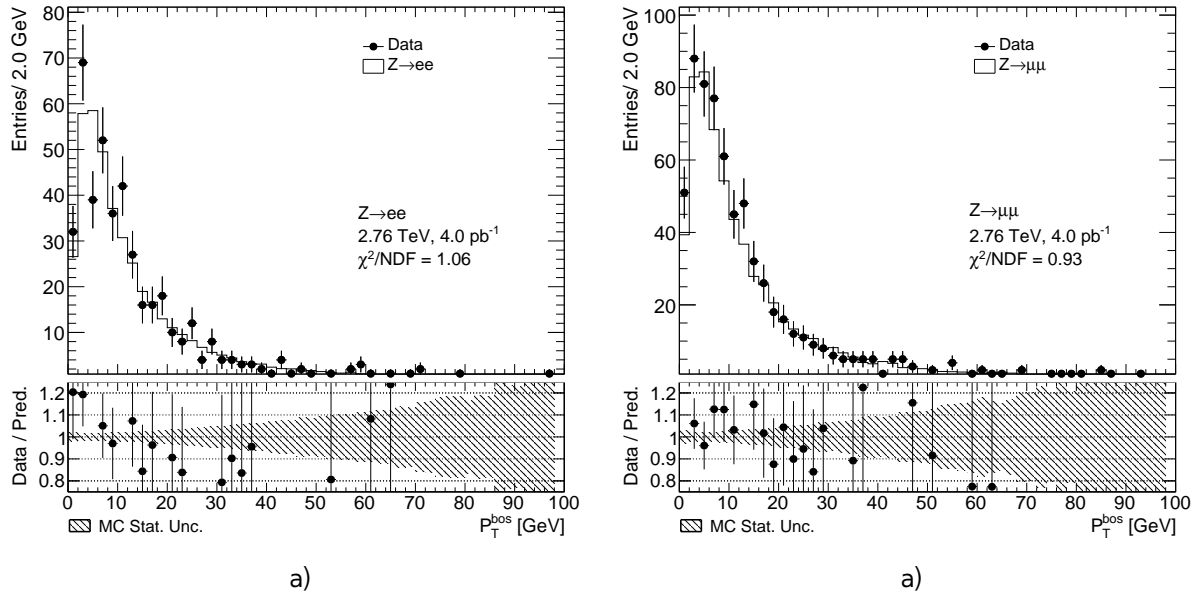


Fig. 14.16: Z boson transverse momentum distributions from the a) $Z \rightarrow e^+e^-$ b) $Z \rightarrow \mu^+\mu^-$

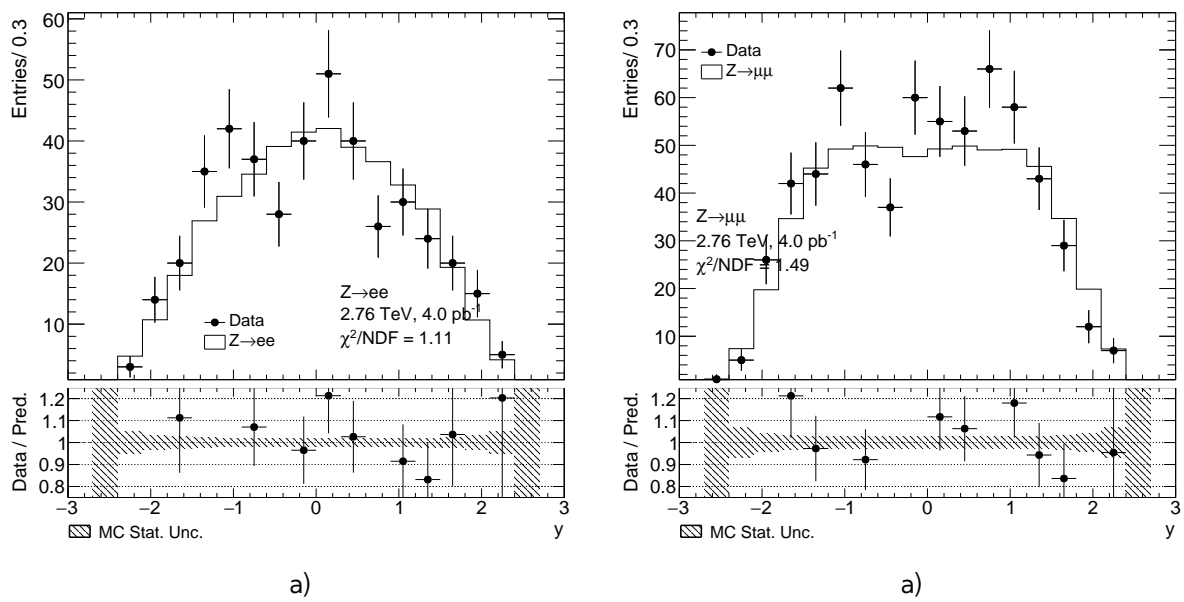


Fig. 14.17: Z boson rapidity distribution from the a) $Z \rightarrow e^+e^-$ b) $Z \rightarrow \mu^+\mu^-$

828 Chapter **15**

829 **Uncertainties in the cross-section measurement**

830	15.1 Methods of uncertainties propagation	93
831	15.2 Experimental systematic uncertainties	94
832	15.2.1 Electron energy scale and resolution	94
833	15.2.2 Muon energy scale and resolution	94
834	15.2.3 Muon and electron efficiency toy Monte-Carlo	94
835	15.3 Theoretical uncertainty	96
836	15.4 Correlation between uncertainties	96
837	15.4.1 Toy MC correlations	96
838	15.4.2 Correlations between PDF's eigenvectors	96

841 Cross-section measurement relies on theoretical models and corrections, used in Monte-Carlo.
842 Thus, their intrinsic uncertainties should be propagated to a final result. This chapter discusses
843 main methods of uncertainties measurements and sources on $C_{W,Z}$ and $A_{W,Z}$ correction factors.

844 **15.1 Methods of uncertainties propagation**

The offset method changes a correction by a $\pm 1\sigma$ of it's systematic uncertainty. The contribution of each correction's uncertainty on the observable (e.g. $C_{W,Z}$, $A_{W,Z}$ or a cross-section) is taken as a symmetric approximation:

$$U_i^{\text{offset}} = \frac{\sigma_i^{\text{up}} - \sigma_i^{\text{down}}}{2}, \quad (15.1)$$

845 where $\sigma_i^{\text{up(down)}}$ - the change in a observable due to the shift of the correction on σ up or down.

Another method used for a uncertainties propagation is a toy MC method, that uses a pseudo experiments with modified input corrections. For a scale factors binned p_T and η uncertainties inside each bin can be divided to a correlated and uncorrelated systematic components and statistical error. For each pseudo-experiment, a table of new scale factors is filled, where inside each bin a scale factor is randomly varied as:

$$SF_i^{\text{Toy}_n} = SF_i + \text{Gauss}(0, \Delta SF_i^{\text{uncorr+stat}}) + \sum \Delta SF_i^{\text{corr}} \cdot \text{Gauss}(0, 1), \quad (15.2)$$

846 where $SF_i^{\text{Toy}_n}$ is a new scale factor in i-th bin, $\Delta SF_i^{\text{uncorr+stat}}$ - is the quadratic sum of uncorrelated
847 and statistical errors and $\Delta SF_i^{\text{corr}}$ is a correlated error.

The overall effect on a observable is calculated as a standard deviation of the values in a pseudo-experiments:

$$U_i = \sqrt{\frac{\sum_{Toy_n=1}^N \sigma_i^2}{N} - \left(\frac{\sum_{Toy_n=1}^N \sigma_i}{N}\right)^2} \quad (15.3)$$

851 The number N of pseudo experiments should be sufficiently large to avoid possible bias in the
852 uncertainty estimation.

853 **15.2 Experimental systematic uncertainties**

854 Sources of experimental uncertainties, methods of estimation and their effect on a $C_{W,Z}$ are sum-
855 marized in a Tab. 15.1. Systematical errors coming from a hadron recoil calculation are discussed in
856 a Sec. 12.

857 **15.2.1 Electron energy scale and resolution**

858 Electron energy scale correction, described in Sec. 11.2 has associated uncertainties coming from
859 <reference>:

- 860 • Statistical component of the scale uncertainty
- 861 • Uncertainty from the possible bias of the calibration method
- 862 • Scale uncertainty from the choice of generator
- 863 • Uncertainty from the presampler energy scale
- 864 • Imperfect knowledge of the material in front of EM calorimeter.

865 The uncertainty contribution from each component is estimated using offset method. The total
866 energy scale uncertainty is the quadratic sum of the components <reference>.

867 **15.2.2 Muon energy scale and resolution**

- 868 • MS modelling
- 869 • ID modelling
- 870 • overall scale

871 The uncertainty contribution from each component is estimated using offset method. The total
872 energy scale uncertainty is the quadratic sum of the components

873 **15.2.3 Muon and electron efficiency toy Monte-Carlo**

874 In case of 2.76 TeV analysis scale factor errors are considered to be enlarged for a statistical and
875 uncorrelated components, so correlated error is assumed to be negligible. The toy MC experiments
876 are performed for electron reconstruction, identification and trigger scale factors and muon recon-
877 struction + identification scale factors. In the current analysis 30 pseudo-experiments are used with
878 a combined toy MC method. Plots for C_W effect on a cross-section. Correlation

Table 15.1

Source of uncertainty	Method	$\delta C_W / C_W (\%)$ $W^+ \rightarrow e\nu$	$\delta C_W / C_W (\%)$ $W^- \rightarrow e\nu$	$\delta C_W / C_W (\%)$ $W^+ \rightarrow \mu\nu$	$\delta C_W / C_W (\%)$ $W^+ \rightarrow \mu\nu$	$\delta C_Z / C_Z (\%)$ $Z \rightarrow ee$	$\delta C_Z / C_Z (\%)$ $Z \rightarrow \mu\mu$
Electron reconstruction	Toy MC	0.11	0.09	-	-	0.12	-
Electron identification	Toy MC	0.32	0.30	-	-	0.54	-
Electron trigger efficiency	Toy MC	0.14	0.13	-	-	0.001	-
Muon reco+id	Toy MC	-	-	0.03	0.02	-	0.03
Electron energy scale	Offset	0.44	0.43	-	-	0.34	-
- Statistical error	Offset	0.05	0.04	-	-	0.04	-
- Bias in method	Offset	0.41	0.40	-	-	0.31	-
- Scale uncertainty	Offset	0.0	0.0	-	-	0.0	-
- Low Pt	Offset	0.0	0.0	-	-	0.003	-
- Presampler energy scale	Offset	0.04	0.03	-	-	0.04	-
- Material knowledge	Offset	0.14	0.13	-	-	0.14	-
Electron energy resolution	Offset	0.05	0.03	-	-	0.03	-
Muon energy scale	Offset	-	-	0.05	0.05	-	0.03
Muon energy resolution total	Offset	-	-	0.02	0.01	-	0.02
- Muon ID energy scale	Offset	-	-	0.02	0.01	-	0.01
- Muon MS energy scale	Offset	-	-	0.01	0.00	-	0.01
Hadron recoil scale	Offset	0.15	0.17	0.15	0.19	-	-
Hadron recoil resolution	Offset					-	-
EWK + $t\bar{t}$ background		0.15	0.16	0.16	0.17	0.01	0.01
QCD		0.34	0.62	0.02	0.04	-	-
PDF error							
Total		0.0041	0.0040	0.0013	0.0014	0.0036	0.0004
Statistics		1.60	2.13	1.51	2.02	4.82	3.93

879 15.3 Theoretical uncertainty

- 880 Theoretical uncertainties on the predictions are mostly dominated by a imperfect knowledge
of the proton PDF's. They are affecting both $A_{W,Z}$ and $C_{W,Z}$. Error coming from an arbitary
881 choice of PDF set is estimated by PDF reweighting <referennce> of original MC generated
882 using <something> to a one of the 4 pdf sets: CT10 <reference>, ATLAS-epWZ12 <reference>,
883 abkm09 <reference> and NNPDF23 <reference>. The error is calculated as a standard deviance
884 for all of the sets.
- 885 • Systematic uncertainty within one pdf set is evaluated using CT10 NLO set. This set contains
52 asosiated error sets, corresponding to a 90% C.L. limits along 26 eigenvectors. The resulting
52 variation are separetelly added in a quadrature as:

$$\delta_X = \frac{1}{2} \cdot \sqrt{\sum_{i=1}^N (X^+ - X^-)^2} \quad (15.4)$$

- 886 The uncertainties arising from the choise of generator and parton showering model are con-
sidered small. They can be calculated as a difference in the acceptances $A_{W,Z}$ for MC samples,
887 generated using same PDF set, but different models for showering and matrix element, namely
888 Powheg + Pythia and Sherpa

890 15.4 Correlation between uncertainties

891 15.4.1 Toy MC correlations

A correlation coefficient between two observables o_1 and o_2 can be estimated as:

$$\rho_{12} = \frac{1}{\sigma(o_1)\sigma(o_2)} \cdot \frac{1}{N-1} \sum_{i=1}^N (o_1^i - \bar{o}_1)(o_2^i - \bar{o}_2) \quad (15.5)$$

892 Using cholesky transformation this uncertainty can be propagated to a 3 eigenvectors:

893 15.4.2 Correlations between PDF's eigenvectors

Correlations for $A_{W,Z}$ and $C_{W,Z}$ for a CT10nlo set have been estimated, since they could affect error
on a total W boson cross section measurment and PDF fits. Given two processes X and Y (

$$\delta_{XY}^2 = \delta_X^2 + \delta_Y^2 + 2\delta_X\delta_Y\rho_{XY} \quad (15.6)$$

$$\rho_{XY} = \frac{1}{4\delta_X\delta_Y} \sum (X^+ - X^-) \cdot (Y^+ - Y^-) \quad (15.7)$$

894

Part V

895

Results

897 Results of the Cross Section Measurement

898 The cross-sections are calculated as described in Chap. 3. All of the W cross-sections are summarized
 899 in Tab. 16.1. The total uncertainty of the measurements in the fiducial region consists of the statistical,
 900 systematical and luminosity errors. The methods of these uncertainties determination are described
 901 in Chap. 15.

902 Because of the lepton universality of the Standard Model, the results, obtained in electron and
 903 muon channel are expected to agree with each other. The ratio in electron and muon channel is
 904 calculated with the respect of the correlated systematic uncertainties is shown in Fig.16.1. The ratios
 905 errors are mostly dominated by the statistics on the W and Z samples and agrees with Standard
 906 Model predictions within the uncertainty.

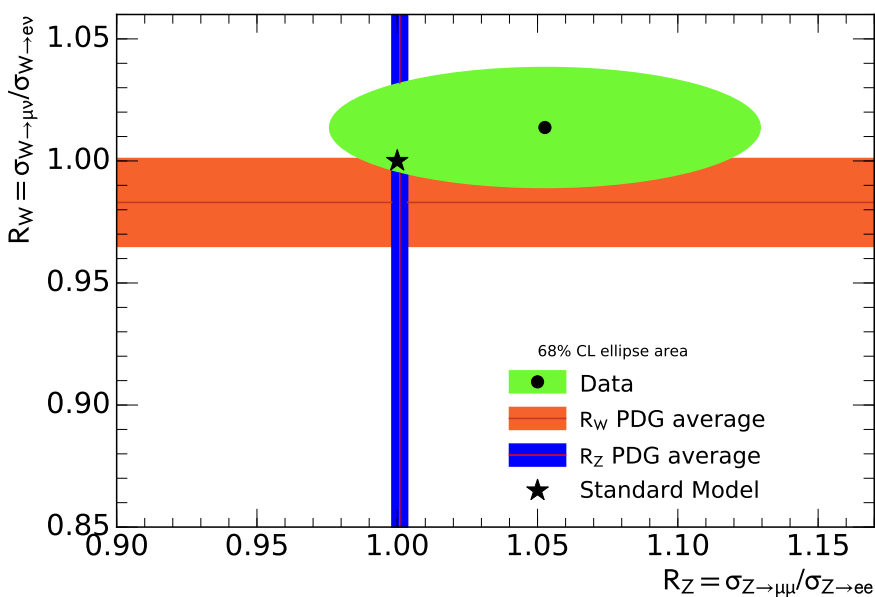


Fig. 16.1: Ratio of Z and W-boson production fiducial cross sections obtained in electron electron and muon channel compared to the expectations of the Standard Model and previous experimental checks of the lepton universality provided as PDG average bands.

Table 16.1: Results on a fiducial σ^{fid} and total cross-section measurement for W^+ , W^- and Z bosons in electron and muon channels. The cross-sections are shown with their statistical, systematical and luminosity uncertainties (and extrapolation error for total cross-section) quoted in that order

	value \pm stat \pm syst \pm lumi (\pm ext)	value \pm stat \pm syst \pm lumi (\pm ext)
W in electron channel		
	$W^+ \rightarrow e\nu$	$W^- \rightarrow e\nu$
σ_W^{fid} [pb]	$1406.0 \pm 23.3 \pm 8.4 \pm 42.2$	$783.8 \pm 17.5 \pm 4.5 \pm 23.5$
σ_W^{tot} [pb]	$2253.6 \pm 37.3 \pm 13.4 \pm 67.6 \pm 1.0$	$1373.0 \pm 30.7 \pm 7.9 \pm 41.2 \pm 5.9$
σ_W^{13} [pb]	$1293.9 \pm 21.4 \pm 7.7 \pm 38.8 \pm 0.0$	$733.8 \pm 16.4 \pm 4.2 \pm 22.0 \pm 0.0$
W in muon channel		
	$W^+ \rightarrow \mu\nu$	$W^- \rightarrow \mu\nu$
σ_W^{fid} [pb]	$1425.3 \pm 22.4 \pm 2.3 \pm 42.8$	$792.5 \pm 16.7 \pm 1.6 \pm 23.8$
σ_W^{tot} [pb]	$2284.7 \pm 35.8 \pm 3.7 \pm 68.5 \pm 1.0$	$1389.6 \pm 29.3 \pm 2.9 \pm 41.7 \pm 6.2$
σ_W^{13} [pb]	$1312.2 \pm 20.6 \pm 2.1 \pm 39.4 \pm 0.0$	$741.4 \pm 15.6 \pm 1.5 \pm 22.2 \pm 0.0$
Z		
	$Z \rightarrow ee$	$Z \rightarrow \mu\mu$
σ_Z^{fid} [pb]	$194.8 \pm 9.4 \pm 1.3 \pm 5.8$	$203.5 \pm 8.0 \pm 0.1 \pm 6.1$
σ_Z^{tot} [pb]	$310.4 \pm 15.0 \pm 2.0 \pm 9.3 \pm 1.1$	$322.9 \pm 12.7 \pm 0.1 \pm 9.7 \pm 1.0$
σ_Z^{13} [pb]	$176.1 \pm 8.5 \pm 1.1 \pm 5.3 \pm 0.0$	$183.2 \pm 7.2 \pm 0.1 \pm 5.5 \pm 0.0$

16.1 Combined results

Since the results between channels are agreeing well, it is possible to perform averaging as described in Sec. 3.3. Systematic uncertainties for the averaging are taken from Tab. 15.1. The systematic uncertainties calculated using Toy MC are included in the averaging following the prescription from Sec. 15.4. The common luminosity uncertainty is excluded from the combination process. The systematic uncertainties from electroweak background sources are considered uncorrelated between W and Z bosons and 100% correlated for different W and Z channels.

The combination yields a good $\chi^2/NDF=1.0/3$ indicating good agreement between measurements. The combined cross-section is extrapolated to the full fiducial phase-space using $A_{W/Z}$ factors. The resulting cross-sections are summarized in Tab. 16.2.

Table 16.2: Results on a fiducial σ^{fid} and total cross-section measurement for W^+ , W^- and Z bosons in electron and muon channels. The cross-sections are shown with their statistical, systematical and luminosity uncertainties (and extrapolation error for total cross-section) quoted in that order

	value \pm stat \pm syst \pm lumi (\pm ext)	value \pm stat \pm syst \pm lumi (\pm ext)
$W^{+/-}$		
	$W^+ \rightarrow l\nu$	$W^- \rightarrow l\nu$
σ_W^{fid} [pb]	$1413.3 \pm 16.1 \pm 6.9 \pm 42.4$	$786.7 \pm 12.1 \pm 3.8 \pm 23.6$
σ_W^{tot} [pb]	$2264.8 \pm 25.8 \pm 10.9 \pm 67.9 \pm 6.4$	$1380.1 \pm 21.2 \pm 14.8 \pm 41.4 \pm 3.6$
σ_W^{13} [pb]	$1300.4 \pm 14.8 \pm 6.3 \pm 39.0$	$736.2 \pm 11.3 \pm 3.6 \pm 22.1$
$W \rightarrow l\nu$		
σ_W^{fid} [pb]	$2200.0 \pm 20.1 \pm 10.7 \pm 66.0$	
σ_W^{tot} [pb]	$3644.9 \pm 33.4 \pm 21.1 \pm 109.3 \pm 6.7$	
σ_W^{13} [pb]	$2036.6 \pm 18.6 \pm 9.9 \pm 61.1$	
$Z \rightarrow ll$		
σ_Z^{fid} [pb]	$200.4 \pm 6.1 \pm 0.1 \pm 6.0$	
σ_Z^{tot} [pb]	$319.2 \pm 9.8 \pm 1.7 \pm 9.6 \pm 0.3$	
σ_Z^{13} [pb]	$180.2 \pm 5.5 \pm 0.1 \pm 5.4$	

16.2 Cross-sections ratios

The combination cross-section are in a fiducial region:

- $R_{W/Z} = 10.978 \pm 0.350 \text{ (stat)} \pm 0.048 \text{ (sys)}$
- $R_{W^+/Z} = 7.052 \pm 0.230 \text{ (stat)} \pm 0.031 \text{ (sys)}$
- $R_{W^-/Z} = 3.926 \pm 0.134 \text{ (stat)} \pm 0.017 \text{ (sys)}$
- $R_{W^+/W^-} = 1.796 \pm 0.034 \text{ (stat)} \pm 0.000 \text{ (sys)}$

16.3 Comparation with Theoretical Predictions

The theoretical predictions for cross-section measurements are obtained at NLO using MCFM/APPLIGRID for a different PDF sets: ABM12nlo, CT14nlo, MMHTnlo, ATLAS-epWZnlo, HERAPDF2.0nlo.

16.4 PDF fits